INTERPRETATION OF NUCLEAR MAGNETIC RESONANCE MEASUREMENTS IN FORMATIONS WITH COMPLEX PORE STRUCTURE

A Dissertation

by

LU CHI

Submitted to the Office of Graduate and Professional Studies of
Texas A&M University
in partial fulfillment of the requirements for the degree of

DOCTOR OF PHILOSOPHY

Chair of Committee,	Zoya Heidari
Committee Members,	Walter B. Ayers
	Yuefeng Sun
	Steve M. Wright
Head of Department,	A. Daniel Hill

August 2015

Major Subject: Petroleum Engineering

ABSTRACT

Nuclear Magnetic Resonance (NMR) measurement as an unconventional well logging method, is among the most accurate approaches to estimate formation porosity. Petrophysicists use NMR to evaluate petrophysical properties such as pore size distribution, permeability, and fluid saturation, of various formations. However, the NMR responses in complex formations, such as fractured carbonate and organic-rich mudrocks, have not been thoroughly investigated. NMR pore-scale simulations using a random-walk algorithm enable us to model the NMR relaxometry in porous rock samples, and to improve interpretation of NMR relaxometry in complex formations. Based on pore-scale simulations and theoretical analysis of NMR relaxometry, this research estimated petrophysical properties that have been challenging when using conventional NMR interpretation, including micro-fracture volumetric concentration, directional pore connectivity and directional permeability, and the impact of wettability alteration.

This dissertation (a) quantified the impacts of micro-fractures on NMR relaxation times by pore-scale simulations and developed an analytical model for fracture-pore diffusional coupling in multiple-pore-type systems (i.e. composed of intra-/inter-granular pores and micro-fractures); (b) investigated the viability of using the NMR analytical model to estimate the volumetric concentrations and apertures of micro-fractures in fractured formations; (c) developed an innovative

NMR-based directional permeability model to estimate anisotropic permeability of rock samples with complex pore structure; (d) investigated the impacts of fracture-pore diffusional coupling on NMR permeability assessment and evaluated reliability of NMR permeability models in fractured formations; and (e) developed a two-phase NMR pore-scale simulation method to model the NMR responses in organic-rich mudrocks, as well as investigated the impact of wettability alteration on NMR relaxometry in organic-rich mudrocks.

The methods used in this research include pore-scale image processing, single-phase and two-phase NMR simulations in porous media, fluid flow simulations in porous media, and theoretical analysis of NMR relaxation mechanisms in porous media. Results show that the introduced methods for interpretation of NMR relaxometry can enhance reservoir characterization in challenging reservoirs, including carbonates and organic-rich mudrocks.

To

my dear husband

Mulin Cheng,

my baby girl,

Adele Cheng,

and my parents

Jianhua Chi & Lijie Zhu

ACKNOWLEDGEMENTS

I would like to thank my advisor, Dr. Zoya Heidari, for her continuous support, encouragement, and challenges in my PhD study. The past three years I spent studying petrophysics in her group has become and will always be a precious asset for me. My fruitful experiences here have strengthened my passion for petrophysics, and confirmed my expectation that petrophysics is the life-long career for me. I would like to thank the other members of my committee, Dr. Steve Wright, Dr. Walter Ayers, and Dr. Yuefeng Sun, for their guidance and encouragement throughout the course of my research, and for spending time to review my dissertation and attend my final defense. I also want to extend my gratitude to Prof. Martin Blunt and his research group at Imperial College London, for providing the original NMR simulation code and micro-CT images of 12 rock samples.

My sincere thanks go to the department faculty and staff for making my time at Texas A&M University a great experience. I would like to thank Professor Yucel Akkutlu for his listening, understanding and kind suggestions. Thanks to Ms. Eleanor Schuler for her time and help in assisting my graduation procedure. Special thanks go to Gia Alexander, who helped me proof-read this dissertation and almost all of my publications with her excellent language skills.

I would like to thank my friends and colleagues at Texas A&M University – Yuhai Zhou, Huangye Chen, Kai Cheng, Nikhil Kethireddy, Marcus Elliot, Artur Posenato Garcia, Emmanuel Oyewole, Mehrnoosh Saneifar, Angie Yang, Bicheng Yan, Dr. Yao Tian, Dr. Zheng Zhang, and Dr. Jichao Yin – for the help, the fun, and the good time we had together.

Finally, thanks to my beloved parents, Jianhua Chi and Lijie Zhu, and my twin sister, Xuan Chi, for their encouragement and whole-hearted support. Millions of thanks go to my dear husband, Mulin Cheng, for his love, patience, and support. Without his meticulous love and support, I could never finish my PhD study smoothly in such a short time. Also thanks to my newborn baby girl, you made my last year of PhD study full of joy and excitement.

ACRONYMS

1D	One-dimensional
2D	Two-dimensional
3D	Three-dimensional
BVI	Bulk Volume Irreducible
BVM	Bulk Volume Movable
CT	Computed Tomography
CPMG	Carr-Purcell-Meiboom-Gill
EPC	Euler-Poincare Characteristics
FIB-SEM	Focused Ion Beam Scanning Electron Microscope
ILT	Inverse Laplace Transform
LBM	Lattice Boltzmann Method
NMR	Nuclear Magnetic Resonance
RF	Radio Frequency
SDR	Schlumberger Doll Research

NOMENCLATURE

C	Constant in conventional NMR permeability models, ( )
C_J	Number of redundant connections along J direction, J can be either X, Y, or Z, ( )
d	Diameter of spherical pores or channel-like inclusions, (μm)
D	Diffusion coefficient, (m^2/sec)
e_{2D}	EPC in 2D space, ( )
e_{3D}	EPC in 3D space, ( )
$e_{2,i}$	2D EPC of the i-th image, ( )
$e_{3,i}$	3D EPC of the i-th image, ( )
$(e_{3D})_J$	3D EPC of a 3D matrix along J direction, J can be either X, Y, or Z, ( )
F	Electrical formation factor, ( )
G	Spatial gradient of the internal magnetic field, (Hz/mm)
h	Half the aperture of planar fractures, (μm)
H	Number of completely enclosed cavities, ( )
$I_{coupled}$	Intensity of coupled micro-fractures, ( )
I_{iso}	Intensity of isolated micro-fractures, ( )
k	Absolute permeability, (mD)
k_{Coates}	Permeability estimated by Coates model, (mD)
k_J	Directional absolute permeability along J direction, J can be either X, Y, or Z, (mD)

k_{SDR}	Permeability estimated by SDR model, (mD)
L	Length of planar fractures or channel-like inclusions, (μm)
m	Constant in conventional NMR permeability models, ( )
M_F	Magnetization in fractures per unit volume, (A/m^4)
M_G	Magnetization in porous grains per unit volume of pore space, (A/m^4)
M_0	Initial transverse magnetization at time zero in NMR simulations, (A/m^4)
$M(t)$	Transverse magnetization at time t in NMR simulations, (A/m^4)
n	Constant in conventional NMR permeability models, ( )
N	Number of isolated components, ( )
N_0	Initial number of total walkers in NMR simulations, ( )
$N(t)$	Number of alive walkers at time t in NMR simulations, ( )
$P(t)$	Fraction of alive walkers at time t in NMR simulations, ( )
p	Constant in NMR directional permeability model, ( )
q	Constant in NMR directional permeability model, ( )
s	Walking step distance of random walkers in NMR simulations, (μm)
S	Surface area of pore space, (m^2)
T_2	NMR transverse relaxation time, (msec)
T_{2B}	Bulk relaxation time of NMR transverse relaxation, (msec)
$T_{2B,eff}$	Effective bulk relaxation time in the two-phase NMR simulations, (msec)
$T_{2B,hc}$	Bulk relaxation time of hydrocarbon, (msec)
$T_{2B,w}$	Bulk relaxation time of water or brine, (msec)
$T_{2cutoff}$	T_2 cutoff value between *BVI* and *BVM* in the Coates permeability model,

(msec)

T_{2D} Diffusion-induced relaxation time of NMR transverse relaxation, (msec)

$T_{2,G}$ Relaxation time in the porous grains, (msec)

$T_{2F,coupled}$ Relaxation time in the coupled micro-fractures, (msec)

$T_{2F,iso}$ Relaxation time in the isolated micro-fractures, (msec)

T_{2GM} Geometric mean of T_2 distribution (msec)

T_{2p} Relaxation time associated to inter-granular pores (msec)

T_{2S} Surface relaxation time of NMR transverse relaxation, (msec)

TE Inter-echo spacing time, (μsec)

V Volume of pore space, (m^3)

w Aperture of planar fractures, (μm)

W Distance from fracture center to grain center in the 1D model for fracture-pore diffusional coupling, (μm)

ε_J Directional pore-connectivity factor along J direction, J can be either X, Y, or Z, ( )

α Constant in NMR directional permeability model, ( )

β Constant in NMR directional permeability model, ( )

λ Constant in NMR directional permeability model, ( )

χ_{hc} Volume ratio of hydrocarbon in all fluids in the two-phase NMR simulations, ( )

χ_w Volume ratio of water or brine in all fluids in the two-phase NMR simulations, ( )

γ	Gyromagnetic ratio of a proton, (rad•sec^{-1}•Tesla^{-1})
δ	Death probability of random walkers in NMR simulations, ( )
Δt	Walking step time of random walkers in NMR simulations, ( )
ϕ	Porosity, (%)
$\phi_{F,iso}$	Amplitude of T_2 mode of isolated micro-fractures, (%)
$\phi_{F,coupled}$	Amplitude of T_2 mode of coupled micro-fractures, (%)
ϕ_G	Inter-granular porosity in the porous grains, (%)
ϕ_{pore}	Inter-granular porosity in the porous grain domain, (%)
ϕ_{tot}	Total porosity of rock, (%)
ρ	Surface relaxivity, (μm/sec)
ρ_2	Surface relaxivity of transverse relaxation, (μm/sec)

TABLE OF CONTENTS

Pages

LIST OF FIGURES

Page

LIST OF TABLES

Page

1. INTRODUCTION

This section reviews the background knowledge on Nuclear Magnetic Resonance (NMR) measurements and defines the scope, objectives, and organization of this dissertation. Borehole NMR measurements have been among the most reliable techniques to evaluate porosity and pore-size distribution in fluid-bearing formations. However, reliable application of NMR relaxometry for pore network characterization in formations with complex pore structures remains challenging. This dissertation investigates the impacts of micro-fractures on NMR relaxometry and NMR permeability assessment, develops a new NMR-based permeability model to estimate directional permeability, and introduces a two-phase NMR pore-scale simulation method.

1.1. Background

To introduce the background for NMR application in well logging and formation evaluation, this work begins by describing the basics of NMR physics, and then briefly reviewing the applications of NMR relaxometry in petrophysical evaluation.

1.1.1. Basics of NMR Physics

NMR technique is a process of manipulating the nuclear spins within a material to generate detectable magnetic signals, and then measuring the chemical and physical properties of the material under study. Therefore, nuclear spin is the first concept that one encounters when introducing NMR technique. Nuclear spin, which is the quantum

angular momentum of the nucleus of an atom, is an intrinsic property of every nucleus. In Quantum Mechanics, the quantum number for nuclear spin is usually denoted as S, and the spin operator $\hat{S}$ can be expressed by $\hat{S} = \hbar\sqrt{S(S+1)}$, where $\hbar = \frac{h}{2\pi}$ is the Plank constant, 1.055×10^{-34} J·sec. The spin quantum number, S, can take integer or half-integer numbers. Since this dissertation concerns the hydrogen nucleus, particularly the proton, which has a spin quantum number of ½, it will focus on spin-1/2 particles throughout this work.

In addition to nuclear spin, a nucleus also possesses intrinsic magnetism; in other words, it has a magnetic dipole moment. The nuclear magnetic moment, μ, is directly proportional to nuclear spin by

$$\hat{\mu} = \gamma \hat{S}, \tag{1-1}$$

where γ is the gyromagnetic ratio of nuclear spin, and the hat above the symbols denotes quantum mechanical operators (Levitt 2001). For proton spins in water, γ is equal to 42.58 MHz/Tesla. Correspondingly, the nuclear magnetic moment is given by $\hat{\mu} = \gamma\hbar\sqrt{S(S+1)}$.

When an external static magnetic field is applied on a nuclear spin, the nuclear magnetic moment starts rotating around the magnetic field direction, keeping a constant angle between the spin axis and the magnetic field direction like a cone (Levitt 2001).

This motion is called Larmor precession, and the frequency of this spin precession is defined as Larmor frequency, ω, given by

$$\omega = 2\pi f = \gamma B, \tag{1-2}$$

where B is the external magnetic field. This relationship dictates that the Larmor frequency of spin precession is determined by the local magnetic field at the site of nuclear spin. In the petroleum industry, most of the commercial NMR core analyzers apply a 0.047 Tesla magnetic field on fluid-bearing rock samples, so the proton spins in the fluids inside the sample has a Larmor frequency of 2 MHz.

When a nuclear spin is placed in an external static magnetic field $\vec{B}_0$, one can use a classical mechanics approach to derive the equation governing its motion. Since the nuclear spin $\vec{S}$ can be treated as an angular momentum vector, its time derivative is equal to the torque, $\vec{T}$, applied on the nucleus, which is given by $\vec{T} = \vec{\mu} \times \vec{B}_0$. Therefore the time derivative of magnetic moment, $\vec{\mu}$, can be expressed via

$$\frac{d\vec{\mu}}{dt} = \gamma \frac{d\vec{S}}{dt} = \gamma \vec{T} = \gamma \vec{\mu} \times \vec{B}_0, \tag{1-3}$$

which is the equation of motion for a rotating vector $\vec{\mu}$ around the vector $\vec{B}_0$. Because the net magnetization vector, $\vec{M}$, is simply expressed by the sum of all magnetic dipole moments (i.e. $\vec{M} = \sum_i \mu_i$), we can derive the Bloch equation (Bloch 1946) for the macroscopic magnetism, given by

$$\frac{d\vec{M}}{dt} = \gamma \vec{M} \times \vec{B}_0. \tag{1-4}$$

The Bloch equation is further modified by adding relaxation terms to give a complete description of the nuclear spin dynamics in a z-direction magnetic field, which becomes the modified Bloch equation (Bloch 1946), as given by

$$\frac{d\vec{M}}{dt} = \gamma \vec{M} \times \vec{B}_0 - \frac{M_x}{T_2}\hat{x}' - \frac{M_y}{T_2}\hat{y}' - \frac{M_z}{T_1}\hat{z} + \frac{\vec{M}_o}{T_1}, \tag{1-5}$$

where $\hat{x}'$ and $\hat{y}'$ denote the rotating axes of the rotating frame $\Sigma = (\hat{x}', \hat{y}', \hat{z})$, T_1 and T_2 are the longitudinal and transverse relaxation time, and $\vec{M}_o$ is the equilibrium magnetization vector given by $\vec{M}_o = M_o \hat{z}$. The relaxation processes in the Z direction and in the X-Y plane are referred to as longitudinal relaxation (or spin-lattice relaxation, T_1 relaxation) and transverse relaxation (or spin-spin relaxation, T_2 relaxation), respectively.

At equilibrium, the nuclear spins in a homogeneous material are randomly oriented and show net zero magnetization. When applying a static magnetic field $\vec{B}_0$ along the z-axis, the isotropic distribution of nuclear spin directions starts breaking down. After sufficient time the net result is a non-zero magnetization along the z-axis (i.e. the system reaches a new thermal equilibrium). Applying an oscillating magnetic field $\vec{B}_1$ in the X-Y plane tips the net magnetization vector $\vec{M}$ away from Z-axis by an angle given by

$$\alpha = \frac{\gamma B_1 T_p}{2}, \tag{1-6}$$

where T_p is the pulse length of the oscillating magnetic field B_1 (Wright 1999). The tipping angle α can easily be adjusted to 90° or 180° by changing the magnetic field B_1 and the pulse length T_p. Now, assume that the first Radio Frequency (RF) pulse tips the magnetization vector $\vec{M}$ away from Z-axis by 90°. In this case, the magnetization vector is placed on the X-Y plane, so it starts rotating around the static magnetic field $\vec{B}_0$ with its Larmor frequency. When the B_1 pulse is suddenly stopped, the magnetization vector $\vec{M}$ will relax back to its initial equilibrium state, i.e. along the Z-axis. During this process, the exponential increase of the longitudinal magnetization, M_z, is termed T_1 relaxation, and the exponential decrease of the transverse magnetization, $M_{x\text{-}y}$, is termed T_2 relaxation. The two relaxation processes can be described by the equations

$$M_z(t) = M_0(1 - e^{-\frac{t}{T_1}}), \tag{1-7}$$

and

$$M_{xy}(t) = M_{xy}^0 e^{-\frac{t}{T_2}}. \tag{1-8}$$

as well as in **Fig. 1.1** (Coates et al. 1999). Equations (1-7) and (1-8) are the solution to the modified Bloch equation, Equation (1-5).

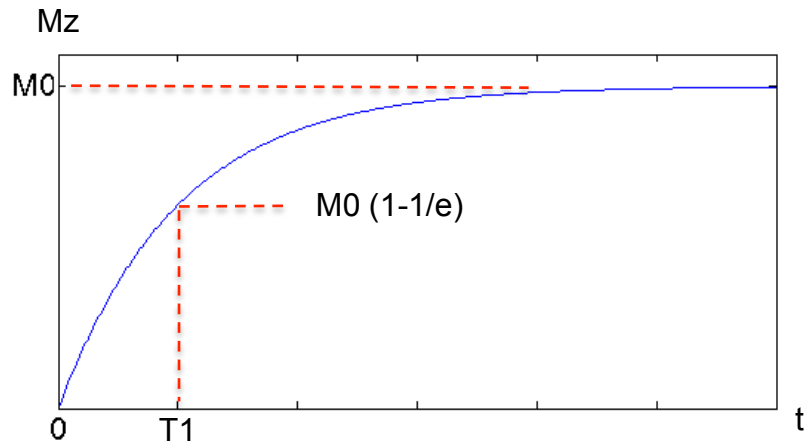

(a)

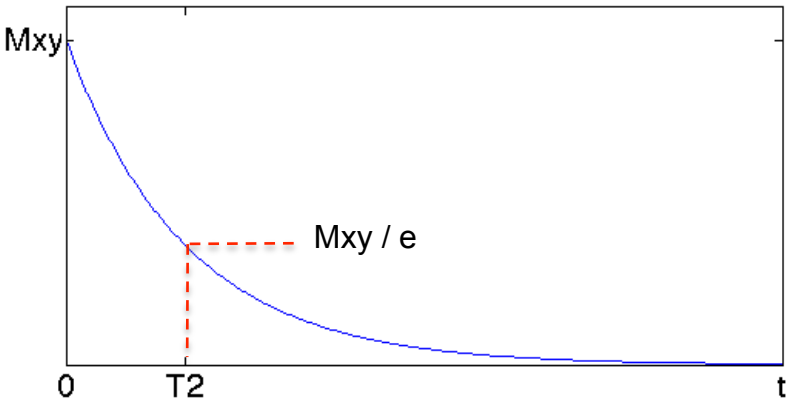

(b)

Fig. 1.1—(a) T_1 relaxation process in the longitudinal direction: exponential increase of the longitudinal magnetization, M_z; and (b) T_2 relaxation process in the transverse direction: exponential decrease of the transverse magnetization, M_{xy}.

Furthermore, measurement of the T_2 relaxation is of special interest for NMR core analysis due to its close relationship with pore size and its relatively easy acquirement. When the transverse magnetization vector, $M_{x\text{-}y}$, rotates around the Z-axis, the individual nuclear spins have slightly different Larmor frequencies due to inhomogeneous magnetic field, which causes a phenomenon called "dephasing" of nuclear spin precession. The net result is that the transverse magnetization vector, $M_{x\text{-}y}$, "fans out" in the X-Y plane, as illustrated in **Fig. 1.2**. This fast reduction of the $M_{x\text{-}y}$

signal caused by dephasing is termed the "free induction decay," characterized by the relaxation time T_2*, and should not be taken as the transverse relaxation time T_2. To refocus the magnetization, a 180° RF (radio frequency) pulse is applied in the X-Y plane to flip the nuclear spins by 180°, so they "rephase" to generate a spin echo. Repeatedly applying the 180° RF pulse in the X-Y plane generates a spin-echo train. The outline of this train shows the T_2 relaxation decay. A 90° pulse sequence, followed by a series of 180° pulses, is termed the Carr-Purcell-Meiboom-Gill (CPMG) pulse sequence (Carr and Purcell 1954; Meiboom and Gill 1958). By this means, the T_2 relaxation decay, i.e. the outline of the spin-echo train, is measured and analyzed by the NMR spectrometer.

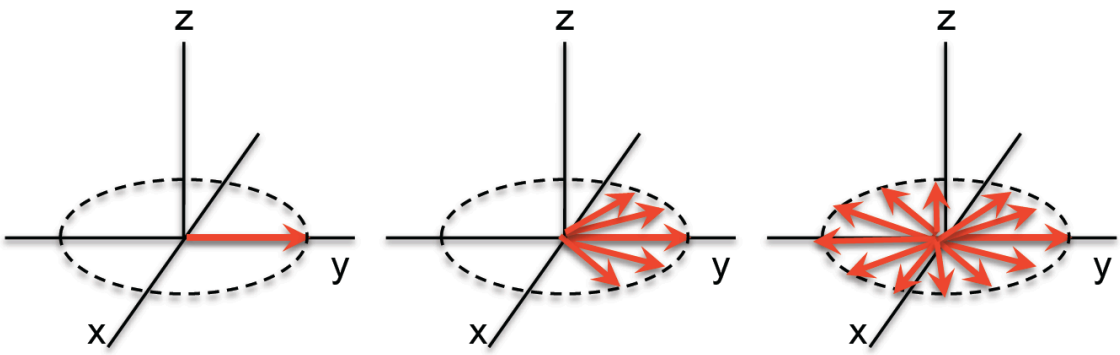

Fig. 1.2—The transverse magnetization vector, $M_{x\text{-}y}$, fans out in the X-Y plane due to dephasing of nuclear spins, depicted in the rotating frame.

1.1.2. NMR Petrophysics

Unlike chemistry, physics, and medical sciences, which extensively use NMR spectroscopy, NMR petrophysics mainly focuses on NMR relaxometry. Many petrophysical studies have applied NMR relaxometry in porous media since Brownstein

and Tarr (1979) and Kleinberg et al. (1994) investigated the mechanism of proton relaxation in restricted space and the NMR relaxation of fluids in rock samples. Today, it is well accepted that in the fast diffusion limit, the NMR spin-spin relaxation time, T_2, of proton spins in the fluid phase within a porous media, can be expressed as

$$\frac{1}{T_2} = \frac{1}{T_{2B}} + \frac{1}{T_{2S}} + \frac{1}{T_{2D}} = \frac{1}{T_{2B}} + \rho_2 \left(\frac{S}{V}\right)_{pore} + \frac{D\left(\gamma \cdot G \cdot TE\right)^2}{12}, \tag{1-9}$$

where T_{2B} is the bulk relaxation time, T_{2S} is the surface relaxation time, T_{2D} is the diffusion-induced relaxation time, ρ_2 is the surface relaxivity for transverse relaxation, S/V is the surface-to-volume ratio of the pore space, D is the diffusion coefficient of pore fluids, γ is the gyromagnetic ratio of a proton, G is the internal magnetic field gradient, and TE is the inter-echo spacing time of CPMG pulse sequence (Kleinberg and Horsfield 1990).

Equation (1-9) explains that the T_2 relaxation process in a porous media can be attributed to three independent relaxation mechanisms: the bulk relaxation, the surface relaxation, and the diffusion-induced relaxation (Kleinberg and Horsfield 1990; Coates et al. 1999; Mohnke and Klitzsch 2010; Daigle et al. 2014; Washburn 2014). The bulk relaxation is due to the homonuclear dipolar coupling, or the dipole-dipole coupling, between proton spins in a fluid in an unbounded medium. The surface relaxation is mainly caused by the interactions between proton spins in the fluid phase and the paramagnetic ions on the grain surface. The diffusion-induced relaxation, on the other

hand, is generated by the diffusion of fluid molecules in an inhomogeneous magnetic field.

In rock samples bearing brine or pure water, the NMR T_2 relaxation is dominated by the surface relaxation, noted as the second term on the right-hand side of Equation (1-9). Therefore, petrophysicists commonly interpret NMR T_2 distribution as representing the pore size distribution of the rock sample, when (a) the pore space is fully saturated with brine or pure water, (b) short TE in the CPMG pulse sequence is used, and (c) all the pore surface has a uniform surface relaxivity ρ_2. Due to its sensitivity to pore size distribution, petrophysicists have extensively used NMR relaxometry to perform permeability assessment, fluid saturation estimation, and fluid typing of rock samples in the petroleum industry (Coates et al. 1999; Akkurt et al. 2009; Chen et al. 2008; Zielinski et al. 2010; AlGhamdi et al. 2012; Jerath et al. 2012; Freedman et al. 2013; Jain et al. 2013; Meridji and Hursan 2013; Serry et al. 2013; Souza et al. 2013; Valori et al. 2014).

The determination of T_2 distribution from the measured NMR T_2 relaxation decay is a mathematical inversion problem, in other words, the T_2 inversion process. An algorithm, such as Inverse Laplace Transform (ILT), is used to analyze the measured T_2 relaxation decay to estimate the T_2 distribution (Venkataramanan et al. 2015). In the ILT method, a cost function Q is minimized with respect to a non-negative T_2 distribution f, as given by

$$Q = \| G - Lf \|^2 + \alpha \| f \|^2, \quad (1\text{-}10)$$

where G is a vector representing the measured NMR transverse magnetization decay data, L is a matrix relating the T_2 distribution to the measured NMR data, and the parameter α is the regularization parameter, which can be chosen by various methods, such as constrained least squares method, cross validation method, and L-curve criteria (Galatsanos and Katsaggelos 1992; Aster et al. 2012). By this means, a non-negative T_2 distribution f is estimated from the measured NMR transverse magnetization decay, and is often used to study pore size distribution and other petrophysical properties of rock samples in the petroleum industry.

1.2. Statement of Problems

Borehole NMR measurements have been among the most reliable techniques for in situ assessment of petrophysical properties. However, interpretation of NMR measurements in formations with complex pore structure has several unanswered questions. The research for this dissertation investigated new techniques for interpretation of NMR relaxometry in complex formations, thus, improving evaluation of their petrophysical properties. The five problems that this work investigates are (a) impacts of micro-fractures on NMR relaxometry in multiple-pore-type systems and their physical origin, (b) assessment of micro-fracture porosity and aperture in fractured formations using a NMR analytical model, (c) NMR directional permeability assessment using NMR relaxometry, (d) the impact of fracture-pore diffusional coupling on NMR

permeability assessment, and (e) two-phase NMR simulations in organic-rich mudrocks and the impact of wettability alteration on NMR relaxometry.

1.2.1. Impact of Micro-fractures on NMR Relaxometry in Multiple-pore-type Systems

The volumetric concentration of micro-fractures and the pore size distribution in formations significantly influence fluid transport and the success of hydraulic fracturing. Conventional well-log interpretation techniques cannot distinguish between different pore structures. NMR relaxometry, although sensitive to the pore size distribution in rock formations, has been conventionally considered as insensitive to the existence of fractures. Therefore, the impact of micro-fractures on NMR relaxometry has not been investigated. Previous publications on wide fractures (i.e. fractures with aperture larger than 0.2 mm) assume that they have no interactions with inter-granular pores on NMR T_2 distribution. Thus, wide fractures can be isolated from inter-granular pores and quantified separately. However, our simulation results show that micro-fractures can influence NMR relaxometry. In this research, we quantify the impact of micro-fractures/channels on NMR relaxometry in multiple-pore-type systems and name the phenomenon as fracture-pore diffusional coupling effect.

1.2.2. Assessment of Micro-fracture Porosity using NMR Relaxometry

Quantification of micro-fracture content in a fractured formation has been challenging for conventional well logs. The previous faulty assumption that NMR relaxometry is insensitive to micro-fractures led researchers to conclude that

quantification of micro-fracture content in a fractured formation using NMR relaxometry is also impossible, so it has not been investigated. This research uses the 1D analytical model developed in Section 3 to inversely solve the volumetric concentration and aperture of micro-fractures in fractured formations. The outcomes of this research enable future applications of NMR relaxometry in real-time assessment of micro-fracture volumetric concentration.

1.2.3. Assessment of Directional Permeability using NMR Relaxometry

Permeability assessment from NMR data includes empirical correlations, such as Coates (Coates et al. 1997) and SDR models (Kenyon et al. 1988). However, carbonate rocks are known for lack of good correlations between pore-size and pore-throat-size, which makes it challenging and often unreliable to estimate permeability from NMR T_2 distribution. Furthermore, permeability estimated from all the previous NMR models does not reflect the anisotropic characteristics of rock permeability. Thus, if directional permeability can be estimated from NMR data, it can significantly improve permeability assessment in complex formations that have anisotropic properties.

1.2.4. Influences of mMicro-fractures on NMR Permeability Assessment

Subsection 1.2.1 demonstrated that the NMR fracture-pore diffusional coupling effect may distort the NMR T_2 distribution in multiple-pore-type systems, which can lead to misinterpretation of pore size distribution of rock samples (Chi and Heidari 2015a). It follows that the distortion of T_2 distribution can influence NMR permeability

assessment in multiple-pore-type systems. Nevertheless, the influences have not been investigated. The reliability of the NMR permeability models in fractured formation thus remains questionable. The present research quantifies the impact of micro-fractures and fracture-pore coupling on NMR permeability assessment, and evaluates the reliability of NMR permeability models, including our new NMR directional permeability model as described in the third research topic (subsection 1.2.3).

1.2.5. Two-phase NMR Simulations in Organic-rich Mudrocks

Interpretation of NMR data in organic-rich mudrocks remains a challenge for petrophysicists, due to their complex pore structure and mixed wettability characteristics. Quantification of wettability using NMR measurements has been investigated by experimental studies, but numerical simulations have not been utilized to study wettability of organic-rich mudrocks. A reliable numerical simulation of NMR responses in these rocks can improve understanding of NMR relaxometry results and the corresponding estimated petrophysical properties. Therefore, this research introduces a two-phase NMR simulation method to model the NMR responses in organic-rich mudrocks. This work advances studies on wettability alteration of organic-rich mudrocks, and provides an alternative approach, in addition to empirical study, to investigate petrophysical properties of such formations.

Solutions to the research problems stated above may enable reliable interpretation of NMR measurements in formations with complex pore structures. The

outcomes of the improved interpretation methods will include more accurate estimates of micro-fracture volumetric concentration, directional permeability, and wettability. Reliable estimates of these properties have been challenging with conventional well logs, and with existing NMR interpretation methods. The outcomes of this research, including improved real-time evaluation of in situ petrophysical properties of formations, can facilitate operational decisions for enhanced production from complex reservoirs.

1.3. Research Objectives

The objectives of this research include:

1. Quantification of the impact of micro-fractures on NMR relaxation times and permeability assessment in multiple-pore-type systems by numerical simulations and theoretical analysis;
2. Investigation of the viability of using an NMR analytical model of fracture-pore diffusional coupling to estimate the volumetric concentrations and apertures of micro-fractures in fractured formations;
3. Development of a new NMR-based permeability model to estimate directional permeability from pore-scale images of rock samples;
4. Development of NMR pore-scale simulator to simulate the two-phase NMR responses in organic-rich mudrocks; and
5. Investigation of the impacts of fluid distribution and wettability alteration on NMR relaxometry in organic-rich mudrocks using numerical simulations.

1.4. Organization of the Dissertation

The balance of this dissertation consists of seven additional sections. Section 2 describes the methods used for the research, including processing pore-scale images, simulating single-phase and two-phase NMR in rock samples, and simulating fluid-flow in rock samples to calculate absolute permeability. Section 3 establishes the impact of micro-fractures on NMR relaxometry in sandstone, carbonate, and organic-rich mudrock samples by numerical simulations, and introduces a new concept of fracture-pore diffusional coupling. This section further presents 1D analytical model for this effect to explain the phenomena observed in numerical simulations. Section 4 explores the possibility of applying the fracture-pore diffusional coupling analytical model to inversely evaluate the micro-fracture aperture and volumetric concentrations in fractured formations, including carbonate and organic-rich mudrocks. Section 5 introduces a new method for directional permeability assessment using NMR relaxometry, by incorporating a directional pore-connectivity factor, which can be calculated from pore-scale images. Section 6 further discusses the influences of fracture-pore diffusional coupling on NMR permeability assessment, and evaluates the reliability of different NMR-based permeability models in fractured formations. Section 7 extends the single-phase NMR simulations used in previous sections to two-phase NMR simulations, to simulate NMR signals from both water and hydrocarbon phases in organic-rich mudrock samples. The two-phase NMR simulation further supports an evaluation of the impact of fluid distribution and wettability alteration on NMR relaxometry of organic-rich

mudrocks. Finally, Section 8 summarizes the main results and conclusions of this dissertation research and gives recommendations for future work.

2. METHODS

This research applies pore-scale image processing for rock samples, single-phase and two-phase NMR simulations in porous media, and fluid flow simulations in porous media to calculate absolute permeability. Later sections describe theoretical analysis and modeling for specific topics.

2.1. Pore-Scale Image Processing

The binary digital rock matrices presented in this dissertation were converted from micro-CT images of real rock samples, obtained from the Petroleum Engineering and Rock Mechanics group at Imperial College London, or synthetically created. Micro-CT images of real rock samples were scanned at W. D. Von Gonten Laboratory at Texas A&M University in College Station, Texas. Next, Fiji, an open-source image processing software (Schindelin et al. 2012), converted the original grey-scale micro-CT images to binary (black-and-white) images by trainable segmentation. The subsequent task involved converting the binary images to a data matrix (0 represents pore pixel and 1 represents grain pixel), to serve as the input file for single-phase NMR numerical simulations. The rock matrices obtained from Imperial College London were also converted from micro-CT images, but were binarized using a median filter (Dong 2007). All digital rock matrices served as input files for single-phase NMR simulations or fluid flow simulations (LBM method) (Degruyter et al. 2010), as described later.

Two-phase NMR simulations in organic-rich mudrock samples require four components in pore-scale images or rock matrices to represent water phase, hydrocarbon phase, inorganic minerals, and kerogen. In this dissertation, the digital rock matrices representing organic-rich mudrock samples were either converted from FIB-SEM (Focused Ion Beam Scanning Electron Microscope) images of real organic-rich mudrock samples, or they were synthetically generated. The FIB-SEM images were obtained in the W. D. Von Gonten Laboratory. Fiji performed trainable segmentation on the original grey-scale FIB-SEM images to convert them into four-color images, showing inorganic pores (red), inorganic minerals (green), organic pores (purple), and kerogen (yellow) regions. The stack of four-color images contributed to generating a data matrix (0 for water, 1 for inorganic minerals, 2 for hydrocarbon, and 3 for kerogen) to serve as the input file for two-phase NMR numerical simulations, as described in the next section.

2.2. Single-phase NMR Simulations in Rock Samples and T_2 Inversion

A random-walk algorithm served to simulate the NMR responses in rock samples (**Fig. 2.1**) (Øren and Bakke 2002; Ramakrishnan et al. 1998) via a C++ program adapted from the work of Talabi et al. (2009).

Single-phase fluid saturation was assumed in the NMR simulator. The input file for the simulator was a data matrix (0 represents pore pixel and 1 represents grain pixel), either converted from micro-CT images of rock samples or synthetically generated. The single-phase NMR simulations assumed that (a) the pore space is fully saturated with

brine water (i.e., T_{2B} of the saturating fluid is assumed to be 3.1 sec), and (b) there is no diffusion-induced relaxation (i.e., the internal field gradient, G, is zero).

The NMR T_2 distribution was then estimated from an inversion of the simulated NMR magnetization decay using a curvature smoothing method (Chen et al. 1999; Talabi et al. 2009; Toumelin et al. 2003). The area under each T_2 distribution curve represents the total porosity of the rock.

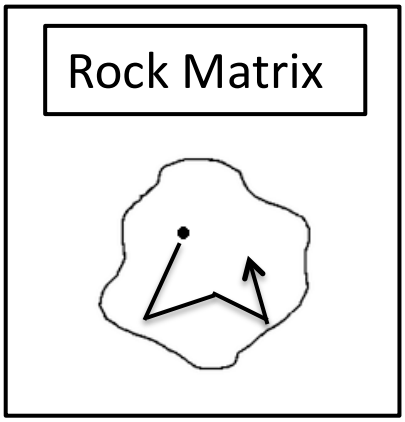

Fig. 2.1—The single-phase random-walk algorithm for NMR numerical simulation in a porous rock matrix.

2.3. Two-Phase NMR Simulations in Organic-rich Mudrocks

We modified the single-phase NMR simulator to simultaneously simulate the two-phase NMR response in organic-rich mudrocks. The input to the two-phase NMR simulator included three-dimensional (3D) digital matrices of organic-rich mudrocks, in which 0 stands for inorganic pore pixels, 1 for grain pixels, 2 for organic pore pixels, and 3 for kerogen. Other input parameters include magnetic properties of kerogen and rock

matrix, gas and water diffusion coefficients, and NMR tool parameters. The output of the NMR simulator is the transverse magnetization decay in the organic-rich mudrock sample. NMR responses from organic and inorganic pores are simulated simultaneously using a random-walk algorithm (**Fig. 2.2**). Section 7 covers more details about the two-phase NMR simulations. The two-phase NMR simulator also assumed no diffusion-induced relaxation. Then, the NMR T_2 distribution was estimated using the same T_2 inversion method described in the previous section.

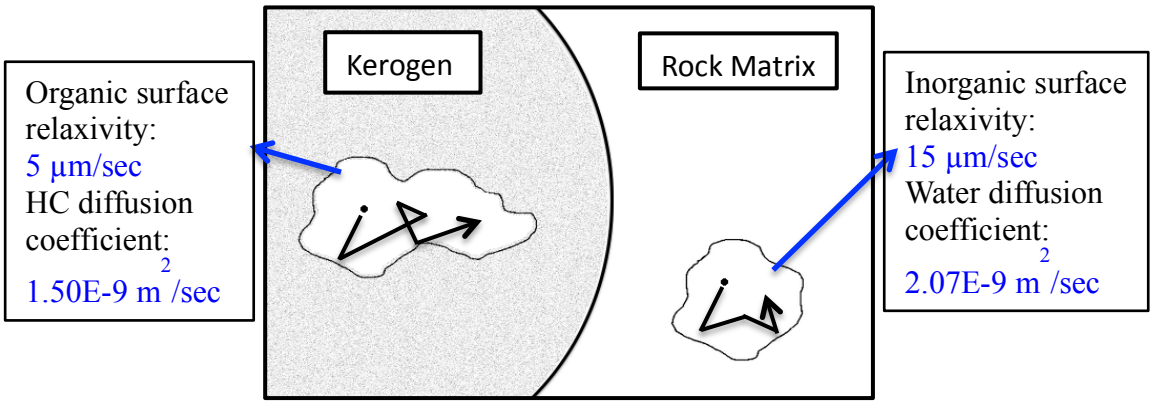

Fig. 2.2—The two-phase random-walk algorithm in hydrocarbon-wet organic pores and water-wet inorganic pores, for two-phase NMR simulation in organic-rich mudrock matrix.

2.4. Fluid Flow Simulations in Porous Media to Calculate Permeability

Palabos (2013), an open-source parallel Lattice Boltzmann solver, served to simulate the single-phase fluid flow in rock samples. The absolute permeability was then calculated using Darcy's law. The Lattice Boltzmann Method (LBM) (Degruyter et al.

2010) simulated the flow of Newtonian fluid by discretizing the Boltzmann equation on a lattice mesh, instead of solving the Navier-Stokes equations on a macroscopic level.

For all the rock matrices obtained from Imperial College London, the simulated LBM permeability results were in agreement with those reported by Dong (2007), using their LBM simulation code, and those reported by Mostaghimi et al. (2012) and Blunt et al., (2013), using a finite element method code developed at Imperial College London. These facts confirmed the accuracy of the LBM simulations. The LBM permeability data then served as the reference target for permeability estimates from NMR-based permeability models.

3. IMPACT OF MICRO-FRACTURES ON NMR RELAXOMETRY: FRACTURE-PORE DIFFUSIONAL COUPLING EFFECT*

NMR relaxometry, although among the most accurate methods to estimate formation porosity, have been considered as insensitive to the presence of micro-fractures. Hence, the NMR relaxometry in multiple-pore-type systems, which contain inter-granular pores, micro-fractures, or channel-like inclusions, have not been thoroughly investigated. NMR pore-scale simulations using a random-walk algorithm, enable us (a) to quantify the impact of micro-fractures/channels on NMR relaxometry, and (b) to propose a new concept of fracture-pore diffusional coupling in such heterogeneous systems.

In this research we randomly distributed and oriented micro-fractures (or channels) in 3D pore-scale images of different rock matrices. Then, we quantified the sensitivity of NMR T_2 (spin-spin relaxation time) distribution to the presence of micro-fractures (or channels), and compared the pore-scale simulation results against a previously published experimental study. The pore-scale simulation results from synthetic rock samples revealed that NMR T_2 distribution can be influenced not only by the conventional interpretations of pore size distribution, but also significantly by

---

* Part of this section is reprinted with permission from "Diffusional coupling between micro-fractures and pore structure and its impact on nuclear magnetic resonance measurements in multiple-porosity systems" by Lu Chi and Zoya Heidari, 2015. *Geophysics*, Vol 80(1): D31-D42. (http://dx.doi.org/10.1190/geo2013-0467.1) Copyright [2015] by Society of Exploration Geophysicists.

fracture-pore diffusional coupling. Furthermore, we developed a simplified one-dimensional (1D) analytical model for fracture-pore diffusional coupling. The analytical solutions of the 1D model were in agreement with the simulation results for the synthetic rock samples, which further demonstrate the existence of fracture-pore coupling in multiple-pore-type systems. The developed 1D model enables real-time evaluation of diffusional coupling effect in the presence of micro-fractures and complex pore-size distribution. The results are promising for future applications of NMR relaxometry to the assessment of micro-fracture content, when combined with other conventional well logs.

3.1. Literature Review

NMR relaxometry has been considered conventionally as insensitive to existence of fractures, so there have been very limited studies on quantifying the effect of fractures in porous media on NMR relaxometry. The few published NMR studies on fractures consider only wide, planar fractures, in which the saturating fluids behave as bulk fluids without spatial restrictions (Nakashima and Kikuchi 2007; Xiao and Li 2011). In other words, the fractures in those studies are considered as isolated from the porous structures of rock. Nakashima and Kikuchi (2007) evaluated the NMR response to wide planar fractures and proposed the use of borehole NMR measurements for assessment of fracture aperture. Xiao and Li (2011) systematically investigated the impact of fracture characteristics and tool parameters on NMR logs by theoretical analysis and numerical simulations. These studies assumed that (a) free fluids exclusively occupy the fracture space, and (b) the fractures are parallel to each other and dominantly perpendicular to the

wellbore. The findings from the aforementioned publications can only be applied to wide, planar fractures with apertures much greater than 0.2 mm, because a simple derivation shows that when the aperture is wider than 0.2 mm, the relaxation time associated to fractures approaches the bulk water relaxation time, i.e., 2 seconds, and becomes independent of aperture size (Nakashima and Kikuchi 2007; Xiao and Li 2011).

Other researchers studied the diffusional pore-to-pore exchange in non-fractured rock samples and its effect on NMR relaxometry. It has been demonstrated that intra- and inter-granular pores in heterogeneous, porous structures (e.g., carbonate rocks) can significantly influence the NMR T_2 distribution. Ramakrishnan et al. (1999) proposed an analytical model of diffusional pore coupling to describe the diffusion of water molecules between micro (intra-granular) and macro (inter-granular) pores in carbonate rocks. They observed that diffusional pore coupling can significantly decrease the longer relaxation time of macro-pores and suppress the peak amplitude of micro-pores, which have shorter relaxation time. Toumelin et al. (2002) further investigated the coupling between micro- and macro-porosities in carbonate rocks and reported the same decrease by Monte Carlo simulations and experimental measurements. Anand and Hirasaki (2005) studied the diffusional pore coupling in sandstones and grainstones, and verified the decrease in macropore relaxation times by mathematical modeling and experimental results. A recent laboratory study (Grunewald and Knight 2009) also confirmed the decrease in macropore relaxation times due to pore coupling by changing the surface geochemistry of porous materials.

None of these previous studies, however, took into account the micro-fractures in the rock. Thus, diffusional coupling effect between micro-fractures and rock pores has never been investigated. We hereby incorporated micro-fractures in porous media to investigate the diffusional coupling between micro-fractures and inter-granular pores, and quantified NMR sensitivity to the randomly distributed micro-fractures as well as the intra-/inter-granular pores. Based on the results, we proposed a new concept of fracture-pore diffusional coupling.

3.2. Theoretical Analysis

To substantiate our hypothesis that micro-fractures can influence the rock NMR signals, we start with a simple theoretical derivation. As discussed in Section 2, it has been well accepted that the NMR T_2 distribution represents the pore size distribution of the rock sample when (a) the pore space is fully saturated with fluids of high hydrogen index such as water or liquid hydrocarbon, (b) short TE in CPMG pulse sequence is used, and (c) all the pore surface has a uniform surface relaxivity ρ_2. Under these conditions the relaxation process is dominated by the surface relaxation mechanism, and the surface relaxation time, T_{2S}, can be considered as directly proportional to the pore size, given by

$$\frac{1}{T_{2S}} \propto \left(\frac{S}{V}\right)_{pore} \propto \left(\frac{1}{d}\right)_{pore}, \tag{3-1}$$

where d is the diameter of the pores. However, to validate the second part of Equation (3-1), another assumption must be made: all the pores are similar in geometry, thus they possess similar surface-to-volume ratios.

For instance, let us consider the case when thin planar fractures exist in rock samples together with the spherical inter-granular pores. The surface-to-volume ratios of spherical pores and planar fractures are given by

$$(\frac{S}{V})_{sphere} = (\frac{6}{d})_{sphere}, \tag{3-2}$$

and

$$(\frac{S}{V})_{plane} = (\frac{2}{w})_{plane}, \tag{3-3}$$

where w is the aperture of planar fractures. One can expect that if the diameter of spherical pores is three times of the aperture of planar fractures, they will overlap on T_2 distribution. In this case, if we still assume that the rock contains merely spherical pores, we may find mismatch between NMR T_2 distribution and pore size distribution of the rock.

The inherent assumption of similar pore geometry in Equation (3-1) makes the impact of micro-fractures on NMR T_2 distribution not discernable. The purpose of this study is therefore to evaluate (a) NMR sensitivity to the randomly distributed micro-fractures inside rocks, and (b) the diffusional coupling effect between micro-fractures

and inter-granular pores in various formations including sandstones, carbonates, and organic-rich mudrocks.

3.3. Synthetic Case No. 1: Sandstone Rock Sample

Synthetic case No. 1 is designed to illustrate the impact of micro-fractures in a porous media with highly connected inter-granular pore structure such as conventional sandstone reservoirs. We synthetically generate pore-scale images of fractured sandstone rocks, by inserting synthetic planar fractures into the sandstone matrix. The base micro-CT image of the sandstone rock sample was provided by the Pore-scale Modeling research group at Imperial College London (Dong 2007). We assigned four walkers in each pore voxel for NMR random-walk simulations.

Table 3.1—Sandstone rock sample: Calculated total porosity, pore T_2 value, coupled and isolated fracture T_2 values, fracture T_2 relative decrease compared to isolated fractures, and pore/fracture volume ratios calculated from images and estimated from NMR T_2 distributions, for the sandstone rock shown in Fig. 3.1.

Matrix	Sandstone, no fractures	Presence of 9-µm fractures	Presence of 12-µm fractures	Presence of 15-µm fractures
Porosity, %	16.86	18.57	19.15	19.73
Pore T_2, msec	106.3	97.5	106.3	106.3
Coupled Fracture T_2, msec	--	178	212	251
Isolated Fracture T_2, msec	--	274	354	421
Fracture T_2 decrease, %	--	35	40	40
Pore/Fracture Volume Ratio (Images)	--	8.01	5.97	4.75
Pore/Fracture Volume Ratio (NMR)	--	5.63	3.25	2.88

Fig. 3.1a shows the NMR T_2 distribution for the synthetic sandstone rock sample including and in the absence of planar fractures. The same figure also shows NMR T_2 distribution for the fractures isolated from the sandstone rock matrix. The two square planar fractures in the sandstone rock sample are identical in shape and size, with aperture of 9 μm and length of 270 μm. Relaxation times associated with the isolated planar fractures (blue dashed line) are longer than those of the original sandstone matrix (black dashed line, Fig. 3.1a). This is expected because the aperture of planar fractures, 9 μm, is larger than 1/3 of the dominant pore size in the sandstone rock sample, which is estimated as 14.9 μm. Also, we calculated the T_2 value of the isolated fractures analytically (Referring to Section 2.7.4). The results from analytical calculations confirm the simulation results for isolated fractures.

After incorporating the fractures into the sandstone matrix, the resulting T_2 distribution (blue solid line) is not equivalent to the superposition of the previously presented T_2 distributions (blue and black dash lines, Fig. 3.1a). Instead, the relaxation time corresponding to the planar fractures has been significantly shortened from 274 msec (isolated fractures) to 178 msec (coupled fractures). Meanwhile, the pore relaxation time has been slightly decreased. The T_2 values for inter-granular pores, coupled fractures, and isolated fractures are listed in **Table 3.1**.

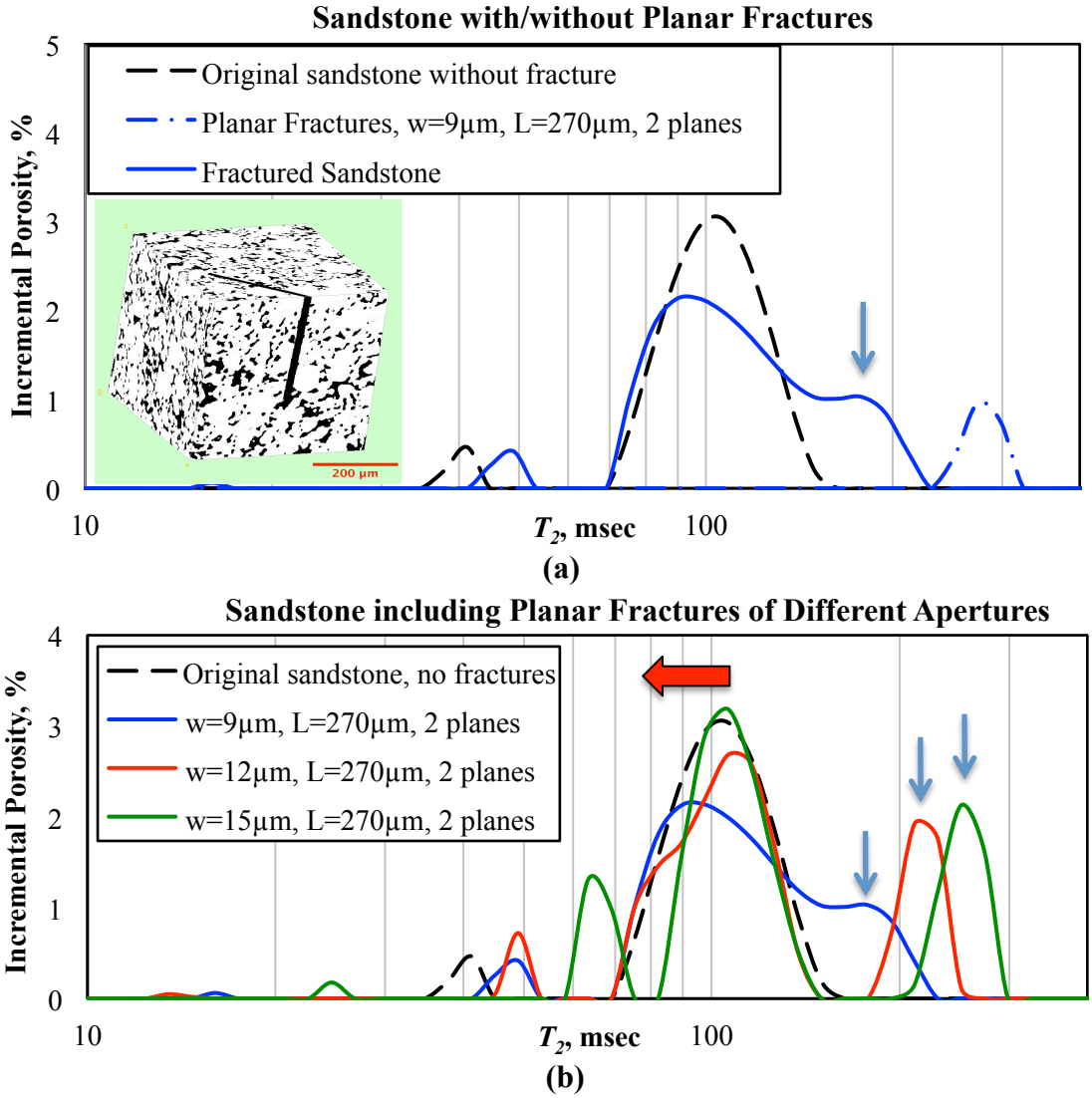

Fig. 3.1—Sandstone rock sample: Simulated NMR T_2 distribution (a) in the rock with two planar fractures (solid blue line) with aperture (w) of 9 µm and length (L) of 270 µm and without planar fractures (black dashed line). Blue dot-dashed line shows the simulated NMR T_2 distribution in the presence of only planar fractures. The blue arrows denote the T_2 peak corresponding to the planar fractures, which are diffusionally coupled with the pore system. The 3D pore-scale image on the left-hand side shows the sandstone example with two 9-µm planar fractures and (b) in the rock including two planar fractures with aperture (w) of 9, 12, or 15 µm, and length (L) of 270 µm. Three blue arrows denote the T_2 peaks for the planar fractures that are diffusionally coupled with the pore system. The area under each T_2 distribution curve represents the total porosity of the rock.

This significant decrease in the fracture T_2 relaxation time and the slight decrease in the pore relaxation time can be explained by the concept of diffusional coupling (Ramakrishnan et al. 1999). The physical origin of the decrease in longer T_2 is that, when the water molecules originally in large pores diffuse into small pores where they are exposed to more surfaces, their proton spins relax faster. This effect is obvious when the fluid diffusion rate is faster than the characteristic relaxation rate of pores (Ramakrishnan, et al 1999; Anand and Hirasaki 2005; Grunewald and Knight 2009). The slight decrease in shorter T_2 times observed in our simulation results (Fig. 3.1a) was also predicted by Ramakrishnans' theoretical analysis, but it was rarely mentioned or explained in literature. In conclusion, we demonstrated that the fracture-pore diffusional coupling exist in this sandstone example. Therefore, the diffusional pore-coupling concept, although proposed for bimodal pores in carbonate rocks, can be extended to explain NMR responses in fractured rocks.

Fig. 3.1b shows the impact of fracture aperture on NMR T_2 distribution. Shrinking fracture aperture leads to a more obvious decrease in sandstone pore relaxation times. When the fractures narrow from 15 μm, 12 μm, to 9 μm, the pore T_2 slightly shifts downward (i.e., from 106.3 msec to 97.5 msec, denoted by a red horizontal arrow). Specifically, in the case of 12 μm fractures (red line), the pore T_2 starts shifting downward as shown by the "shoulder peak" on the left. The reason is that as the fracture aperture approaches 1/3 pore size, the diffusional coupling between fractures and pores gets stronger, thus showing a more obvious pore T_2 decrease. Indeed,

the amount of exchanged fluid between fractures and pores becomes non-negligible when their sizes are similar, which promotes the fracture-pore coupling. Furthermore, Chang et al. (1997) published experimental results of real limestone samples including artificial fractures and showed the same decrease in relaxation times of limestone pores. Chang et al. (1997) provided T_2 distribution results for four Leuters limestone samples, three of which were made with artificial fractures with controlled apertures of 0.75 mm, 0.35 mm, and 0.25 mm, respectively. Their results show a visible decrease in the limestone T_2 relaxation times due to the existence of artificial fractures, in both water- and oil-saturated cases (i.e., from 3.1 msec to 2.5 msec in water-saturated case). Although the authors did not mention or explain this phenomenon, we found their experimental results in agreement with our simulation results and Ramakrishnan's (1999) analytical solutions. Again, these evidences demonstrate the existence of fracture-pore coupling effect in the fractured rocks.

We estimated the volume occupied by the inter-granular pores and the fractures, respectively, from NMR T_2 distribution of the sandstone example. We calculated the volumes by integrating the area below the T_2 curve that represents pores or fractures. In the 9 μm fracture case where the pore and fracture peaks are merged, we selected the saddle point (163 msec) as the T_2 cutoff value between the fractures and pores. Then, we integrated the areas above and below the T_2 cutoff value to calculate volumes of fractures and pores. The results (Table 3.1) show that the volume ratio of pores versus fractures (i.e. pore/fracture volume ratio) is underestimated by NMR T_2 distribution,

compared to the value calculated from the input images, for all three sandstone cases. This result is further substantiated by Ramakrishnan's (1999) observation that the amplitude of short T_2 peak gradually decreases when coupled with the long T_2 peak. This observation indicates that the volume fraction of the short T_2 component (i.e. inter-granular pores in this case) might be underestimated by more than 10% in NMR T_2 distribution when diffusional coupling exists.

3.4. Synthetic Case No. 2: Carbonate Rock Sample

This set of synthetic carbonate examples is designed to compare the impact of micro-fractures in carbonate rock samples with distinct pore-size distributions. We synthetically generated two pore-scale images of fractured carbonate rocks; one with small pores and the other one with large pores. The dominant inter-granular pore sizes are estimated as 10 μm and 57 μm, for the small-pore and large-pore carbonate rock samples, respectively. The base micro-CT images of the carbonate rock examples are provided by a project funded by Qatar National Research Fund (QNRF, Gupta et al. 2011). The synthetic micro-fractures are either planar fractures or channel-like inclusions.

3.4.1. Small-Pore Carbonate Example including Planar Fractures

This carbonate example illustrates the impact of micro-fractures in a porous media with poorly connected inter-granular pore structure. The volumetric Euler-Poincare Characteristic (EPC) method is used to quantify the pore connectivity in porous

media (Vogel 1997; Chi and Heidari 2015b), with lower value of EPC representing better pore connectivity. We calculated the volumetric EPC for the carbonate and the sandstone samples, which are -1.38×10^{-4} μm^{-3} and 4.37×10^{-4} μm^{-3}, respectively. It shows that the carbonate sample has poorly connected pores compared to the well-connected sandstone sample. The same sets of planar fractures, as used in the sandstone example (i.e. two identical planes with aperture of 9, 12, or 15 μm, and length of 270 μm), are inserted into the carbonate matrix. We assigned four walkers in each pore voxel for NMR random-walk simulations.

Fig. 3.2 shows the impact of fracture aperture on NMR T_2 distribution in the carbonate case. **Table 3.2** lists the T_2 values estimated for inter-granular pores, coupled fractures, and isolated fractures. We observe that, unlike the sandstone case, shrinking the fracture aperture has no impact on the carbonate pore relaxation times, i.e. the pore T_2 decrease is indiscernible. Meanwhile, the fracture T_2 decrease is less than that in the sandstone sample. We observed that, in the carbonate case the coupled fracture T_2 are decreased by 29% (Table 3.2) relative to the isolated fracture T_2, which is smaller than the 35%~40% decrease in the sandstone case (Table 3.1). Total porosity and inter-granular pore sizes are both similar for the carbonate and sandstone samples. However, the sandstone pore connectivity is much better than that in the carbonate sample. Consequently, we concluded that in the highly-connected pore structure, the fracture T_2 is shortened more significantly than in the poorly-connected pore structure. We attributed this observation to the stronger fracture-pore coupling in the better-connected

pore structure. Indeed, in a highly-connected pore space, the fluid molecules can migrate between fractures and pores more easily, which promotes the diffusional coupling between them.

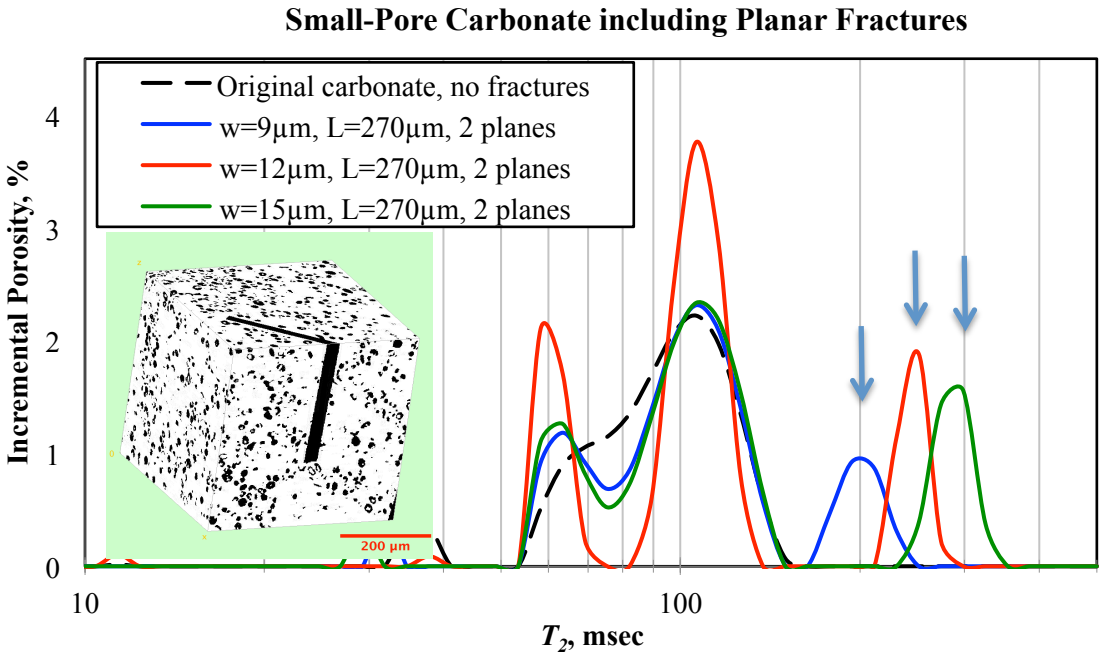

Fig. 3.2—Small-pore carbonate rock sample: Simulated NMR T_2 distribution for the synthetic carbonate example with planar fractures with aperture (w) of 9, 12, or 15 µm, and length (L) of 270 µm. Three blue arrows denote the T_2 peaks for the planar fractures, which are diffusionally coupled with the pore system. The 3D pore-scale image on the left-hand side shows the carbonate example with two 15-µm planar fractures. The area under each T_2 distribution curve represents the total porosity of the rock.

Table 3.2—Small-pore carbonate rock sample: Calculated total porosity, pore T_2 value, coupled and isolated fracture T_2 values, and fracture T_2 relative decrease compared to isolated fractures, for the sandstone rock shown in Fig. 3.2.

Matrix	**Small-pore carbonate, no fractures**	**Presence of 9-µm fractures**	**Presence of 12-µm fractures**	**Presence of 15-µm fractures**
Porosity, %	15.70	17.44	18.02	18.60
Pore T_2, msec	106.3	106.3	106.3	106.3
Coupled Fracture T_2, msec	--	194	251	298
Isolated Fracture T_2, msec	--	274	354	421
Fracture T_2 decrease, %	--	29	29	29

3.4.2. Small-Pore Carbonate Example including Channel-like Inclusions

This example illustrates the impact of micro-inclusions with apertures close to the size of inter-granular pores, on NMR T_2 distribution. Channel-like inclusions, with radius of 3 µm and length of 150 µm, are inserted into the carbonate rock as a special form of micro-fractures in this example. It can be shown that channel-like inclusions and planar fractures have similar impact on NMR T_2 distribution by comparing Equation (3-11) to Equation (3-13) in the Section 3.7.4. The relaxation times for both of them are solely affected by the size of their smallest dimension, which is the diameter of a cylindrical channel, or the aperture of a planar fracture. Consequently, all the conclusions previously drawn for planar fractures can be applied to channel-like inclusions. We assigned four walkers in each pore voxel for NMR random-walk simulations in this synthetic example.

Fig. 3.3 shows the impact of channel-like inclusions on NMR T_2 distribution of the carbonate example, which is simply an overlap of T_2 peaks for channels and inter-granular pores (both located at 106.3 msec). Although, the amplitude of T_2 peak increases with higher concentration of inserted channels, the channels and inter-granular pores cannot be distinguished from the T_2 distribution in this case. **Table 3.3** shows the calculated total porosity, pore T_2 value, and coupled channel T_2 values for the carbonate example.

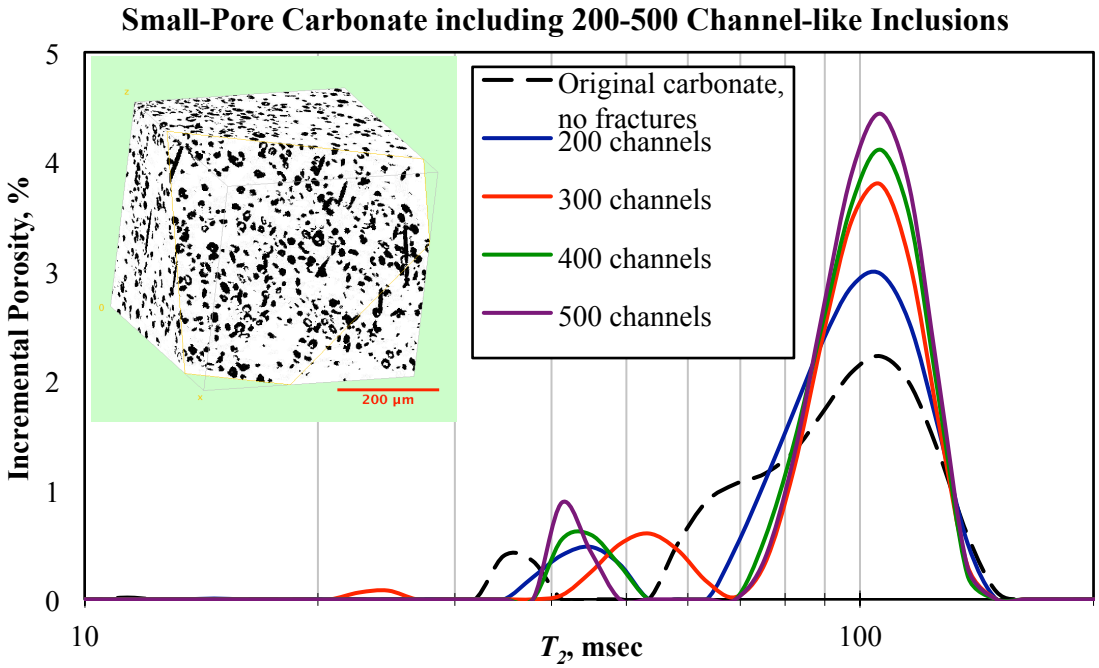

Fig. 3.3—Small-pore carbonate rock sample: Simulated NMR T_2 distribution for the carbonate example including 200-500 channel-like inclusions. The 3D pore-scale image on the left-hand side shows the carbonate pore structure including 500 channels. The area under each T_2 distribution curve represents the total porosity of the rock.

Table 3.3—Small-pore carbonate rock sample: Calculated total porosity, pore T_2 value, and coupled channel T_2 values for the carbonate rock shown in Fig. 3.3.

Matrix	Small-pore carbonate, no fractures	Presence of 200 channels	Presence of 300 channels	Presence of 400 channels	Presence of 500 channels
Porosity, %	15.70	17.47	18.35	19.25	20.02
Pore T_2, msec	106.3	106.3	106.3	106.3	106.3
Coupled Channel T_2, msec	--	106.3	106.3	106.3	106.3

The major difference between planar fractures and channel-like inclusions is that, given the same surface-to-volume ratio, a planar fracture occupies a larger volume than a cylindrical channel, so the NMR T_2 distribution is more sensitive to planar fractures. In other words, planar fractures can be considered as expanded cylindrical channels.

3.4.3. Large-Pore Carbonate Example including Planar Fractures

In this example, we use a large-pore carbonate matrix to study the effect of thin micro-fractures on large pores. In this synthetic case, the total volume of micro-fractures are kept the same, while the impact of fracture aperture on NMR T_2 distribution is evaluated. Square planar fractures with different aperture (i.e., 3 μm, 6 μm, or 9 μm) and the same length (150 μm) are inserted into the large-pore carbonate matrix. The aspect ratios (aperture-to-length ratio) of these fractures change from 0.02 to 0.04 to 0.06. The number of fractures is varied (i.e., 60, 30, or 20 fractures) to maintain the same total porosity. We assigned one walker in each pore voxel for NMR random-walk simulations in this case.

Fig. 3.4 shows the simulation results for different fracture sizes. Three blue arrows denote the T_2 peaks of the planar fractures. By theoretical calculation (see Section 3.7.4) for the 3 μm fractures, and separate numerical simulation on a cubic volume containing only the 3 μm fractures, we determined that the 3 μm fractures are located at T_2 = 107 msec. Also 6 μm and 9 μm fractures are determined and labeled in the same way. The second blue T_2 peak (w = 3 μm case) in the middle is caused by original carbonate pores, which has the same origin as the small black peak. This middle peak disappears in the red (6 μm) and green (9 μm) cases because it merges with the fracture T_2 peaks.

In the presence of thin planar fractures, relaxation times of the large inter-granular pores are more significantly decreased compared to the case of thick fractures. For example, the third blue T_2 peak in the w = 3 μm case represents the carbonate inter-granular pores. When no fractures exist, this carbonate pore peak is located where the largest black peak is; after fracturing, the peak is shifted downwards by fracture-pore coupling. The pore T_2 peak is shifted downwards by 11%, 21%, and 29% from its original position in the presence of 9-μm, 6-μm, and 3-μm planar fractures, respectively (**Table 3.4**). Again, this is explained by the fluid diffusion between fractures and pores– when the water molecules diffuse from large pores to thin fractures, they experience a larger surface area that makes the proton spins relax faster. The thinner fractures have larger surface-to-volume ratio, thus they relax the protons originally from large pores faster than thicker fractures. In other words, the relaxation time of the long-time

component reflects an averaging of the sizes of heterogeneous porous structures when diffusional coupling exists.

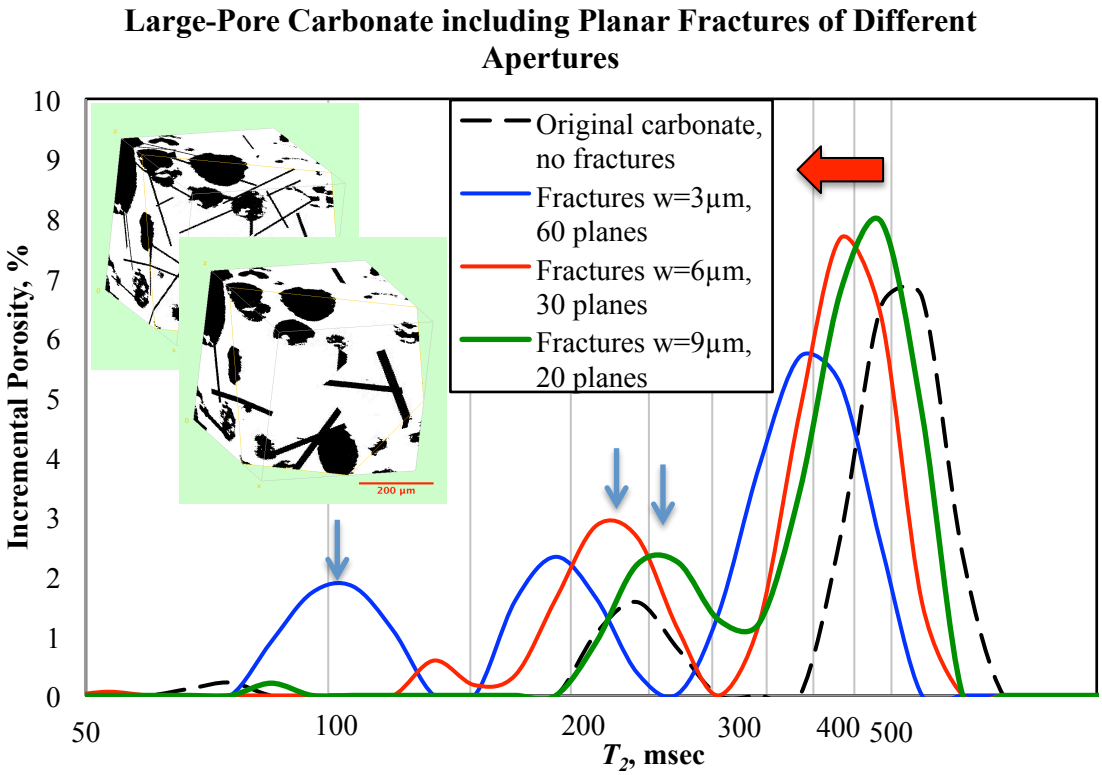

Fig. 3.4—Large-pore carbonate rock sample: Simulated NMR T_2 distribution for the synthetic large-pore carbonate example, in presence of planar fractures of different apertures. The planar fractures take an aperture (w) of 3, 6, or 9 µm, and keep the same length (L) of 150 µm. The number of planar fractures is 60, 30, or 20 for the three cases, respectively, to maintain a constant total porosity. Three blue arrows denote the T_2 peaks representing the planar fractures that are coupled with the pore system. The red arrow indicates that thin fractures can shorten the pore T_2 more than thick fractures. The 3D pore-scale images on the left-hand side show the carbonate pore structure including planar fractures with apertures of 3 µm (left) and 9 µm (right image). The area under each T_2 distribution curve represents the total porosity of the rock.

Table 3.4—Large-pore carbonate rock sample: Calculated total porosity, pore T_2 value, pore T_2 relative decrease compared to the original value, and coupled fracture T_2 values for the large-pore carbonate rock example shown in Fig. 3.4.

Matrix	Large-pore carbonate, no fractures	Presence of 3-µm fractures (60 fractures)	Presence of 6-µm fractures (30 fractures)	Presence of 9-µm fractures (20 fractures)
Porosity, %	21.98	31.11	30.96	30.96
Pore T_2, msec	546.1	385.3	432.8	486.1
Pore T_2 decrease, %	--	29	21	11
Coupled Fracture T_2, msec	--	107.2	215.4	271.8

Table 3.5—Large-pore carbonate rock sample: Calculated total porosity and pore T_2 values for the large-pore carbonate example in Fig. 3.5.

Matrix	Porosity, %	Pore T_2, msec
Large-Pore Carbonate, no fractures	21.98	540.1
Presence of 100 channel-like fractures	22.84	523.7
Presence of 200 channel-like fractures	23.63	523.7
Presence of 300 channel-like fractures	24.47	507.8
Presence of 400 channel-like fractures	25.29	507.8
Presence of 500 channel-like fractures	25.99	492.4
Presence of 600 channel-like fractures	27.74	463.0

3.4.4. Large-Pore Carbonate Example including Channel-like Inclusions

In this synthetic case, the same sets of channel-like inclusions with radius of 3 µm and length of 150 µm, as used in the small-pore carbonate example, are inserted into the large-pore carbonate rock. We assigned one walker in each pore voxel for NMR random-walk simulations.

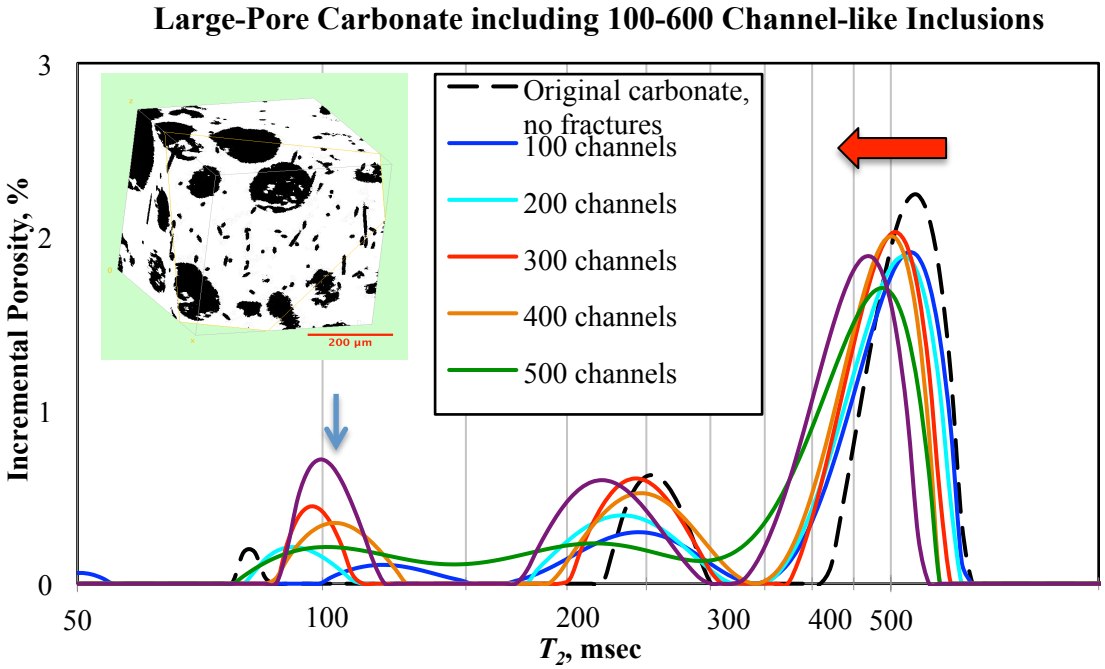

Fig. 3.5—Large-pore carbonate rock sample: Simulated NMR T_2 distribution for the synthetic large-pore carbonate example including 100-600 channel-like inclusions. The red arrow denotes that pore T_2 decreases as more fractures are inserted into the matrix, and the blue arrow indicates the fracture T_2 location at around 100 msec. The 3D pore-scale image on the left-hand side shows the large-pore carbonate sample including 500 channels. The area under each T_2 distribution curve represents the total porosity of the rock.

Fig. 3.5 shows the impact of volumetric concentration of micro-inclusions on NMR T_2 distribution in the large-pore carbonate sample. **Table 3.5** lists the T_2 values estimated for inter-granular pores. When thin channel-like fractures are inserted into the carbonate rock, the upper peak associated with the inter-granular pores is shifted downwards. Having more channels inserted into the carbonate rock, the upper peak shifts more significantly (i.e. denoted by the red arrow). Table 3.5 lists the estimated pore T_2 values and their corresponding decrease due to the increase in channels. The results indicate that in the presence of higher volumetric concentration of micro-fractures,

the fracture-pore coupling becomes stronger, causing the fluids in the large pores relax faster. In this case, one will significantly underestimate the pore size based on NMR T_2 distribution by up to 14%, if one ignores the micro-fractures (channel-like inclusions) and assume only spherical inter-granular pores in the rock.

3.5. Synthetic Case No. 3: Organic-rich Mudrock Sample

The organic-rich mudrock matrix is synthetically generated to study the impact of micro-fractures on NMR relaxation measurements in organic-rich mudrock formations, in which the pore size is extremely small. We assumed that volumetric concentration of kerogen and matrix porosity are 15% and 10%, respectively. Matrix porosity is assumed to be water-saturated. The inter-granular pores in the mudrock matrix are designed to be very small (0.05~0.1μm). We did not take into account the kerogen porosity in random-walk simulations. Two sets of double planar fractures, with narrow (0.45μm) or wide (0.75μm) apertures and with length of 13.5 μm, are synthetically inserted into the mudrock matrix. We assigned five walkers in each pore voxel for NMR random-walk simulations. **Fig. 3.6a** shows the 3D pore-scale images of the synthetic organic-rich mudrock sample before and after inserting the 0.75-μm wide micro-fractures.

Fig. 3.6b shows the impact of micro-fracture aperture on NMR T_2 distribution in organic-rich mudrocks. Similar to the small-pore carbonate example, the pore T_2 remains almost intact at its original position of 1.2 msec before and after inserting the micro-fractures. But T_2 values of the coupled fractures are significantly decreased by

75%~78% compared to the T_2 values of isolated fractures (**Table 3.6**), due to the fracture-pore diffusional coupling.

Furthermore, we calculated the volume occupied by the inter-granular pores and the fractures, respectively, from NMR T_2 distribution. The results show that, the volume ratio of pores versus fractures has decreased from 4.74 (calculated from images) to 2.04 (estimated from NMR T_2 distribution) in the presence of 0.45-μm fractures, and from 2.81 (from images) to 1.55 (from NMR) in the presence of 0.75-μm fractures (Table 3.6). Consequently, the volume occupied by the shorter T_2 component (inter-granular pores) might be significantly underestimated by NMR T_2 distribution when diffusional coupling exists. This result is further substantiated by Ramakrishnan's observation that the short T_2 peak, corresponding to micropores, decreases in amplitude when coupled with the upper peak corresponding to macropores.

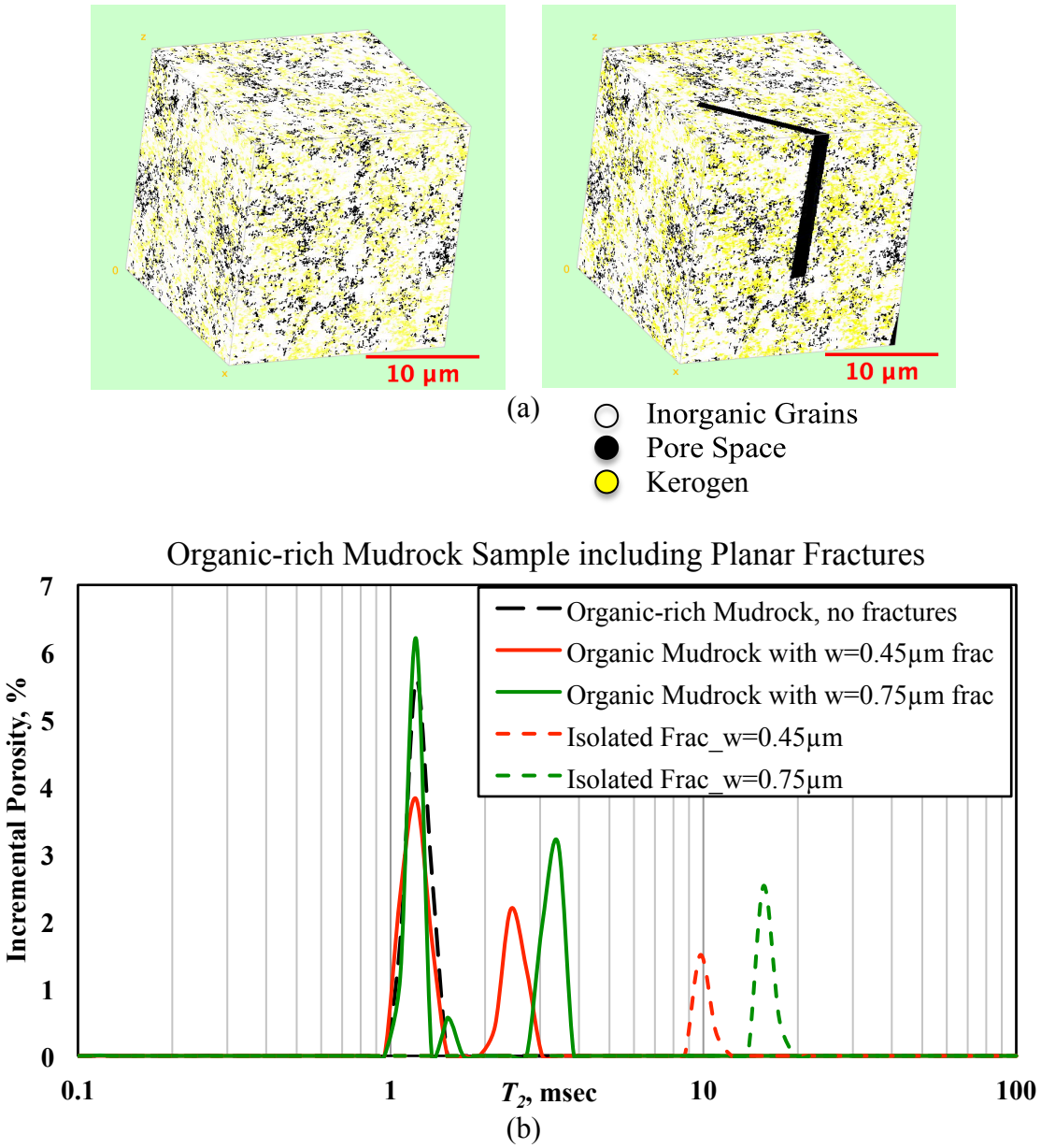

Fig. 3.6—Organic-rich mudrock sample: (a) the 3D pore-scale images of the organic-rich mudrock sample with no fractures (left) and including 0.75-µm wide planar fractures (right). Black, white, and yellow regions represent pore space, inorganic grains, and kerogen, respectively. (b) Simulated NMR T_2 distribution for the synthetic organic-rich mudrock example including planar fractures with aperture (w) of 0.45 or 0.75 µm, and length (L) of 13.5 µm. The green and red dash curves show the isolated planar fractures with aperture of 0.45 or 0.75 µm.

Table 3.6—Organic-rich mudrock example: Calculated total porosity, pore T_2 value, coupled and isolated fracture T_2 values, fracture T_2 relative decrease compared to the case of isolated fractures, and pore-to-fracture volume ratios calculated from images and from NMR T_2 for the organic-rich mudrock example shown in Fig. 3.6.

Matrix	**Organic-rich Mudrock, no fractures**	**Presence of 0.45-µm planar fractures**	**Presence of 0.75-µm planar fractures**
Porosity, %	10.00	11.84	13.07
Pore T_2, msec	1.20	1.20	1.20
Coupled Fracture T_2, msec	--	2.42	3.43
Isolated Fracture T_2, msec	--	9.77	15.56
Fracture T_2 Decrease, %	--	75	78
Pore/Fracture Volume Ratio (Images)	--	4.74	2.81
Pore/Fracture Volume Ratio (NMR)	--	2.04	1.55

3.6. Analytical Model for Fracture-Pore Diffusional Coupling

3.6.1. Model Introduction

The 1D analytical model for the fracture-pore diffusional coupling effect used in this study was adapted from a previous model introduced by Ramakrishnan et al. (1999). Ramakrishnan's model described the pore coupling between macropores (inter-granular) and micropores (intra-granular pores) in carbonate rocks. We adapted this model to study the diffusional coupling between micro-fractures and inter-granular pores in various rock samples. **Fig. 3.7** shows the assumed 1D simplified model for the fractured rock sample. The magnetization in the fracture domain, M_F, is governed by the usual NMR diffusion equation:

$$D\frac{\partial^2 M_F}{\partial x^2} - \frac{M_F}{T_{2B}} = \frac{\partial M_F}{\partial t}, \tag{3-4}$$

where D is the diffusion coefficient of fluids within the fractures.

Within the porous grains, the magnetization M_G, is governed by the modified NMR diffusion equation:

$$\frac{D}{F}\frac{\partial^2 M_G}{\partial x^2} - \phi_G M_G\left(\frac{1}{T_{2B}} + \frac{1}{T_{2,G}}\right) = \phi_G \frac{\partial M_G}{\partial t}, \tag{3-5}$$

where $T_{2,G}$ is the relaxation time of fluids within the inter-granular pores, and F and ϕ_G are the formation factor and the inter-granular porosity of the porous grain domain, respectively.

The boundary conditions between the fracture domain and the porous grain domain can be expressed as

$$M_F\Big|_{x=h} = M_G\Big|_{x=h}, \tag{3-6}$$

and

$$D\frac{dM_F}{dx}\bigg|_{x=h} = \frac{D}{F}\frac{dM_G}{dx}\bigg|_{x=h} + \rho(1-\phi_G)M_F\Big|_{x=h}, \tag{3-7}$$

where ρ is the surface relaxivity of the grains, and h is half the aperture of fractures given by $h = w/2$.

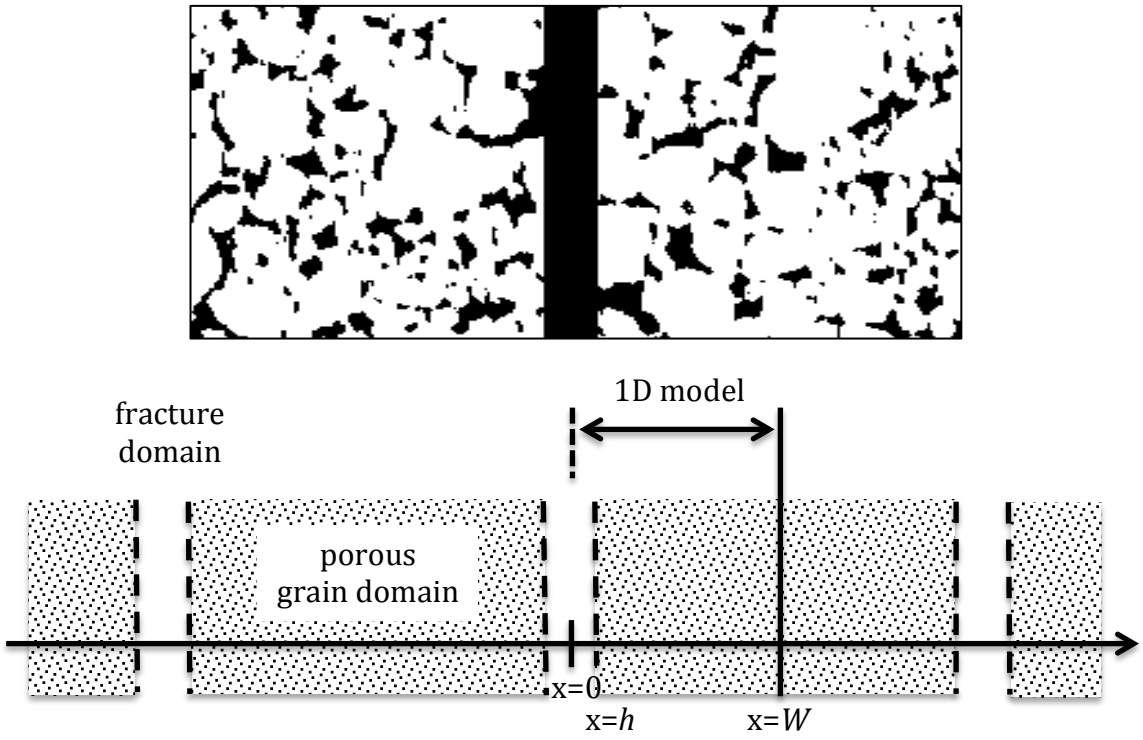

Fig. 3.7—Simplified 1D model for a fractured rock matrix. The values on the x-axis are used to denote the relative dimensions of fractures and grains. *W* is the distance from fracture center to grain center, and *h* is half the aperture of fractures.

According to Ramakrishnan's paper, the approximate analytical solutions to Equations (3-4) and (3-5) can be obtained by assuming two principal exponential-decay modes. First, we defined "coupled fractures" as the micro-fractures that are diffusionally coupled (i.e. connected) with inter-granular pores. Next, we adopted Ramakrishnan's approximate analytical solution to obtain the relaxation time for the coupled fractures, $T_{2F,coupled}$, via

$$\frac{1}{T_{2F,coupled}} \cong \frac{1}{h}\left[\sqrt{\frac{\phi_G D}{T_{2,G} F}} + \rho(1-\phi_G)\right]. \tag{3-8}$$

Equations (3-4) to (3-8) are adapted from Ramakrishnan's work (1999), by replacing their terms for micro- and macro-pores with our definitions of inter-granular pores and micro-fractures, respectively.

In comparison, if the micro-fractures are not connected to any inter-granular pores, we defined them as "isolated fractures". The relaxation time of fluids within the isolated fractures, $T_{2F,iso}$, can be theoretically estimated by

$$\frac{1}{T_{2F,iso}} = \rho \cdot \frac{2}{w} = \frac{\rho}{h}, \tag{3-9}$$

It can be easily shown that when the grain porosity, ϕ_G, approaches zero, Equation (3-8) naturally becomes Equation (3-9), which describes isolated micro-fractures.

The amplitude of T_2 mode in the isolated micro-fractures, I_{iso}, can be determined from the input geometry. The amplitude of T_2 mode in the coupled micro-fractures, $I_{coupled}$, is then derived using the analytical model, given by (Ramakrishnan et al. 1999)

$$I_{coupled} \cong I_{iso} \frac{(1+X)^2}{1+X/2}, \tag{3-10}$$

where

$$X \cong \frac{T_{2,G} / T_{2F,coupled}}{\sqrt{1 - T_{2,G} / T_{2F,coupled}}}.$$

3.6.2. Comparison of NMR Simulation Results Against Analytical Model

We further compared my NMR simulation results against the 1D analytical solution described in the previous section. **Tables 3.7** and **3.8** list the assumed parameters for the analytical model. We assumed a typical formation factor of 25 for the sandstone example (Ramakrishnan et al. 1999), a formation factor of 0.85 for the fractures in the large-pore carbonate example, and a value of 40 for the inter-granular pores in the synthetic organic-rich mudrock example. It should be noted that the assumed formation factor of the porous grain domain has significant influences on the estimates of T_2 mode.

Table 3.7—Parameters assumed in the analytical models for the sandstone and large-pore carbonate examples.

Parameters	Sandstone example (with 9, 12, and 15 μm fractures)	Large-pore carbonate example (with 3, 6, and 9 μm fractures)
T_{2B}, s	3.1	3.1
D, μm^2/s	2070	2070
ρ, μm/s	10	10
H, μm	4.5, 6, and 7.5 (fractures)	28.5 (pores)
ϕ_G, %	16.51, 16.40, and 16.30 (pores)	9.13, 8.98, and 8.98 (fractures)
$T_{2,G}$, s	0.106	0.107, 0.215, and 0.272
F	25 (inter-granular pores)	0.85 (fractures)

Table 3.8—Parameters assumed in the analytical models for the synthetic organic-rich mudrock example.

Parameters	Synthetic organic-rich mudrock example (with 0.45 μm and 0.75 μm fractures)
T_{2B}, s	3.1
D, μm^2/s	2070
ρ, μm/s	15
H, μm	0.45 and 0.75 (fractures)
ϕ_G, %	9.78 and 9.63 (inter-granular pores)
$T_{2,G}$, s	0.106
F	40 (inter-granular pores)

We first compared the simulation results against the analytical solution in the sandstone case (i.e. previously shown in Fig. 3.1b). **Fig. 3.8** shows an agreement between the analytical T_2 modes (black arrow and red bars) and the simulated T_2 distribution (dashed, solid and dot-dashed curves) for the fractured sandstone example. Note that the areas under the T_2 distribution curves represent the porosity of the rock, i.e. the area under the coupled curves is equal to summation of areas under the isolated

curves. Meanwhile, the amplitude of T_2 modes represents the volume fraction (porosity) of each mode. Therefore, the analytical T_2 modes not only match the T_2 peak positions, but also predict the change in volume fraction of each mode.

Next, we compared the numerical simulation results against the analytical model for the large-pore carbonate example (i.e., previously shown in Fig. 3.4). In this case, the role of micro-fractures and inter-granular pores in the 1D analytical model is indeed switched, i.e. the micro-fractures are the short-time mode, while the inter-granular pores are the long-time mode. **Fig. 3.9** shows the comparison between the analytical T_2 modes (black arrow and red bars) and the simulated T_2 distribution (dashed and solid curves) of the large-pore carbonate rock sample including thin planar fractures. The results demonstrate that analytical T_2 modes are in agreement with the simulated T_2 distribution in the large-pore carbonate case, which further confirms the existence of fracture-pore diffusional coupling.

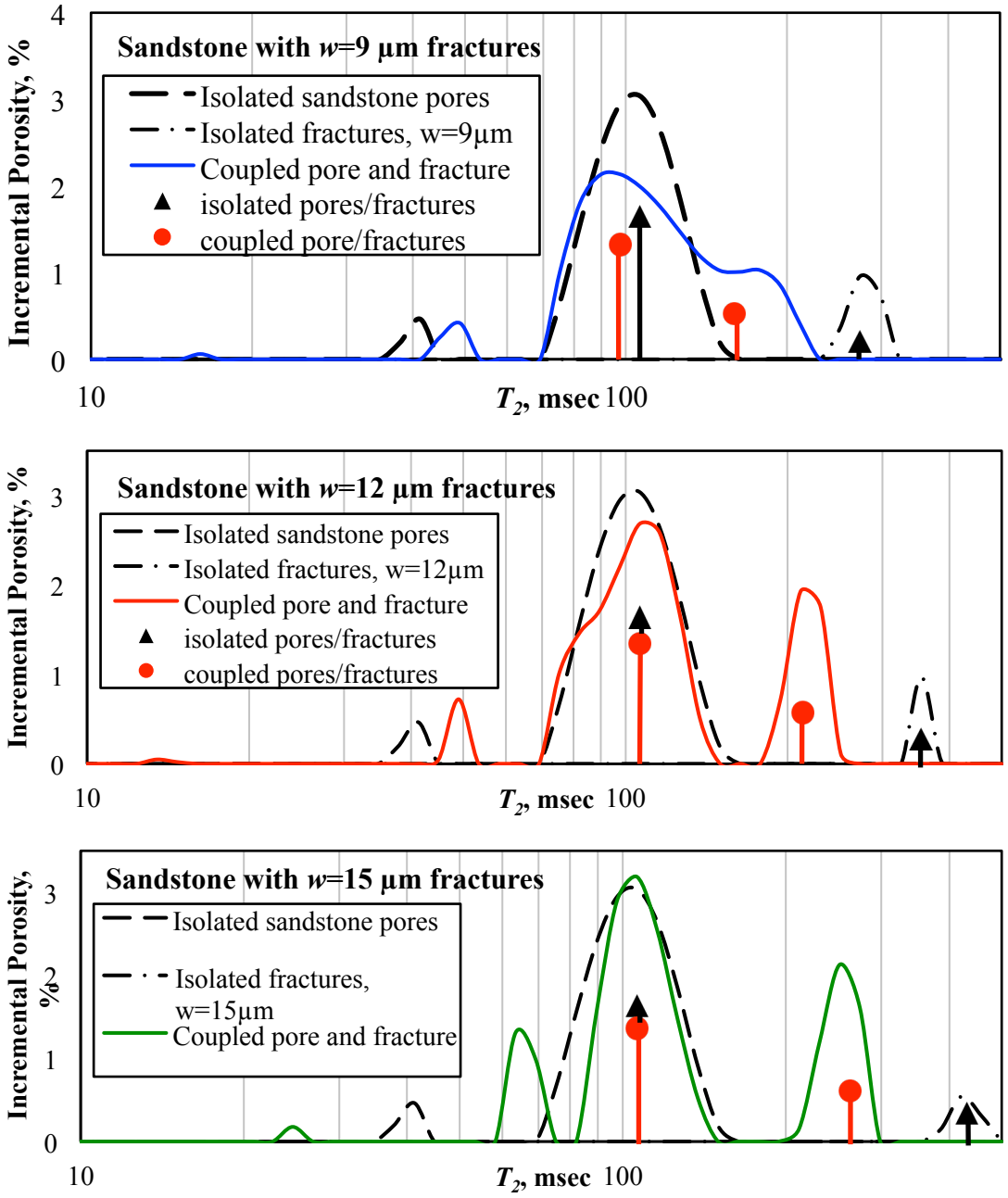

Fig. 3.8—Analytical T_2 modes and simulated T_2 distributions for the sandstone rock sample including planar fractures with aperture (w) of 9, 12, or 15 µm, and length (L) of 270 µm. The black arrow bars represent the T_2 modes for isolated sandstone pores or fractures, and the red bars show coupled fractures or pores. The T_2 curves are the same as in Fig. 3.1b, showing the simulated T_2 distributions for the isolated sandstone pores (dashed), coupled pores-fractures (solid lines), and isolated fractures (dot-dashed), respectively. The area under each T_2 distribution curve represents the total porosity of the rock.

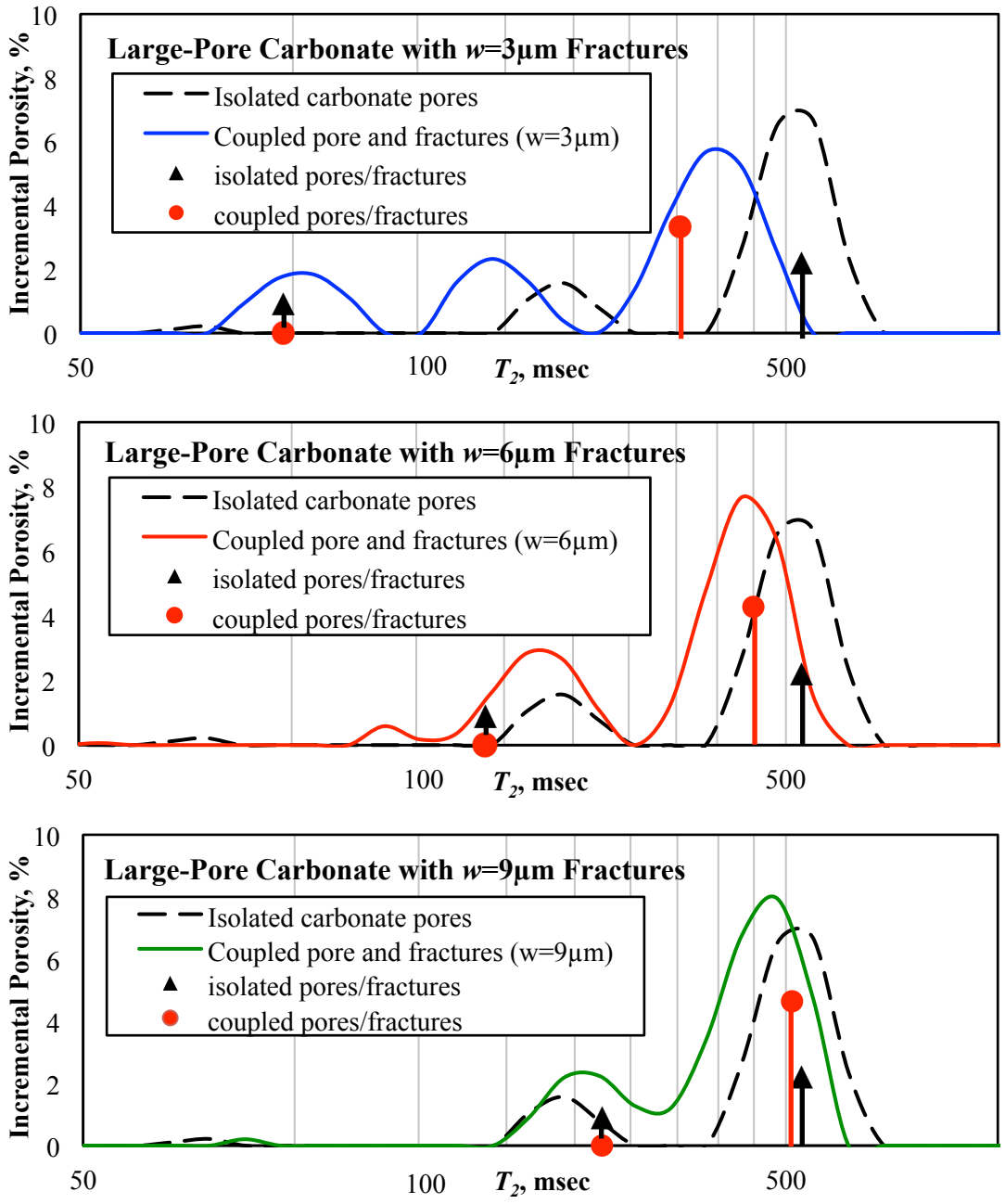

Fig. 3.9—Analytical T_2 modes and simulated T_2 distributions for the carbonate rock sample including planar fractures with aperture (w) of 3, 6, or 9 µm, and length (L) of 150 µm. The black arrow bars represent the analytical T_2 modes for isolated carbonate pores or fractures, and the red bars show coupled fractures or pores. The T_2 curves are the same as in Fig. 3.4 showing the simulated T_2 distributions for the isolated carbonate pores (dashed) and coupled pores-fractures (solid lines), respectively. The area under each T_2 distribution curve represents the total porosity of the rock.

At last we compared the numerical simulation results against the analytical model for the synthetic organic-rich mudrock example (i.e., previously shown in Fig. 3.6b). This case is similar to the sandstone case, where the micro-fracture aperture is larger than the original mudrock pores, therefore the micro-fractures are the long-time mode and the inter-granular pores are the short-time mode. **Fig. 3.10** shows the comparison between the analytical T_2 modes (black arrow and red bars) and the simulated T_2 distribution (dashed and solid curves) of the synthetic organic-rich mudrock sample including thick planar fractures. Again, the analytical T_2 modes reasonably match the simulated T_2 distribution in the organic-rich mudrock case.

It should be emphasized that the analytical T_2 bars shown in all the cases in this section (Figs. 3.8 to 3.10) are the approximate analytical solutions of the simplified 1D model. Thus, when comparing the T_2 modes from 1D simplified model to the simulation results in 3D volume, the agreement might not be perfect. Ramakrishnan et al (1999) proposed that the accurate solutions to the 1D model can be derived by Laplace transform of Equations (3-4) to (3-7), and then final solutions can be obtained by contour integration or numerical Laplace inversion.

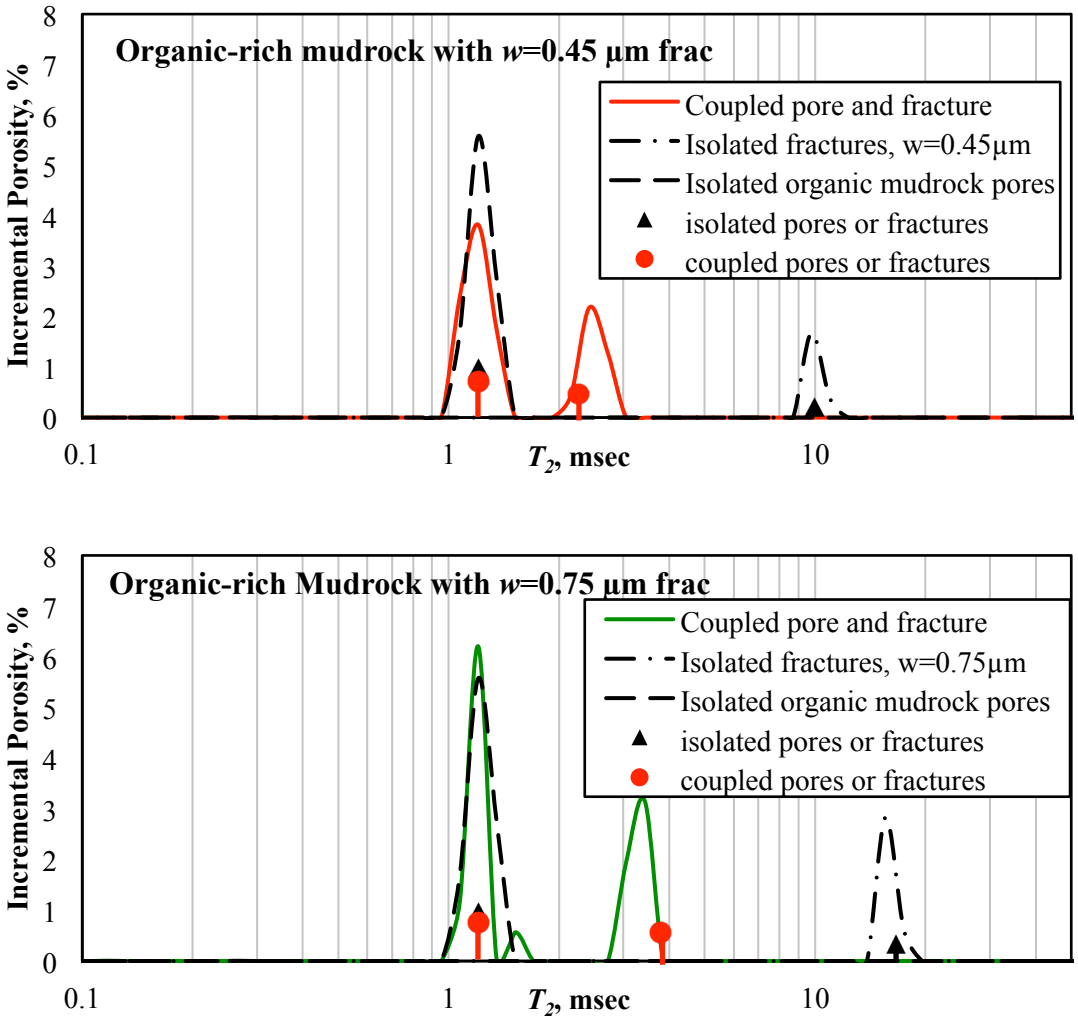

Fig. 3.10—Analytical T_2 modes and simulated T_2 distributions for the organic-rich mudrock sample including planar fractures with aperture (w) of 0.45 or 0.75 µm, and length (L) of 15 µm. The black arrow bars represent the analytical T_2 modes for isolated carbonate pores or fractures, and the red bars show coupled fractures or pores. The T_2 curves are the same as in Fig. 3.6b, showing the simulated T_2 distributions for the isolated mudrock pores (dashed black lines), the isolated micro-fractures (dot-dashed black lines), and the coupled pores-fractures (solid lines), respectively. The area under each T_2 distribution curve represents the total porosity of the rock.

3.7. Discussions

3.7.1. Uniformness of Micro-Fracture Aperture

All the randomly distributed and oriented micro-fractures considered in this study were uniform in aperture or radius. To investigate the impact of non-uniform fractures on NMR T_2 distribution, we also synthesized planar fractures with variable apertures and constant length of fractures in the large-pore carbonate rock sample. Apertures of synthetic micro-fractures were randomly generated based on Gaussian normal distribution. We assumed a mean value of 6 μm or 9 μm and a 3 μm deviation from mean value. The NMR simulation results (**Fig. 3.11**) showed that the T_2 distribution in such fractured rocks appear to be similar to those with uniform fractures of 6-μm or 9-μm aperture (Fig. 3.4). The pore T_2 of rocks with non-uniform or uniform fractures is the same in particular. The T_2 distribution can, however, get affected by non-uniform fractures in the case of a wide range of fracture aperture. Indeed, in the presence of a wide range of fracture apertures, the diffusional coupling (a) between fractures and inter-granular pores, and (b) between fractures with different apertures (if connected) will cause uncertainty in interpretation of NMR response.

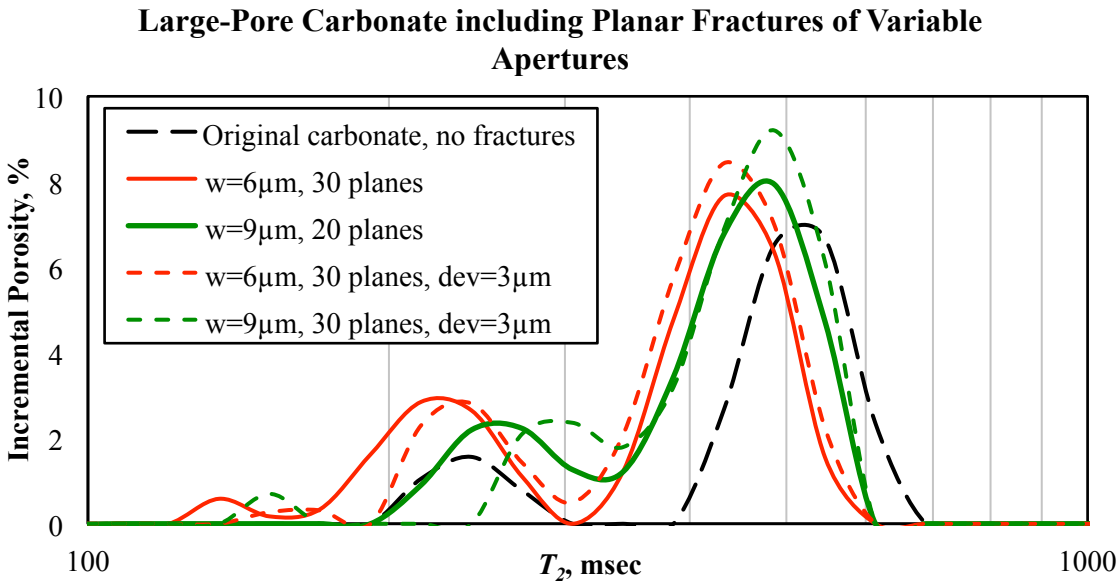

Fig. 3.11—Large-pore carbonate rock sample: Simulated NMR T_2 distribution for the synthetic large-pore carbonate example, in presence of planar fractures of variable apertures. The red dashed curve shows the carbonate sample including 30 planar fractures, with a mean aperture (w) of 6 µm and a 3-µm deviation from the mean value. The green dashed curve shows 20 planar fractures, with a mean aperture (w) of 9 µm and a 3-µm deviation. They all keep the same length (L) of 150 µm. The red and green solid curves show the same uniform-aperture planar fractures as in Fig. 3.4. The area under each T_2 distribution curve represents the total porosity of the rock.

3.7.2. Aspect Ratio of Micro-Fracture

In this study we differentiated micro-fractures and pores by aspect ratio and shape. Micro-fractures refer to pores with low aspect ratio, for example, with aspect ratio of less than 0.1, which is significantly less than that of pores. Some grain contact asperities might also form porous space, and they can be considered as micro-fractures as long as they are thin and long enough. By such definition, we believe the fracture-pore coupling effect exist in a wide variety of multiple-pore-type systems, for example, micro-fractured grains in tight sands or deformation bands. The theoretical results reported in this study can be utilized to explain pore-coupling phenomena in such complicated systems. Furthermore, the outcomes of this research potentially enables quantifying volumetric concentration of micro-fractures using NMR, when combined with other well logs such as electromagnetic measurements. Such discrimination between micro-fractures and pores can facilitate the analysis of pore connectivity and topology, which in turn can enhance interpretation of other borehole geophysical measurements such as electromagnetic and acoustic measurements.

3.7.3. Surface Relaxivity of Rock Samples

In this study we did not investigate the influence of surface relaxivity values on the NMR response. However, we expected that with higher surface relaxivities, the pores and fractures become less coupled with each other. Ramakrishnan et al. (1999) reported that surface relaxivity values can be crucial to the degree of diffusional coupling

between macro- and micro-pores. High surface relaxivity can reduce the diffusion length of water molecules and thus hinder the coupling between micro- and macro-pores.

The surface relaxivity of carbonate rocks typically ranges from 1 to 10 μm/sec (Talabi 2008), and for sandstone rocks it can vary from 9 μm/sec (Liaw et al. 1996) to 46 μm/sec (Roberts et al. 1995). We assumed a surface relaxivity of 10 μm/sec for both sandstone and carbonate rocks for convenience of comparison. In the synthetic organic-rich mudrock example, we assumed the surface relaxivity of the inorganic pore space to be 15 μm/sec, which can be varied depending on different lithology.

3.7.4. Calculation of NMR Relaxation Times for Isolated Fractures

Theoretically, we can estimate the T_2 value for the planar fractures in Fig. 3.1a by combining Equations (1-9) and (3-3), which results in

$$\frac{1}{T_2} = \frac{1}{T_{2B}} + \rho_2 \left(\frac{S}{V}\right)_{plane} = \frac{1}{T_{2B}} + \rho_2 \left(\frac{2}{w}\right)_{plane}, \tag{3-11}$$

where T_{2B} is 3.1 seconds, ρ_2 is chosen as 10 μm/sec, and the aperture of planar fractures, w, is 9 μm. The resulting theoretical T_2 value for the fractures will then be 393 msec. However, our pore-scale simulations, which assume voxelized grain boundary, shows a fracture T_2 peak at 274 msec (Fig. 3.1a and Table 3.1). This difference between the theoretical and simulated T_2 values comes from the discretization of the pore space in the micro-CT images, which overestimates the grain-fluid interface surface area by about

1.5 times (Jin et al. 2009). To theoretically validate the simulation result, Equation (3-11) should be modified for a "surface-area-corrected" coefficient of 1.5, as given by

$$\frac{1}{T_2} = \frac{1}{T_{2B}} + \rho_2 \cdot 1.5(\frac{S}{V})_{plane} = \frac{1}{T_{2B}} + \rho_2 \cdot (\frac{3}{w})_{plane}, \tag{3-12}$$

which provides T_2 peak location of 274 msec.

Similarly, the T_2 values for channel-like inclusions can be theoretically estimated via

$$\frac{1}{T_2} = \frac{1}{T_{2B}} + \rho_2 \cdot (\frac{S}{V})_{cylinder} = \frac{1}{T_{2B}} + \rho_2 \cdot (\frac{4}{d})_{cylinder}, \tag{3-13}$$

where d is the diameter of the cylindrical channels. Then we applied a "surface-area-corrected" coefficient of 1.5 on the right-hand-side to correct for the discretization effect. Then the Equation (3-13) becomes

$$\frac{1}{T_2} = \frac{1}{T_{2B}} + \rho_2 \cdot 1.5(\frac{S}{V})_{cylinder} = \frac{1}{T_{2B}} + \rho_2 \cdot (\frac{6}{d})_{cylinder}. \tag{3-14}$$

This surface-area correction method was applied to theoretically estimate the NMR relaxation times for all the isolated fractures, including planar fractures and channel-like inclusions, in Section 2.

3.8. Summary of Results

We quantified the impact of micro-fractures and the effect of fracture-pore diffusional coupling on NMR responses in multiple-pore-type systems. To summarize,

two forms of pore structures, the inter-granular pores and the micro-fractures (including planar fractures and channel-like inclusions), were simultaneously considered in my simulation cases. The results of simulations showed that the effect of diffusional coupling on NMR response is significant. When the two forms of porous structures are diffusionally coupled, (a) the longer T_2 component always significantly decreases; (b) the shorter T_2 component remains unaffected or slightly decreased; and (c) the volume occupied by the shorter T_2 component can be underestimated by NMR T_2 distribution.

We evaluated rock samples with different combinations of pore and fracture sizes. The fracture-pore diffusional coupling effect can be summarized in three categories as follows:

(a) Planar fractures much thinner than 1/3 of pore size: the pore relaxation times are significantly shortened by the existence of fractures. Thin fractures shift the pore relaxation time more significantly than thick fractures do.

(b) Planar fractures much thicker than 1/3 of pore size: the inter-granular pores cause a significant decrease in fracture relaxation times. The well-connected pores can shorten the fracture relaxation time more significantly than the poorly-connected pores do. Furthermore, the total volume of inter-granular pores can be underestimated in this case.

(c) Planar fracture apertures close to 1/3 of pore size: the relaxation times corresponding to micro-fractures overlap those of inter-granular pores. Thus, fractures and pores cannot be distinguished using NMR T_2 distribution in this case.

In all the three aforementioned categories, NMR T_2 distribution is shown to be sensitive to volumetric concentration and shape of micro-fractures. With higher concentration of fractures, the fracture-pore coupling becomes stronger. Furthermore, planar fractures show more significant impact on T_2 distribution than channel-like inclusions even when they have the same S/V ratio.

3.9. Conclusions

Based on the simulation results and analytical model calculations obtained in this research, and previously published experimental outcomes, we proposed a new concept of fracture-pore coupling, and showed that NMR T_2 distribution is influenced by the diffusional coupling between micro-fractures (or channel-like inclusions) and inter-granular pores. The intergranular pore size can be underestimated by up to 29%, and the volume fraction of intergranular pores can be underestimated by more than 10%, if the impact of fracture-pore diffusional coupling was not taken into account in interpretation of NMR relaxometry.

Recognition of the fracture-pore diffusional coupling effect can improve substantially the interpretation of NMR measurements in a variety of rock samples (e.g., naturally fractured carbonates and organic-rich mudrocks). It is generally accepted that NMR T_2 distribution represents the pore size distribution in rock samples; however, we demonstrated that the pore size or the pore volume fraction can be significantly underestimated by NMR measurements due to fracture-pore coupling.

The findings of this study are promising to improve the interpretation of NMR core and borehole measurements in reservoirs with complex pore structure. They also enable future applications of NMR measurements to the assessment of volumetric concentration of micro-fractures, in addition to inter-/intra-granular pores, when combined with other conventional well logs.

4. ASSESSMENT OF MICRO-FRACTURES USING THE NMR ANALYTICAL MODEL FOR FRACTURE-PORE DIFFUSIONAL COUPLING

Assessment of micro-fracture volumetric concentration and aperture in hydrocarbon-bearing reservoirs raises special interest for designing production plans and selecting zones for fracture treatment. NMR T_2 distribution has been traditionally considered insensitive to the presence of fractures. However, the previous section demonstrated a measureable NMR sensitivity to the existence of micro-fractures and proposed a new concept of fracture-pore diffusional coupling. The quantification of micro-fracture volumetric concentrations and apertures in fractured formations remains a challenging issue, and distinguishing fractures from pore space is not possible from NMR T_2 measurement alone. However, if additional borehole measurements, such as micro-imaging or induction logs, are included and combined with NMR measurements, the evaluation of micro-fracture volumetric concentration and aperture becomes possible. This section explores the possibility of evaluating the porosity associated with micro-fractures and intra-/inter-granular pores and the micro-fracture aperture in complex formations, using the analytical model for NMR fracture-pore diffusional coupling with aid of other well logging measurements.

This technique applied successfully to synthetic cases devised from pore-scale images of carbonate and organic-rich mudrock formations. The estimated micro-fracture volumetric concentration and apertures showed agreement with the actual

value. The results further showed that assessment of fracture volumetric concentration is possible by combining the NMR analytical model of fracture-pore diffusional coupling and other well logging methods such as induction logs. This introduced method for quantifying micro-fracture volumetric concentration and aperture can improve reservoir characterization, contribute to operational decisions regarding number and location of fracture treatments, and enhance production from tight carbonate and organic-rich mudrock formations.

4.1. Method Introduction

Section 3 defined micro-fractures that are diffusionally coupled (i.e., connected) with inter-granular pores as "coupled fractures," and those not connected to inter-granular pores as "isolated fractures." The previous section further used the fracture-pore diffusional coupling analytical model to do forward modeling based on knowledge of micro-fracture dimensions, to predict the T_2 modes of coupled fractures in the measured (or simulated) NMR T_2 distribution of the rock sample. This section explains the use of the fracture-pore diffusional coupling analytical model to do inverse modeling based on the T_2 modes of coupled fractures and pores in the measured (or simulated) NMR T_2 distribution, to estimate the volumetric concentrations and aperture of micro-fractures.

As shown in the previous section, the relaxation time associated to the coupled fractures, $T_{2F,coupled}$, expresses as

$$\frac{1}{T_{2F,coupled}} = \frac{2}{w}\left[\sqrt{\frac{\phi_{pore} D}{T_{2p} F}} + \rho(1-\phi_{pore})\right], \tag{4-1}$$

where w is the aperture of planar fractures, D is the diffusion coefficient of saturating fluids (brine water) within the rock, ρ is the surface relaxivity of the rock grains, T_{2p} is the relaxation time associated to inter-granular pores, and F and ϕ_{pore} are the formation factor and the inter-granular porosity in the inter-granular pore domain, respectively.

In the fracture-pore diffusional coupling model, the amplitude of T_2 modes is proportional to the volume fraction of corresponding pore structures. The T_2 mode amplitude of isolated micro-fractures, $\phi_{F,iso}$, shows the real volume fraction taken up by the micro-fractures. The T_2 mode amplitude of coupled micro-fractures, $\phi_{F,coupled}$, shows the apparent volume fraction measured by NMR, which has been overestimated from the real value due to fracture-pore diffusional coupling. According to the relationship between $\phi_{F,coupled}$ and $\phi_{F,iso}$ (Ramakrishnan et al. 1999), the following expression estimates the real volume fraction of micro-fracture, $\phi_{F,iso}$, i.e. the micro-fracture density, by

$$\phi_{F,iso} \cong \phi_{F,coupled} \frac{(1+X/2)}{(1+X)^2}, \tag{4-2}$$

where

$$X \cong \frac{T_{2p}/T_{2F,coupled}}{\sqrt{1-T_{2p}/T_{2F,coupled}}},$$

in which $\phi_{F,coupled}$, T_{2p}, and $T_{2F,coupled}$ were read off from the measured (or simulated) NMR T_2 distributions.

Consequently, the real porosity of pore space, ϕ_{pore}, can be estimated by

$$\phi_{pore} = \phi_{tot} - \phi_{F,iso}, \tag{4-3}$$

where ϕ_{tot} is the total porosity of rock, which can be measured by NMR. Thereafter, one can estimate the aperture of planar fractures, w, based on Equation (4-1), given by

$$w = 2T_{2F,coupled}[\sqrt{\frac{\phi_{pore}D}{T_{2p}F}} + \rho(1-\phi_{pore})], \tag{4-4}$$

as long as one knows the values of the parameters ρ, D and F. The water diffusion coefficient, D, is assumed as 2.07×10^{-9} m^2/s in this section. The surface relaxivity, ρ, is assumed as 10μm/sec and 15 μm/sec for carbonate and organic-rich mudrock cases, respectively. The electrical formation factor, F, can be expressed as $1/\phi_{pore}^{m}$ according to Archie's law. Then the parameter, m, can be assumed as 2.2 to 2.8 for carbonate cases, and 1.7 for organic-rich mudrock cases, respectively, and estimated as the fracture aperture. This work emphasizes that the fracture aperture estimation is highly sensitive to the value of electrical formation factor, thus sensitive to the parameter m.

4.2. Synthetic Case No. 1: Carbonate Formation

4.2.1. Carbonate Formation with Different Concentrations of Micro-Fractures

Synthetic Example No. 1 is designed to investigate the reliability of the proposed micro-fracture estimation method in fractured carbonate formations. This

research involved designing five synthetic carbonate cases with different volumetric concentrations of micro-fractures. **Fig. 4.1** shows the comparison of these artificially fractured carbonate rock matrices. Cases A, B, and C contain 2, 4, and 6 vertical primary fractures, respectively; Cases D and E contain 2 and 4 primary fractures, respectively, and secondary fractures terminating at the primary fractures. The micro-fractures are square and planar in shape, with an aperture of 9 μm and a length of 450 μm.

Figs. 4.2 and **4.3** show the simulated NMR T_2 distribution and the corresponding analytical T_2 modes for these artificially fractured carbonate rock samples. The T_2 peaks at 241.9 msec are attributable to the existence of planar fractures, which can be verified by NMR numerical simulations for the isolated fractures and the original carbonate sample. The next step calculated the real micro-fracture volume concentration using Equation (4-2), and further estimated the fracture aperture using Equation (4-4). **Table 4.1** lists the pore and fracture T_2 modes read off from T_2 distributions, the estimated/real fracture volumetric concentration and relative error, the estimated inter-granular porosity, and the estimated/real fracture aperture and relative error for all five rock samples. It shows that the NMR estimation of fracture volumetric concentration using the NMR analytical model is accurate within 6.63% of error for Cases A, B, and C, which contain only primary fractures; and the estimation is accurate within 11.67% of error for Cases D and E, which contain both primary and secondary fractures. In addition, the NMR estimation of fracture aperture is accurate within 7.52% of error for

all five cases. These errors are mainly because the NMR 1D analytical model is an oversimplification of the 3D cases.

Table 4.1—Carbonate rock samples with different concentrations of micro-fractures: NMR T_2 values for coupled pores and fractures, estimated and real fracture density and its relative error, estimated inter-granular porosity, estimated and real fracture aperture and its relative error, for synthetic example No. 1.

Variable	Case A	Case B	Case C	Case D	Case E
Carbonate Pore T_2, msec	103.5	103.5	103.5	103.5	103.5
Coupled Fracture T_2, msec	241.9	241.9	241.9	241.9	241.9
NMR Estimated Fracture Volumetric Concentration, %	4.41	8.31	11.28	5.24	10.03
Real Fracture Volumetric Concentration, %	4.73	8.20	12.00	5.90	11.35
NMR Relative Error in Fracture Volumetric Concentration, %	-6.63	1.30	-5.97	-11.22	-11.67
NMR Estimated Inter-granular Porosity, %	16.01	15.59	16.42	16.36	17.02
NMR Estimated Fracture Aperture, μm	9.41	9.45	9.51	9.50	9.68
Real Fracture Aperture, μm	9.00	9.00	9.00	9.00	9.00
Relative Error in Fracture Aperture, %	4.57	5.05	5.72	5.56	7.52

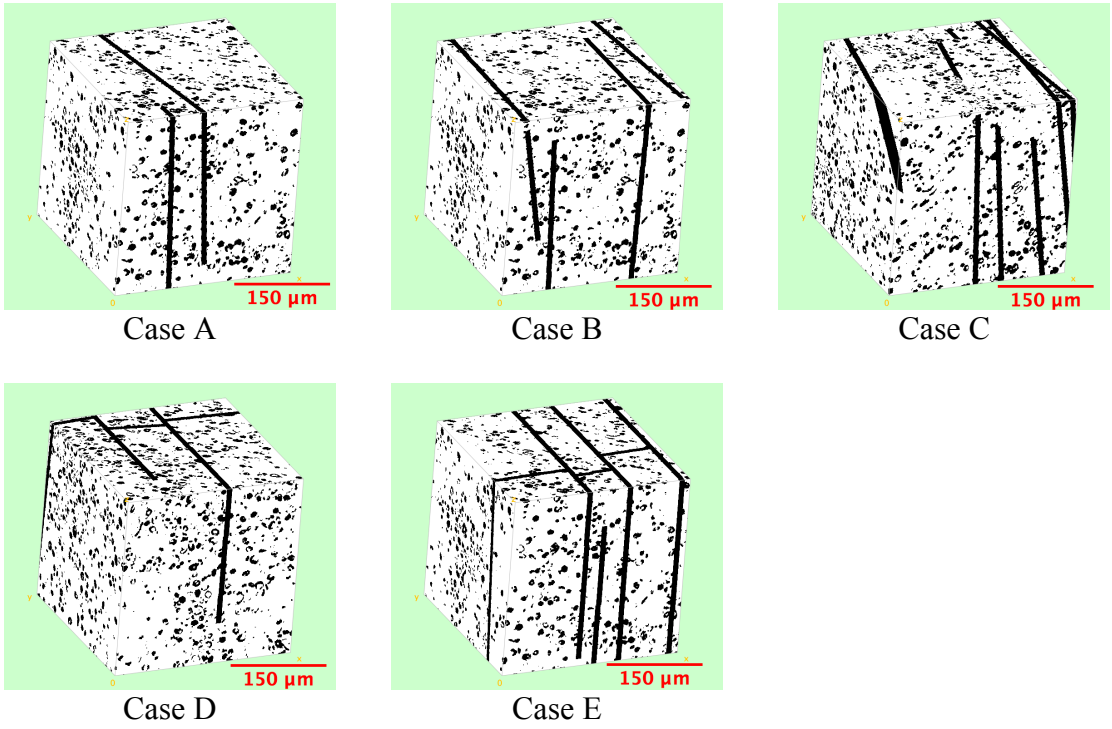

Fig. 4.1—Carbonate rock samples with different concentrations of fractures: Pore-scale images of five fractured carbonate rock samples. Case A, B, and C contain 2, 4, and 6 primary fractures, respectively. Case D and E contain 2 and 4 primary fractures, and secondary fractures terminating at primary fractures. The planar fractures are 9 µm in aperture, and 450 µm in length for all cases. The white and black regions represent the rock grains and pore space, respectively.

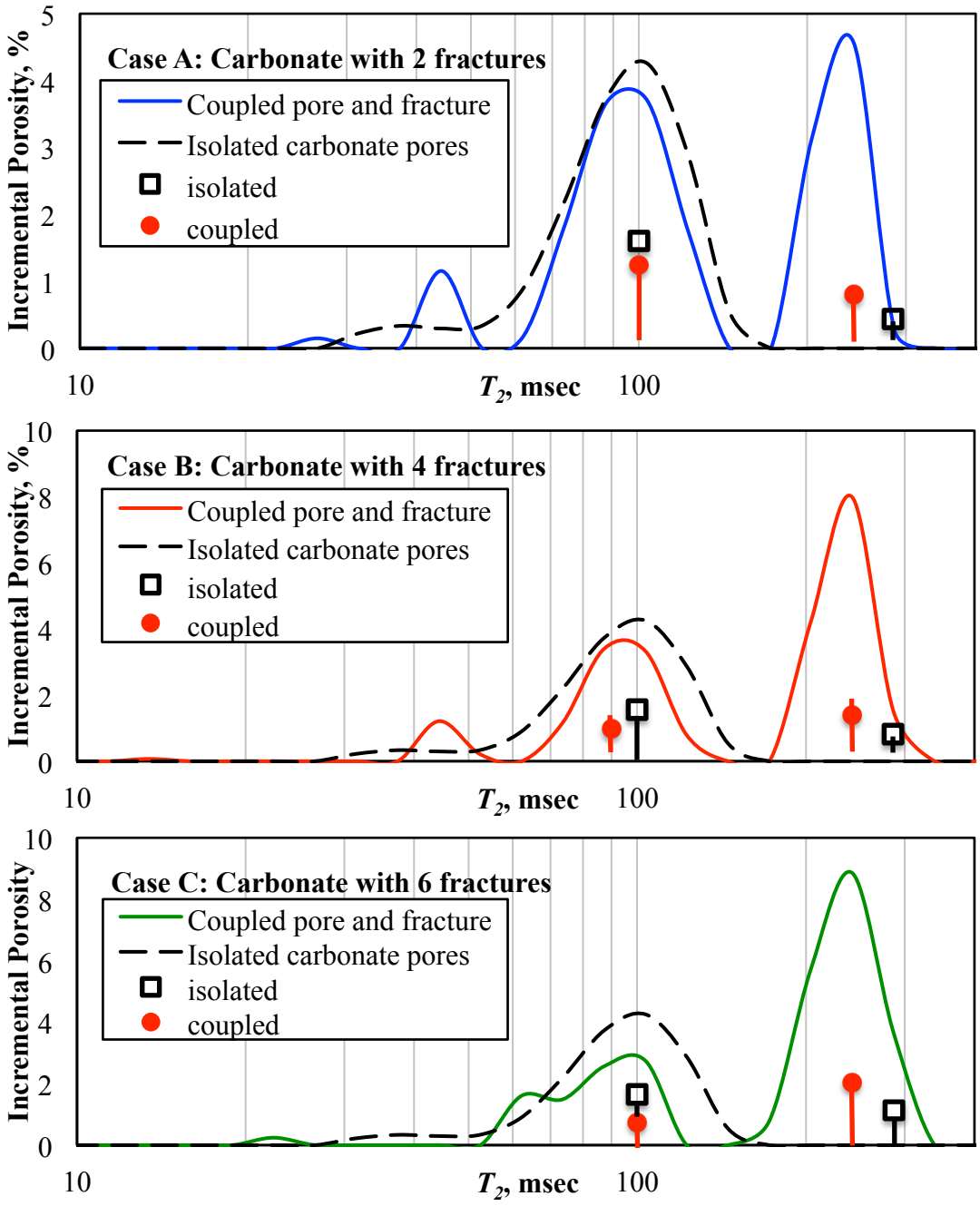

Fig. 4.2—Carbonate rock samples with different concentrations of fractures, Cases A - C: Analytical T_2 modes and simulated T_2 distributions for the carbonate rock samples including primary fractures. The black bars represent the analytical T_2 modes for isolated carbonate pores or fractures, and the red bars show coupled fractures or pores. The blue, red, and green lines show NMR T_2 distributions of carbonate rock samples with 2, 4, and 6 primary fractures, respectively. The area under each T_2 distribution curve represents the total porosity of the rock sample.

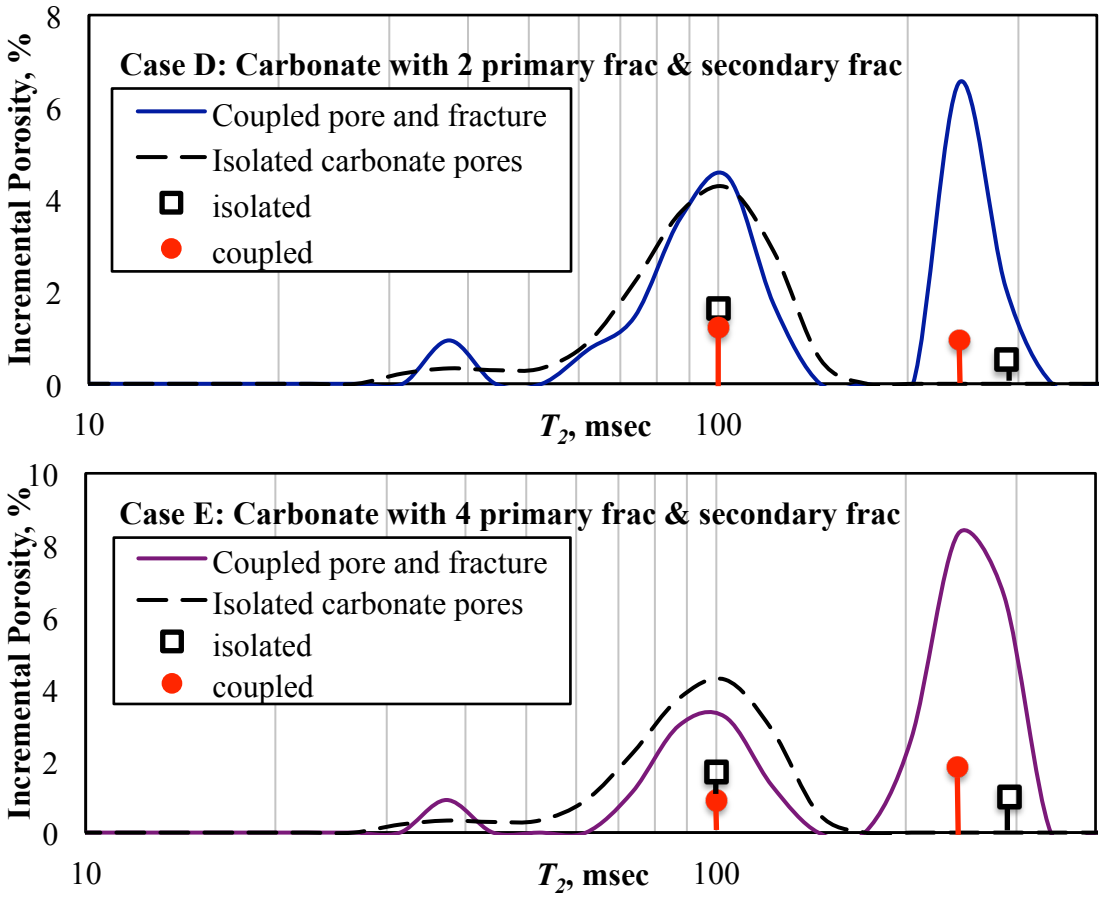

Fig. 4.3—Carbonate rock samples with different concentrations of fractures, Cases D and E: Analytical T_2 modes and simulated T_2 distributions for the carbonate rock samples including primary and secondary fractures. The black bars represent the analytical T_2 modes for isolated carbonate pores and fractures, and the red bars show coupled fractures and pores. The dark blue and brown lines show NMR T_2 distributions of carbonate rock samples with 2 and 4 primary fractures, respectively. The area under each T_2 distribution curve represents the total porosity of the rock sample.

Table 4.2—Carbonate rock samples with different apertures of micro-fractures: NMR T_2 values for coupled pores and fractures, estimated and real fracture density and its relative error, estimated inter-granular porosity, estimated and real fracture aperture and its relative error, for synthetic example No. 1.

Variable	Case A	Case B	Case C
Carbonate Pore T_2, msec	103.5	103.5	103.5
Coupled Fracture T_2, msec	204.1	241.9	286.6
NMR Estimated Fracture Volumetric Concentration, %	1.52	2.03	2.56
Real Fracture Volumetric Concentration, %	1.74	2.32	2.90
NMR Relative Error in Fracture Volumetric Concentration, %	-12.74	-12.40	-11.63
NMR Estimated Inter-granular Porosity, %	15.92	15.99	16.04
NMR Estimated Fracture Aperture, μm	9.52	11.45	13.81
Real Fracture Aperture, μm	9.00	12.00	15.00
Relative Error in Fracture Aperture, %	5.73	-4.57	-7.92

4.2.2. Carbonate Formation with Different Micro-Fracture Apertures

The three synthetic carbonate cases in this example contain planar fractures of different apertures. The square planar fractures are 270 μm in length, and two fractures are included in each rock matrix. The fracture apertures for Case A, B, and C are 9 μm, 12 μm, and 15 μm, respectively. **Fig. 4.4** shows the comparison of these three artificially fractured carbonate cases. **Fig. 4.5** shows the analytical T_2 modes and the simulated NMR T_2 distribution for these fractured carbonate rock samples. We attributed the T_2 peaks at 215, 242, and 305 msec to the existence of planar fractures. Then we calculated the real micro-fracture volumetric concentration using Equation (4-2), and further estimated the fracture aperture using Equation (4-4). **Table 4.2** lists the pore and fracture T_2 modes read off from T_2 distributions, the estimated/real micro-fracture density and relative error, the estimated inter-granular porosity, and the estimated/real micro-fracture aperture and relative error for all three cases. The data shows that the NMR estimation of micro-fracture volumetric concentration is accurate within 12.74% of error, and the NMR estimation of fracture apertures is within 7.92% of error for all three cases.

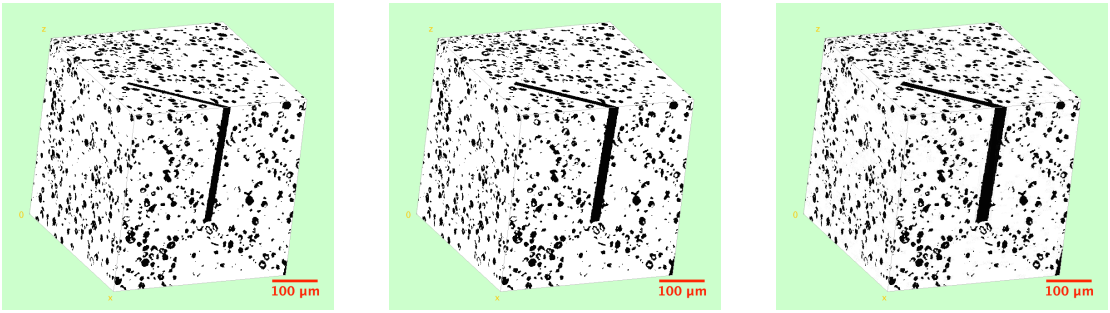

Case A Case B Case C

Fig. 4.4—Carbonate rock samples with different apertures of fractures: Pore-scale images of three cases of fractured carbonate rock samples. The fracture apertures for Case A, B, and C are 9 µm, 12 µm, and 15 µm, respectively. The planar fractures are 270 µm in length, and the number of fractures is 2 for all cases. The white and black regions represent the rock grains and pore space, respectively.

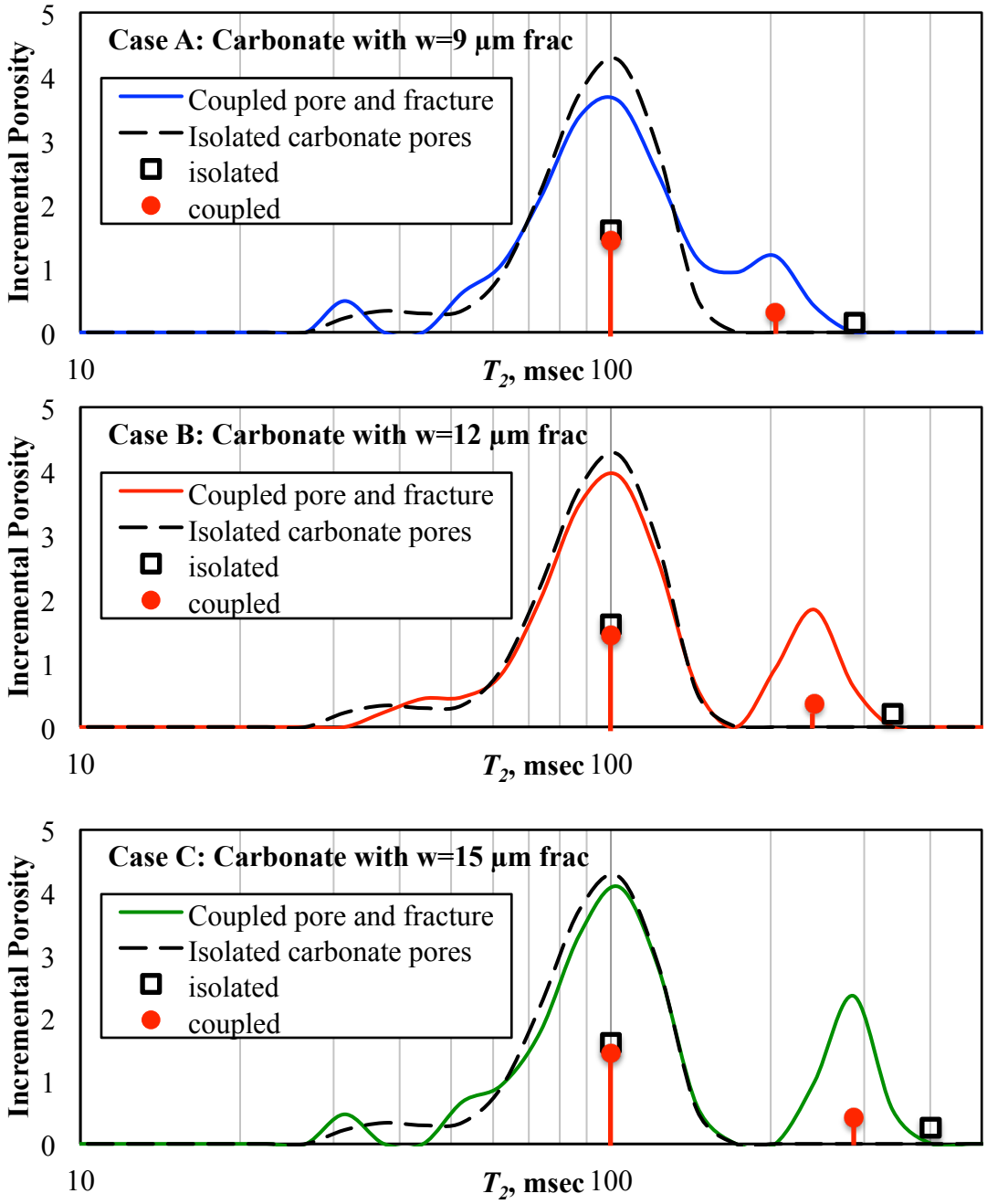

Fig. 4.5—Carbonate rock samples with different apertures of fractures: Analytical T_2 modes and simulated T_2 distributions for the carbonate rock samples including planar fractures with aperture (w) of 9 µm, 12 µm, or 15 µm, respectively. The black bars represent the analytical T_2 modes for isolated carbonate pores or fractures, and the red bars show coupled fractures or pores. The blue, red, and green lines show NMR T_2 distributions of carbonate rock sample with w = 9, 12, and 15 µm micro-fractures, respectively. The area under each T_2 distribution curve represents the total porosity of the rock sample.

4.3. Synthetic Case No. 2: Organic-rich Mudrock Formation

The purpose of this synthetic case is to test the reliability of the introduced micro-fracture estimation method in fractured organic-rich mudrock formations. The three synthetic organic-rich mudrock cases in this example contain planar fractures of different apertures. The square planar fractures are 135 μm in length, and two fractures are included in each case. The fracture apertures for Cases A, B, and C are 1.5 μm, 4.5 μm, and 7.5 μm, respectively. **Fig. 4.6** shows the comparison of these three artificially fractured carbonate cases. **Fig. 4.7** shows the analytical T_2 modes and the simulated NMR T_2 distribution for these fractured organic-rich mudrock samples. We attributed the T_2 peaks at 17.5, 53, and 82 msec to the planar fractures. The next step calculated the real micro-fracture volumetric concentration using Equation (4-2), and further estimated the fracture aperture using Equation (4-4). **Table 4.3** lists the pore and fracture T_2 modes read off from T_2 distributions, the estimated/real micro-fracture density and relative error, the estimated inter-granular porosity, and the estimated/real micro-fracture aperture and relative error for all three cases. It shows that the NMR estimation of micro-fracture volumetric concentration is accurate within 16.4% of error, and the NMR estimation of fracture apertures is within 4.27% of error for all three cases.

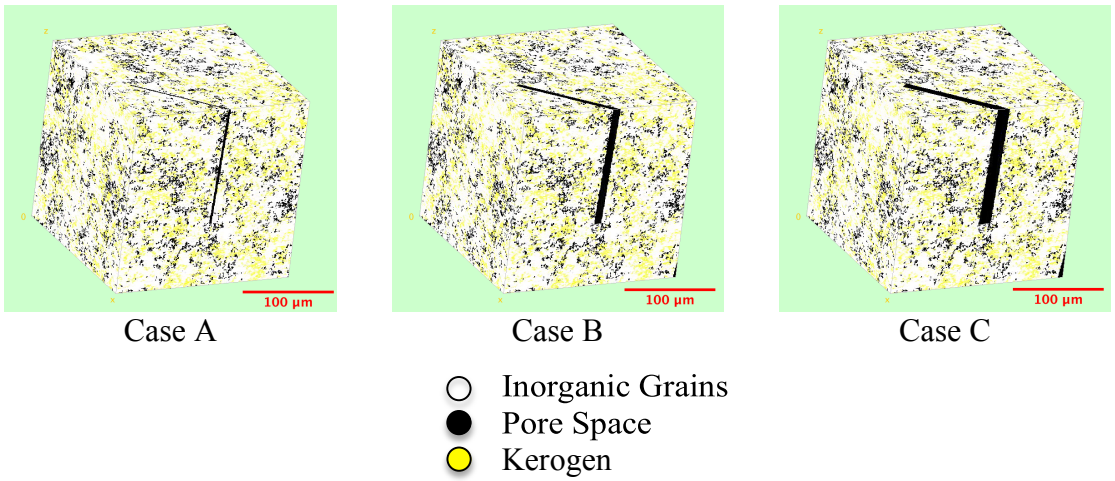

Fig. 4.6—Synthetic organic-rich mudrock samples: Pore-scale images of three cases of fractured organic-rich mudrock samples. The fracture apertures for Case A, B, and C are 1.5 µm, 4.5 µm, and 7.5 µm, respectively. The square planar fractures are 135 µm in length, and the number of fractures is 2 for all cases. The yellow, white, and black regions represent the kerogen, rock matrix, and pore space, respectively.

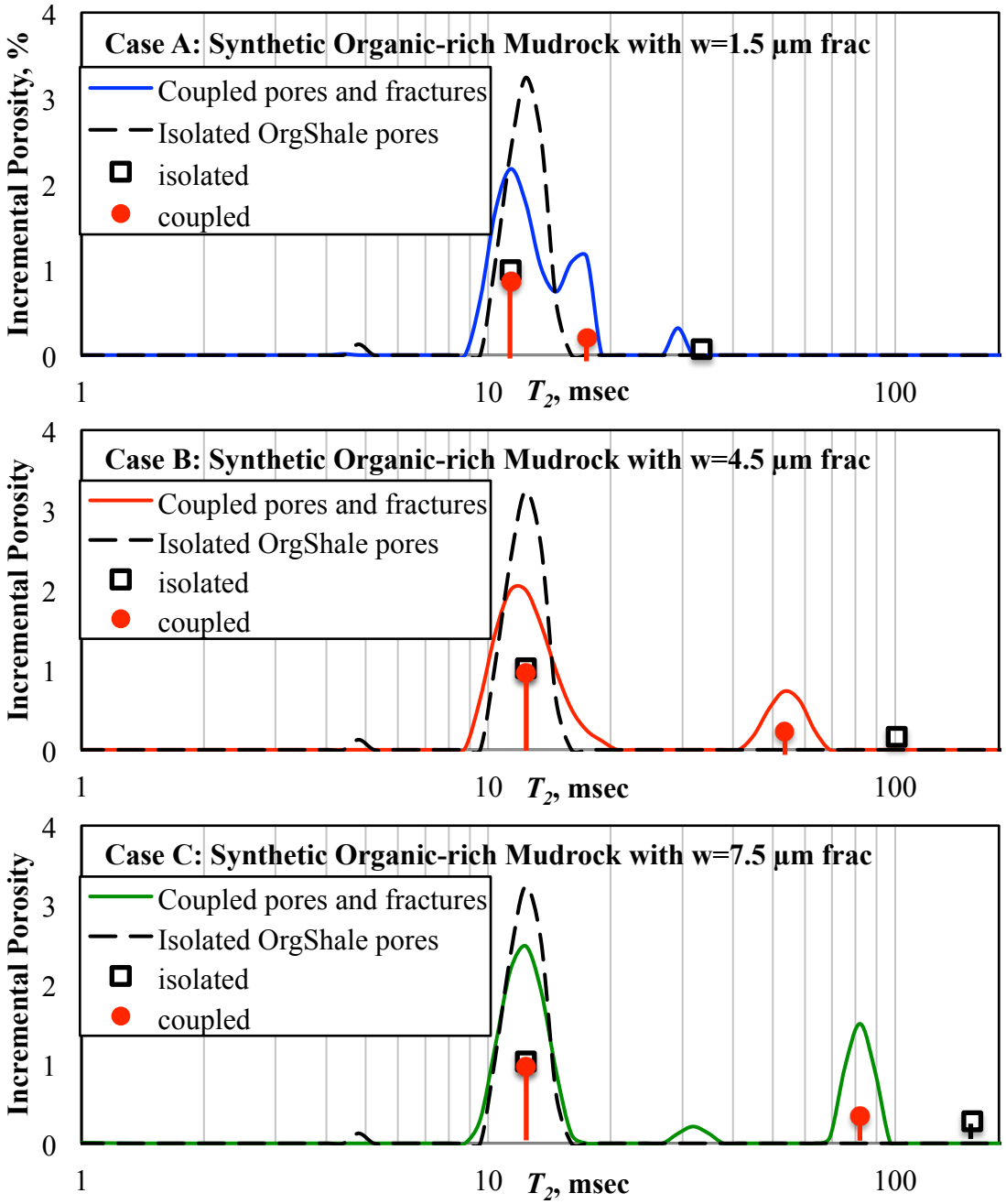

Fig. 4.7—Synthetic organic-rich mudrock samples: Analytical T_2 modes and simulated T_2 distributions for the synthetic organic-rich mudrock samples including planar micro-fractures with aperture (w) of 1.5 µm, 4.5 µm, or 7.5 µm, respectively. The black bars represent the analytical T_2 modes for isolated mudrock pores or fractures, and the red bars show coupled fractures and pores. The blue, red, and green lines show NMR T_2 distributions of carbonate rock sample with w = 1.5, 4.5, and 7.5 µm micro-fractures, respectively. The area under each T_2 distribution curve represents the total porosity of the rock sample.

Table 4.3—Synthetic organic-rich mudrock samples: NMR T_2 values for coupled pores and fractures, estimated and real fracture volumetric concentration and its relative error, estimated inter-granular porosity, estimated and real fracture aperture and its relative error, for synthetic example No. 2.

Variable	Case A	Case B	Case C
Organic-rich Mudrock Pore T_2, msec	11.35	12.37	12.37
Coupled Fracture T_2, msec	17.5	53.4	82.1
NMR Estimated Fracture Volumetric Concentration, %	7.10	16.28	27.55
Real Fracture Volumetric Concentration, %	6.10	18.40	30.70
NMR Relative Error in Fracture Volumetric Concentration, %	16.40	-11.55	-10.26
NMR Estimated Inter-granular Porosity, %	9.90	10.21	10.31
NMR Estimated Fracture Aperture, μm	1.52	4.69	7.33
Real Fracture Aperture, μm	1.5	4.5	7.5
Relative Error in Fracture Aperture, %	1.56	4.27	-2.24

4.4. Conclusion

Characterization of micro-fracture volumetric concentration and apertures in fractured formations remains a challenging task that directly impacts completion designs, including placement and number of fracture treatments. However, estimation of micro-fracture volumetric concentration and apertures has not been investigated by NMR measurements or conventional well logging methods. The present work has demonstrated that the volumetric concentrations of micro-fractures and pores, as well as micro-fracture aperture, can be estimated by using an NMR analytical model for fracture-pore diffusional coupling, with aid of other well logging methods.

The NMR numerical simulations and analytical solutions show that the estimated volumetric concentrations of micro-fractures are within 12.74% error for all carbonate cases, and within 16.40% error for all synthetic organic-rich mudrock cases, compared to the actual values. Furthermore, the estimated fracture apertures are within 7.92% error for all carbonate cases, and within 4.27% error for the synthetic organic-rich mudrock cases. The outcomes of this research can be applied to increase production from tight carbonate and organic-rich mudrock formations by improving the fracturing treatment designs through enhanced reservoir characterization.

5. DIRECTIONAL PERMEABILITY ASSESSMENT USING NMR RELAXOMETRY

In this section we propose a new method for directional permeability assessment using NMR measurements. Conventional techniques for permeability assessment from NMR measurements include empirical correlations such as SDR (Schlumberger-Doll-Research) and Coates models. However, carbonate rocks are known for lack of good correlations between pore-body-size and pore-throat-size, which makes it challenging and often unreliable to estimate permeability from NMR T_2 distribution in carbonate formations with complex pore structure. It has also been proposed that conventional permeability models can be improved by incorporating an estimated pore connectivity factor. However, none of the previously introduced techniques reflect the anisotropic characteristics of rock permeability. Here, we introduce a new NMR-based directional permeability model by incorporating a directional pore-connectivity factor into a conventional NMR-based permeability model.

We developed two approaches to quantify the directional pore network connectivity of rock samples using pore-scale images. The first approach calculates directional pore connectivity in 3D pore-scale images using a topological technique. The second approach combines image analysis and electrical formation factor. The new NMR-based permeability model enables assessment of rock permeability in any desired direction.

We successfully calibrated and tested the introduced NMR-based permeability model on carbonate, sandstone, and sandpack samples with complex pore geometry or anisotropic permeability. Then we compared the directional permeability estimated from the new NMR model against the directional permeability calculated from Lattice Boltzmann Method (LBM) simulations. The comparison between the permeability estimates using our new NMR model and conventional NMR models (e.g. SDR and Coates models) demonstrated that the NMR-based directional permeability model significantly improves assessment of rock permeability, by reflecting rock's anisotropic characteristics and minimizing calibration efforts. The outcomes of this research can significantly improve permeability assessment in complex carbonate reservoirs and anisotropic sandstone reservoirs, and can be further extended to organic-rich mudrock formations.

5.1. Literature Review

Permeability assessment has been one of the most challenging tasks in formation evaluation, especially in carbonate reservoirs with complex pore structures. NMR measurements have been considered as good candidates for assessment of rock permeability, because of their sensitivity to pore size distribution in rocks. Conventionally the NMR T_2 distribution is considered as representing pore size distribution, therefore the conventional NMR-based permeability models take advantage of this specific characteristic to estimate rock permeability. The most

extensively-used conventional NMR-based permeability models include the SDR (Schlumberger-Doll-Research) model (Kenyon et al. 1988) and the Coates model (Coates et al. 1997), as shown in Equations (5-1) and (5-2):

$$k_{SDR} = C\phi^a T_{2GM}^b, \tag{5-1}$$

and

$$k_{Coates} = (\frac{\phi}{C})^m (\frac{BVM}{BVI})^n, \tag{5-2}$$

where k is the permeability in mD, ϕ is the porosity in percent. For SDR model, T_{2GM} is the geometric mean of NMR T_2 distribution in sec, a and b are constant parameters with typical values of 4 and 2, respectively, and the parameter C is a constant that depends on the formation type. For Coates model, C, m, and n are constants with typical values of 10, 4, and 2, respectively. BVM and BVI stand for bulk volume movable and bulk volume irreducible, respectively. BVI is obtained by integrating all partial porosity up to a selected cutoff value $T_{2cutoff}$, and BVM is calculated by total porosity minus BVI. The commonly-used value for $T_{2cutoff}$ is 90 msec for carbonates, but in many real cases this T_2 cutoff value requires adjustment for each rock type and can vary significantly, e.g. from 18.3 msec to 1072 msec (Chen et al. 2008).

Both SDR and Coates models can provide reliable estimates of permeability when the pore network is well connected, such as in the case of sandstone formations. However, carbonate rocks are known for lack of good correlations between pore-body-size and pore-throat-size, which makes the reliability of conventional NMR-based

permeability models questionable. To enhance performance of conventional NMR-based permeability models in carbonate formations, previous publications proposed new NMR models by modifying the conventional ones. The first example is the modified SDR model for vuggy carbonates (Chang et al. 1997), which was derived based on experimental data and is given by

$$k_{SDR\_Modified} = C\phi^4_{<750ms} T^2_{2GM,<750ms}, \tag{5-3}$$

where $<750ms$ means with T_2 less than 750 msec. This model assumes an empirical $T_{2\text{cutoff}}$ value for large vugs in carbonates. Indeed, all pore structures with T_2 relaxation times larger than 750 msec are considered as isolated vugs. Consequently, the large vugs are excluded from the calculation of T_{2GM} and effective porosity, and the permeability is estimated only from the porosities with T_2 shorter than 750 msec. This model assumes that all large vugs are disconnected and do not contribute to the rock permeability, which may not be a realistic assumption in many carbonate cases.

Another modified NMR-based permeability model for carbonate formations is the connectivity-based permeability model, which was adapted from the Coates model (Chen et al. 2008). The authors incorporated a pore-connectivity factor into the Coates model. They expressed the permeability via

$$k_{Coates\_p} = \left(\frac{\phi}{C}\right)^m \cdot \left(\frac{p \cdot BVM}{BVI + (1-p)\cdot BVM}\right)^n, \tag{5-4}$$

where p is the pore-connectivity factor estimated from thin-section photomicrographs of carbonate samples, ranging from 0 to 1. The connectivity factor p represents the

volumetric fraction of connected pores in *BVM*, while 1-*p* represents the isolated pore fraction in *BVM*. Consequently, the isolated pores are excluded from calculation of *BVM* and are counted as addition to irreducible fluid volume *BVI*. By this means, the *BVI* and *BVM* can be calculated using the typical $T_{2cutoff}$ value, 90 msec, for carbonates, which eliminates the need to adjust $T_{2cutoff}$ for different rock types. This modified Coates model (Chen et al. 2008), however, requires empirical assessment of pore-connectivity factor based on two-dimensional (2D) thin-section images of rock samples, therefore it cannot be calculated objectively.

In all the previously published NMR-based permeability models, the estimated permeability does not reflect the anisotropic characteristics of rock permeability. We hereby introduced a new NMR-based directional permeability model by incorporating a directional pore-connectivity factor to estimate the anisotropic permeability of carbonate and sandstone rocks (Chi and Heidari 2015b; Chi and Heidari 2014c). The directional pore connectivity factor can be calculated from 3D pore-scale images, or from electrical formation factor. The quantification of pore-connectivity from 3D pore-scale images is based on the method introduced by Vogel (1997), utilizing the topological concept of Euler-Poincare Characteristics (EPC).

5.2. Quantification of Directional Pore-Connectivity Factor

There have been several studies attempting to quantify the pore connectivity in porous structures. Previously, many researchers quantified the pore connectivity from

the viewpoint of percolation theory, for example, Gueguen and Dienes (1989) defined the connectivity as the ratio of the number of pores belonging to the percolating cluster to the total number of pores. Other researchers studying common porous rocks, argued that the mean coordination number, i.e. the number of pores connected to a given node of the topological skeleton, is a more appropriate parameter to quantify pore connectivity (Bernabe et al. 2010). Also, there have been studies utilized a topological concept, Euler-Poincare Characteristics (EPC), to characterize pore connectivity (Odgaard and Gundersen 1993; Gundersen et al. 1993; Vogel 1997). In this section we focus on the EPC approach to quantify the pore connectivity in rock samples, due to its simplicity and convenience to apply on voxelized micro-CT images.

5.2.1. Introduction to Euler-Poincare Characteristics (EPC)

The topological concept, EPC, has been used to characterize the connectivity of porous structures such as cancellous bone (Odgaard and Gundersen 1993) and soil samples (Vogel 1997). The EPC of a network structure in 3D space, e_{3D}, is defined as (Gundersen et al. 1993):

$$e_{3D} = N - C + H, \tag{5-5}$$

where N is the number of isolated components of the structure; C is the number of redundant connections or "handles", which can be interpreted as the number of holes in the structure; and H is the number of enclosed cavities within the 3D structure. In 2D space, EPC is defined simply as $e_{2D} = N - C$. For example, the 2D EPC of the three images in **Fig. 5.1** is 2, 2, and 1, respectively.

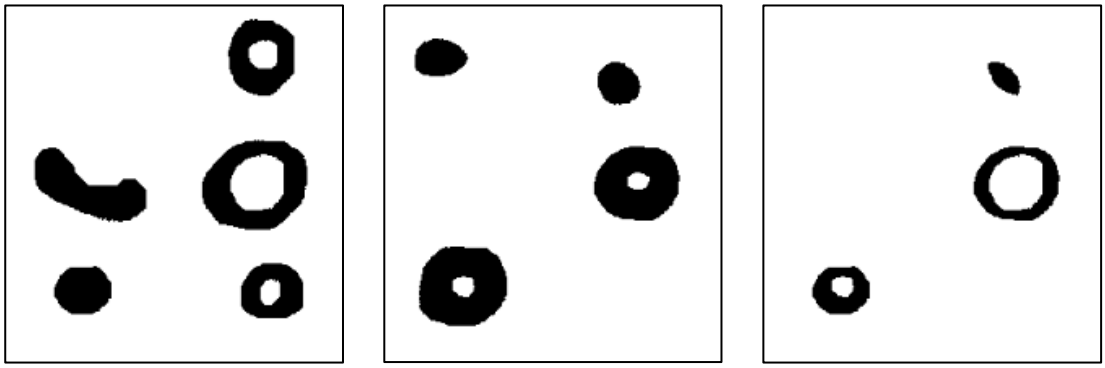

Fig. 5.1—Two adjacent 2D images, S_{i-1} (left) and S_i (middle), and their overlapping surface, $S_{i-1} \cap S_i$ (right).

When calculating the connectivity of pores in a 3D rock sample, *N* reports the number of isolated pore structure, *C* reports the number of tunnels, and *H* is the number of "suspending grains" in pores, which should be zero in reality. By topological definition, smaller EPC value corresponds to higher connectivity. Negative EPC values usually indicate well-connected pores, and positive values indicate poorly-connected pores.

We used Vogel's method (Vogel 1997) to calculate the 3D EPC of pore structures in rock samples. First, we have a series of micro-CT images along one direction (**Fig. 5.2**). Next, we compute the 2D EPC, $e_{2,i}$, for each micro-CT image, S_i. The 3D EPC, $e_{3,i}$, for each pair of adjacent images, S_{i-1} and S_i, is given by

$$e_{3,i} = \frac{e_{2,i-1} + e_{2,i} + e_{2,i-1\cap i}}{2}, \tag{5-6}$$

where i-1$\cap i$ means the logical AND operation for the i-th pair of adjacent images, and $e_{2,i\text{-}1\cap i}$ is the 2D EPC of the overlapping area of the i-th and (i-1)-th images. Fig. 5.2 shows an example where $e_{2,i\text{-}1}$, $e_{2,i}$, and $e_{2,i\text{-}1\cap i}$ are equal to 2, 2, and 1, respectively, so the $e_{3,i}$ for the two adjacent images (left and middle) is calculated as 1.

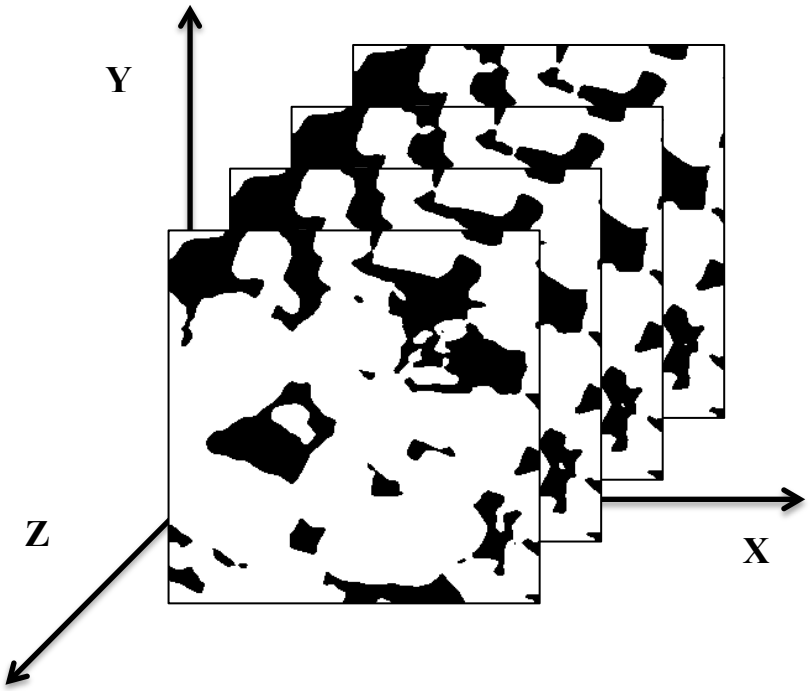

Fig. 5.2—A series of 2D micro-CT images stacking along the Z direction. White and black regions represent grains and pore space, respectively.

Finally, the 3D EPC for a rock matrix containing n 2D images is given by

$$(e_{3D})_J = \sum_{i=2}^{n} e_{3,i}, \tag{5-7}$$

where J can be either X, Y, or Z direction, which is the stacking direction of the serial 2D images. For example, if the 2D micro-CT images reside in the X-Y plane, then Equation (5-7) generates the 3D EPC in the Z direction, $(e_{3D})_Z$.

Although Vogel (1997) treated the 3D EPC calculated by Equation (5-7) as representing the pore connectivity of the whole 3D volume, it actually has directional properties, which means that the 3D EPC calculated along each direction can be different. We consider the anisotropy of 3D EPC comes from the different number of redundant connections, C, along different directions.

5.2.2. Calculation of Directional Pore-Connectivity Factor, Approach 1: Image Analysis

The major obstacle for incorporating EPC into permeability models is that it has no upper or lower limit, and it can be negative or positive. We thereby define our directional pore-connectivity factor by modifying the EPC definition. First, we calculate the number of redundant connections in each direction, C_J, using Equations (5-6) and (5-7). C_J can be calculated via

$$C_J = N - (e_{3D})_J + H = N - (\sum_{i=2}^{n} e_{3,i})_J + H, \tag{5-8}$$

where J can be either X, Y, or Z direction. Although H should be zero in all the pore-scale images, non-zero values might be observed in certain cases. The main reason for non-zero H values is the noise associated with the micro-CT scans, which might lead to noise pixels in the pores, which appear to be "suspending grains". The number of these noise pixels is counted as H, which is also a constant number regardless of directions. Both N and H can be calculated using ImageJ, a public domain, Java-based image-processing program, developed at the National Institute of Health. Then we defined the directional pore-connectivity factor, ε_J, via

$$\varepsilon_J = \left(\frac{C_J}{\sum_J C_J}\right)^p \cdot \left(\frac{N+H}{C_J}\right)^q, \tag{5-9}$$

where p and q are parameters which can be determined by multiple linear regression analysis. The first term in this definition, $C_J/\Sigma C_J$, is designed to enhance the directional property; the second term, $(N+H)/C_J$, is similar to EPC's definition (i.e. lower values of $(N+H)/C_J$ indicate better pore connectivity). Specifically, we considered rock matrices with $(N+H)/C_J \geq 1$ as poorly-connected, and with $(N+H)/C_J < 1$ as well-connected. By this definition, the directional pore-connectivity factor, ε_J, is always positive, and can be easily incorporated into NMR-based permeability models.

Next, we introduce an NMR-based directional permeability model using the defined pore-connectivity factor. The new NMR-based directional permeability model (Approach 1) is simply given by multiplying the conventional SDR model and the directional pore-connectivity factor, ε_J:

$$k_J = \lambda \cdot \phi^{\alpha} \cdot T_{2GM}^{\beta} \cdot \varepsilon_J$$
$$= \lambda \cdot \phi^{\alpha} \cdot T_{2GM}^{\beta} \cdot \left(\frac{C_J}{\sum_J C_J}\right)^p \cdot \left(\frac{N+H}{C_J}\right)^q, \quad (5\text{-}10)$$

where k_J is the directional permeability in J direction, and the parameters λ, α, β, p, and q can be determined by multiple linear regression analysis. To determine these parameters, we divided the rock samples into two groups depending on their pore connectivity, i.e. $(N+H)/C_J$ values: the rock samples with $(N+H)/C_J$ larger than or close to one are categorized in the poor-connectivity group, and those with $(N+H)/C_J$ less than one in the good-connectivity group. The sample classification was made regardless of rock lithology and only based on pore structure, which in real formations can vary in different rock facies depending on depositional environment. Finally, we applied multiple linear regression analysis within each rock group, and two sets of parameters λ, α, β, p, and q are therefore obtained.

5.2.3. Calculation of Directional Pore-Connectivity Factor, Approach 2: Electrical Formation Factor

Similar to the approach above, we introduce an alternative method to calculate the directional pore connectivity, which integrates the directional formation factor determined by electrical resistivity measurements. This second directional pore-connectivity factor, ε_J, is obtained by replacing C_J in Equation (5-10) with directional electrical formation factor, expressed as

$$\varepsilon_J = (\frac{FF_J}{\sum_J FF_J})^p \cdot (\frac{N+H}{C_J})^q, \tag{5-11}$$

where FF_J is the formation factor in J direction, assuming that the rock sample is fully saturated with water. The formation factor FF is defined as

$$FF = \frac{R_0}{R_w}, \tag{5-12}$$

where R_0 is the resistivity of a rock sample fully saturated with water, and R_w is the resistivity of water. In this paper, the directional formation factors, FF_J, of ten sandstone samples are obtained from Imperial College London (Dong 2007). The effective electrical resistivity of the samples was calculated using finite difference numerical simulation of the electrical potential distribution in porous media.

Incorporating Equation (5-11) in Equation (5-10) provides the second form of our NMR-based directional permeability model (Approach 2) as

$$\begin{aligned} k_J &= \lambda \cdot \phi^\alpha \cdot T_{2GM}^\beta \cdot \varepsilon_J \\ &= \lambda \cdot \phi^\alpha \cdot T_{2GM}^\beta \cdot (\frac{FF_J}{\sum_J FF_J})^p \cdot (\frac{N+H}{C_J})^q, \end{aligned} \tag{5-13}$$

where the parameters λ, α, β, p, and q can be determined by multiple linear regression analysis.

5.3. Carbonate, Sandstone, and Sandpack Samples for Calibration and Testing

5.3.1. Carbonate Rock Samples

This section summarizes the detailed information about the carbonate rock samples in this paper. They were from different formations with distinct physical properties and topological characteristics. Five of the carbonate rock matrices named Austin Chalk, HS_C1, HS_C4, HS_C4_1, and Sa_C3, are converted from micro-CT images scanned by W. D. Von Gonten Lab, and another two carbonate rock matrices named C1 and C2 are obtained form Imperial College London (Dong 2007). We also made two synthetic carbonate samples, C1_fractured and C2_fractured, by inserting two planar fractures into the C1 and C2 rock matrices, respectively. **Table 5.1** lists the matrix volume, the resolution of the micro-CT images, the total porosity, and the T_{2GM} value calculated from the simulated NMR T_2 distribution of each carbonate matrix. **Fig. 5.3** shows the 3D pore-scale images of all the carbonate rock samples.

Table 5.2 lists the number of isolated components, N, the number of redundant connections, C_J, the ratio of $(N+H)/C_J$, and the LBM directional permeability for each carbonate matrix, in X, Y, and Z directions. We observed that all these carbonate rock samples have $(N+H)/C_J$ ratio larger than or close to 1. Consequently, we categorized all the 9 carbonate rock samples into the group of poor connectivity ($(N+H)/C_J \geq 1$). It must be emphasized that carbonate rocks are not necessarily poorly-connected, there can be carbonate samples with $(N+H)/C_J < 1$, which should be categorized into the well-connected group.

Table 5.1—Carbonate rock samples: matrix volume, micro-CT resolutions, total porosity, and estimated T_{2GM} values of the carbonate rock matrices constructed from micro-CT images.

Matrix	Volume, pixel^3	Resolution, µm/pixel	Porosity, %	T_{2GM}, msec
C1	400x400x400	2.850	23.26	1025
C2	400x400x400	5.345	16.83	1223
C1_fractured	400x400x400	2.850	25.49	1083
C2_fractured	400x400x400	5.345	19.46	1326
Austin Chalk	600x600x600	0.700	25.44	249.5
HS_C1	600x600x600	0.900	11.89	203.2
HS_C4	600x600x600	2.700	15.37	795.7
HS_C4_1	600x600x600	3.460	20.22	914.9
Sa_C3	600x600x600	2.000	15.77	591.7

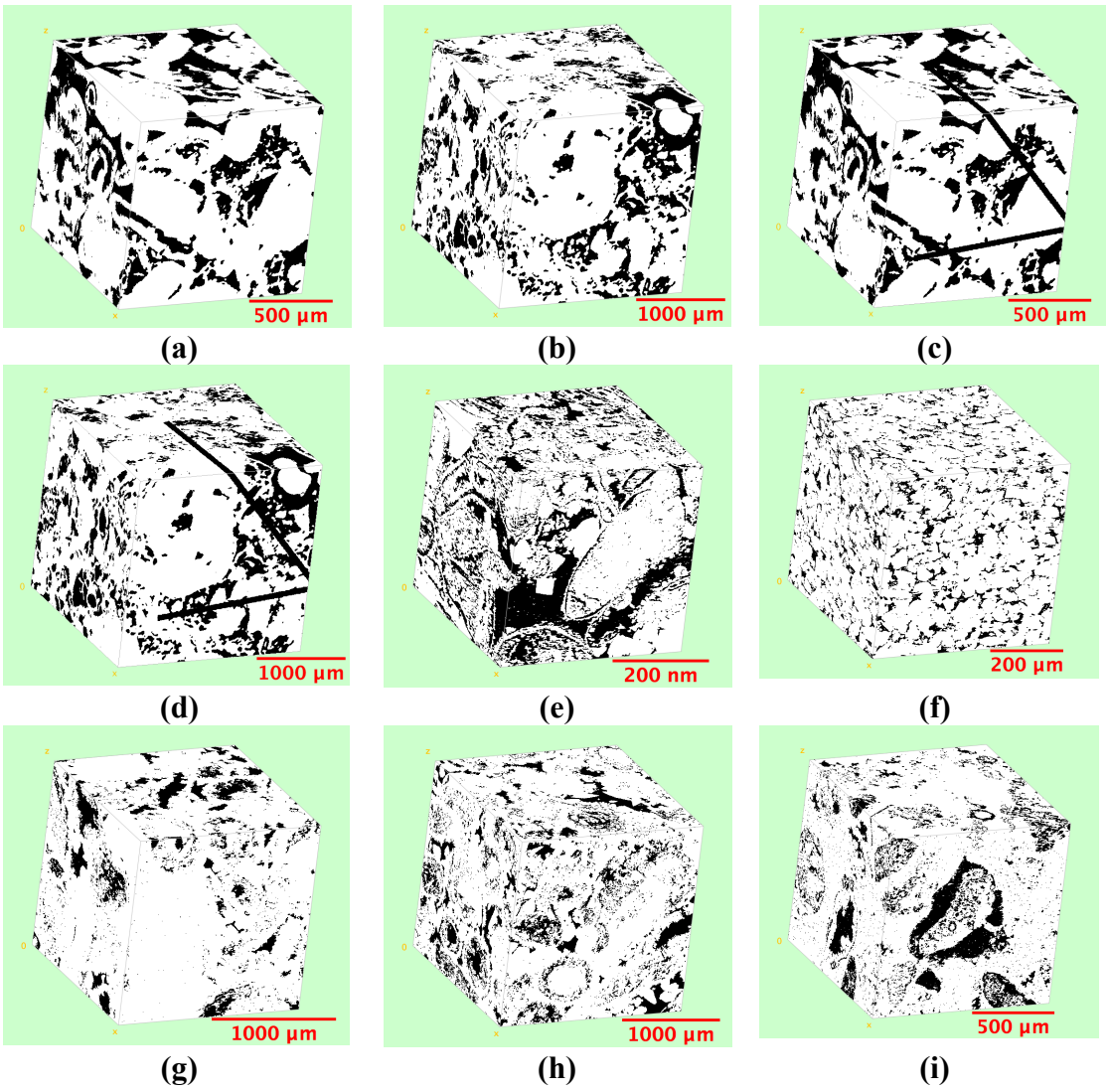

Fig. 5.3—The 3D pore-scale images of the 9 carbonate samples: (a) C1, (b) C2, (c) C1_fractured, (d) C2_fractured, (e) Austin Chalk, (f) HS_C1, (g) HS_C4, (h) HS_C4_1, and (i) Sa_C3. The white and black regions represent the grains and pore space, respectively.

Table 5.2—Carbonate rock samples: number of isolated components (N), number of redundant connections (C_J), the ratio of $(N+H)/C_J$, and the LBM directional permeability in X, Y, and Z directions.

Matrix	Direction	N	C_J	$(N+H)/C_J$	LBM Permeability, mD
C1	X	4059	5412.5	0.97	896.0
	Y	4059	5367	0.98	1688.1
	Z	4059	4794.5	1.09	1047.6
C2	X	7293	6285.5	1.24	76.5
	Y	7293	6244.5	1.25	180.6
	Z	7293	5629.5	1.38	70.4
C1_fractured	X	3808	5251	0.95	2881.1
	Y	3808	4740	1.06	1537.0
	Z	3808	5326.5	0.94	1534.0
C2_fractured	X	6925	6216.5	1.19	767.4
	Y	6925	5685	1.30	224.7
	Z	6925	6209	1.19	1071.6
Austin Chalk	X	58924	42721	1.42	16.1
	Y	58924	42266	1.43	24.2
	Z	58924	41095	1.47	17.2
HS_C1	X	19206	28493.5	0.96	4.52
	Y	19206	29158.5	0.94	3.60
	Z	19206	29444.5	0.93	2.76
HS_C4	X	56859	16473	3.57	1.80
	Y	56859	17372.5	3.39	2.68
	Z	56859	14510.5	4.05	1.89
HS_C4_1	X	84023	65188.5	1.31	81.4
	Y	84023	65890	1.30	100.6
	Z	84023	66666.5	1.28	22.3
Sa_C3	X	136124	38971.5	3.60	3
	Y	136124	36365.5	3.86	1.06
	Z	136124	31466.5	4.46	0.43

5.3.2. Sandstone and Sandpack Samples

In this section we will show 11 sandstone rock samples and one sandpack sample with distinct physical properties and topological characteristics. The sandstone rock matrix named SS1 is converted from micro-CT images scanned at Texas A&M University. All the other samples, including 10 sandstone rock matrices (S1~ S9 and Berea) and one sandpack sample (F42B), are obtained from Imperial College London (Dong 2007). **Table 5.3** shows the matrix volume, the resolution of the micro-CT images, the total porosity, and the T_{2GM} value estimated from simulated NMR T_2 distributions of each sandstone/sandpack sample. **Fig. 5.4** shows the 3D pore-scale images of all the sandstone/sandpack samples.

Table 5.4 lists the number of isolated components N, the number of redundant connections C_J, the ratio of $(N+H)/C_J$, and the LBM directional permeability for each sandstone/sandpack sample, in X, Y, and Z directions. We observed that all sandstone/sandpack samples have $(N+H)/C_J$ ratios less than 1. Thus, all of them are categorized into the group of good pore connectivity ($(N+H)/C_J < 1$).

Table 5.3—Sandstone rock samples: matrix volumes, micro-CT resolutions, total porosity, and estimated T_{2GM} values of the sandstone rock and sandpack matrices constructed from micro-CT images. Sample F42B is a sandpack sample, all the other samples are actual sandstone rock samples.

Matrix	Volume, pixel^3	Resolution, µm/pixel	Porosity, %	T_{2GM}, msec
S1	300x300x300	8.683	14.13	853.3
S2	300x300x300	4.956	24.63	589.6
S3	300x300x300	9.100	16.86	543.9
S4	300x300x300	8.960	17.13	551.1
S5	300x300x300	3.997	21.13	809.1
S6	300x300x300	5.100	23.96	1021.4
S7	300x300x300	4.803	25.05	736.8
S8	300x300x300	4.892	33.98	734.0
S9	300x300x300	3.398	22.17	697.9
Berea	400x400x400	5.345	19.65	549.8
SS1	600x600x600	3.460	21.48	452.9
F42B	300x300x300	10.002	21.48	452.9

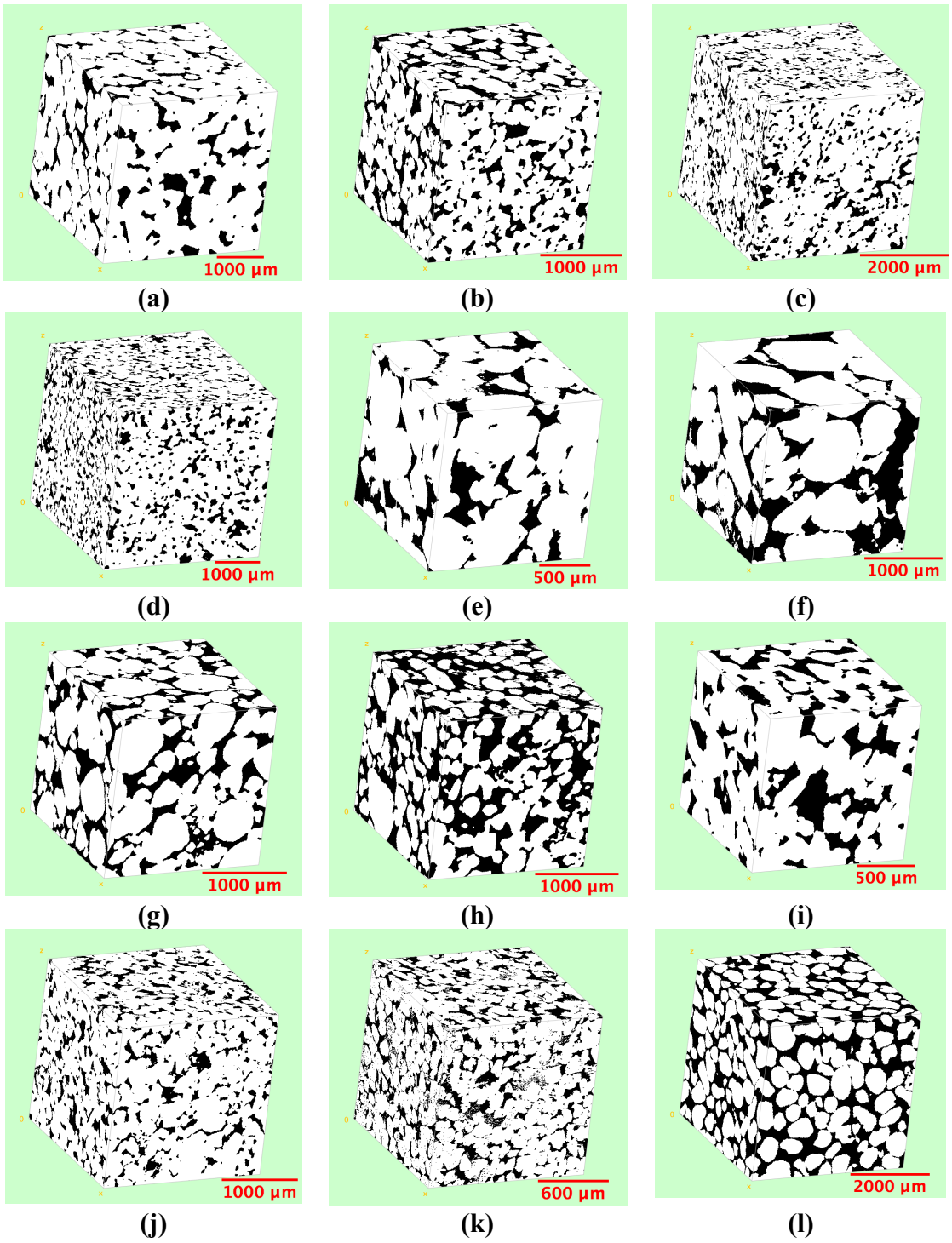

Fig. 5.4—The 3D pore-scale images of the 11 sandstone rock and one sandpack samples: (a) S1, (b) S2, (c) S3, (d) S4, (e) S5, (f) S6, (g) S7, (h) S8, (i) S9, (j) Berea, (k) SS1, and (l) F42B. The white and black regions represent the grain and pore space, respectively.

Table 5.4—Sandstone rock and sandpack samples: the number of isolated components (N), the number of redundant connections (C_J), the ratio of $(N+H)/C_J$, the directional formation factors (FF_J), and the LBM directional permeability in X, Y, and Z directions. All are real sandstone samples except F42B, which is a sandpack sample. * Formation factors calculated by Dong (2007).

Matrix	Direction	N	C_J	$(N+H)/C_J$	FF_J*	LBM Perm, mD
	X	385	1064.5	0.39	36.32	1763.5
S1	Y	385	1070	0.39	37.89	1517.1
	Z	385	975.5	0.43	53.47	1227.5
	X	463	2886.5	0.20	10.85	3927.5
S2	Y	463	2902.5	0.20	11.32	3564.0
	Z	463	2732	0.21	12.55	3134.9
	X	2288	6107.5	0.39	52.16	160.3
S3	Y	2288	6116.5	0.39	41.89	369.6
	Z	2288	5169	0.46	70.32	219.3
	X	2780	4035.5	0.80	74.5	137.8
S4	Y	2780	3995.5	0.81	71.01	150.9
	Z	2780	3245.5	0.99	114.44	112.1
	X	346	673	0.69	14.08	5126.8
S5	Y	346	672.5	0.69	14.59	5301.1
	Z	346	612.5	0.76	15.9	5525.9
	X	275	1223.5	0.58	10.26	14848.8
S6	Y	275	1248.5	0.57	11.17	11895.7
	Z	275	1159.5	0.61	12.92	11372.6
	X	222	1771	0.18	9.58	7522.4
S7	Y	222	1745	0.19	9.28	8322.3
	Z	222	1652	0.20	11.17	6104.3
	X	989	2876.5	0.41	6.02	12708.2
S8	Y	989	2865	0.41	5.97	13349.9
	Z	989	2698.5	0.44	6.53	12490.9
	X	118	447.5	0.32	16.42	2815.1
S9	Y	118	439.5	0.33	19.85	2316.8
	Z	118	438.5	0.33	18.10	2015.5
	X	2251	6792.5	0.37	23.12	1196.8
Berea	Y	2251	6719.5	0.38	23.99	1159.0
	Z	2251	6758.5	0.38	25.22	1050.5
	X	23827	47735	0.56		1005.3
SS1	Y	23827	47915.5	0.56		1205.3
	Z	23827	46277.5	0.58		1067.6
	X	270	3791.5	0.091		46292.9
F42B	Y	270	4154.5	0.083		52118.8
	Z	270	3756	0.092		49221

5.4. Calibration and Testing of the New NMR-Based Directional Permeability Model

After classification of poorly-connected (($N+H)/C_J \geq 1$) and well-connected (($N+H)/C_J < 1$) rock samples, we performed multiple linear regression analysis in each rock group, and obtain two sets of parameters for the NMR-based directional permeability model (Equation (5-10)), using the first approach (assessment of directional pore-connectivity factor using image analysis). In the poorly-connected group, we used 6 carbonate samples to calibrate the model, and the 3 carbonate samples left (C1_fractured, C2_fractured, and HS_C4_1) are later used as test samples to evaluate the reliability of the model. In the well connected rock sample group, we used 11 sandstone/sandpack samples for calibration, and one sandstone sample (S2) for testing the reliability of the model. **Table 5.5** lists the model parameters in Equation (5-10), calibrated by multiple linear regression analysis, for each rock group.

Table 5.5—Parameters estimated for the new NMR-based directional permeability model, Equation (5-10), using the first proposed approach (i.e. using image analysis) for assessment of directional pore connectivity.

	λ	α	β	p	q
$(N+H)/C_J \geq 1$	1.12	3.61	1.79	0.87	-2.91
$(N+H)/C_J < 1$	1.41E-4	3.94	3.49	0.67	-0.75

Using the first approach for calibration of NMR-based permeability model (Equation (5-10)), the directional permeability, k_J, for the poorly-connected and well-connected rock samples are given by

$$k_J = 1.12 \cdot \phi^{3.61} \cdot T_{2GM}^{1.79} \cdot \left(\frac{C_J}{\sum_J C_J}\right)^{0.87} \cdot \left(\frac{N+H}{C_J}\right)^{-2.91}, \quad (5\text{-}14)$$

and

$$k_J = 1.41 \times 10^{-4} \cdot \phi^{3.94} \cdot T_{2GM}^{3.49} \cdot \left(\frac{C_J}{\sum_J C_J}\right)^{0.67} \cdot \left(\frac{N+H}{C_J}\right)^{-0.75}, \quad (5\text{-}15)$$

respectively, where porosity, ϕ, is in volume fraction (i.e. $0 < \phi < 1$).

Looking at the estimated model parameters in Equations (5-14) and (5-15), the porosity exponent is 3.94 for well-connected rock samples, which is very close to the default value of 4 in the original SDR model. In fact, the power 4th for the porosity can be theoretically demonstrated by Navier-Stokes and Darcy's laws (Chauveteau et al. 1996; Fleury et al. 2001), and has been supported by various experimental data. On the other hand, for poorly-connected rock samples the porosity exponent is 3.61, which is less than that of well-connected samples, confirming that permeability of carbonate rock samples might not be well correlated to their porosity. Furthermore, the exponents of T_{2GM} are 1.79 and 3.49 for poorly-connected and well-connected samples, respectively, which are also close to the default value in the original SDR model. The aforementioned observations provide a strong support to the reliability of our parameter calibration.

The multiple linear regression results were obtained for the poorly-connected and well-connected rock samples, respectively (**Fig. 5.5**). Three data points are shown

for each rock sample, representing the permeability in X, Y, and Z directions. The linear correlations given by Equations (5-14) and (5-15) are used to fit these data points.

The calibration and testing results for the new NMR-based directional permeability model (**Fig. 5.6**) were obtained using the first approach (Equation (5-10)). The new NMR-based directional permeability estimates are compared against the LBM-derived permeability data, which is considered as the reference target of permeability. Three data points are shown for each rock sample, representing the permeability in X, Y, and Z directions. In Fig. 5.6a, all the calibration samples are well aligned along the diagonal line; in Fig. 5.6b, we observed close agreement between the NMR estimated directional permeability and LBM permeability for the four testing samples (C1_fractured, C2_fractured, HS_C4_1, and S2), and all the permeability estimates show anisotropic properties in three directions. For all the carbonate, sandstone, and sandpack samples, 80% of the NMR-estimated permeability values were accurate within a factor of two, and the other 20% were accurate within a factor of five. The correlation coefficient R^2 is calculated as 0.88 for all the rock samples. The permeability values illustrated in Figs. 5.6a and 5.6b cover six orders of magnitude (from 0.1 mD to 100,000 mD), showing the smallest rock permeability of approximately 0.4 mD (carbonate sample, Sa_C3), and the largest of approximately 52,000 mD (sandpack sample, F42B). These results confirm that our NMR-based directional permeability model can be reliably applied to a wide variety of rock samples from different formations.

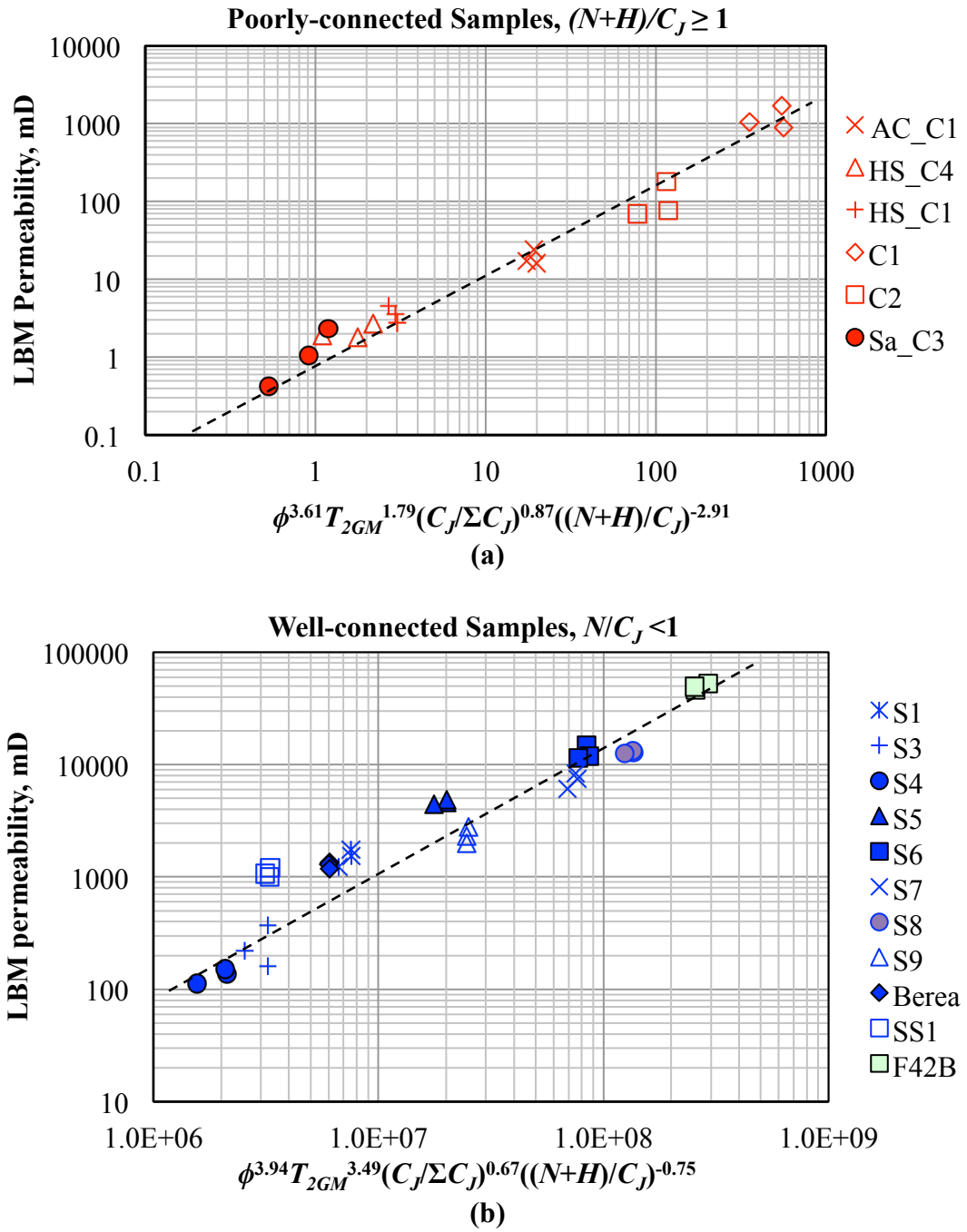

Fig. 5.5—The permeability correlations for (a) poorly-connected samples ($(N+H)/C_J \geq 1$) and (b) well-connected samples ($(N+H)/C_J < 1$). The black dash lines in the figures show the linear correlation used to fit the data points. For each rock sample, three data points are shown to represent the permeability in X, Y, and Z directions.

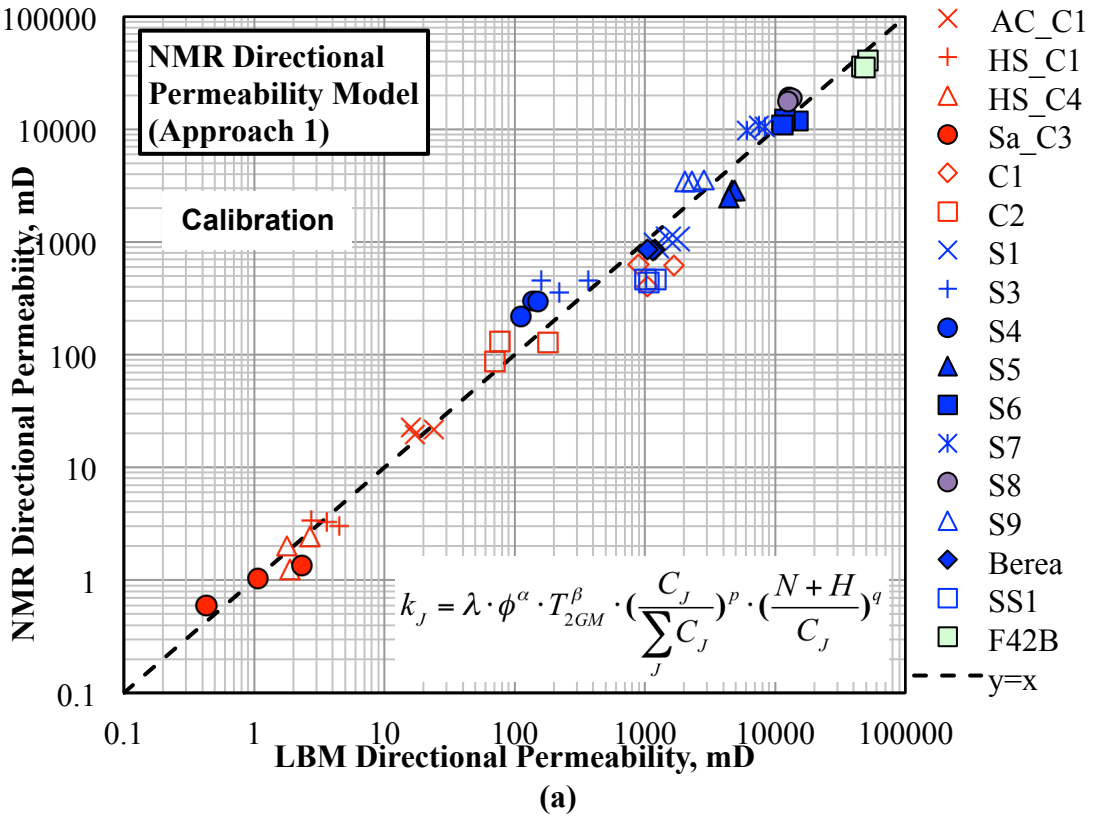

(a)

Fig. 5.6—(a) Calibration and (b) testing results for the new NMR-based directional permeability model using the first approach (Equation (5-10)) for assessment of directional pore connectivity. The red, blue, and green data points represent carbonate, sandstone, and sandpack (F42B) samples, respectively. All the rock samples shown in Figure (a) are used for calibration. The four additional samples in Figure (b), including S2, C1_fractured, C2_fractured, and HS_C4_1, are used for testing the model. In both figures the permeability estimates from NMR-based directional permeability model are compared against the LBM directional permeability. For each rock sample, three data points are shown to represent the permeability in X, Y, and Z directions.

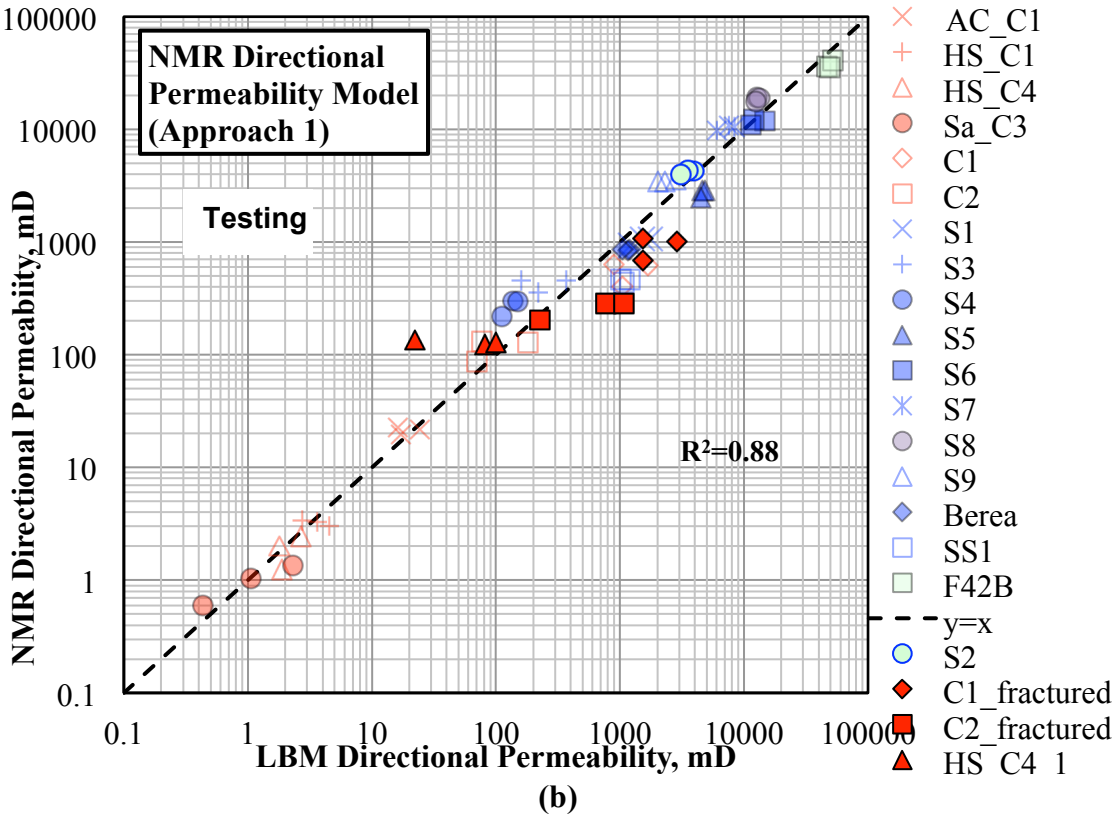

(b)

Fig. 5.6 Continued.

We emphasize that only one calibration step, i.e. the multiple linear regression analysis, is required for the new NMR-based directional permeability model. No further effort is needed to adjust model parameters for new rock samples from different formations. When applying the model to new rock samples and rock types, the only required action is to estimate porosity and NMR T_{2GM} from NMR measurements, and to calculate the directional connectivity factor from pore-scale images of rock sample representatives from different rock types in the formation.

Furthermore, we applied the second approach (assessment of directional pore-connectivity factor using electrical formation factor) for assessment of model parameters the sandstone rock samples, i.e. the well-connected group. We used 9 sandstone samples for calibration, and one sandstone sample (S2) for testing. **Table 5.6** lists the calibrated model parameters in Equation (5-13) by multiple linear regression analysis for the well-connected group.

Table 5.6—Parameters estimated for the new NMR-based directional permeability model, Equation (5-13), using the second proposed approach (i.e. using electrical formation factor and image analysis) for assessment of directional pore connectivity.

	λ	α	β	p	q
$(N+H)/C_J \geq 1$	--	--	--	--	--
$(N+H)/C_J < 1$	4.98E-9	3.41	4.72	-0.46	-0.70

Using the second approach for NMR-based permeability model (Equation (5-13)), the directional permeability for well-connected rock samples are estimated as

$$k_J = 4.98\times10^{-9}\cdot\phi^{3.41}\cdot T_{2GM}^{4.72}\cdot\left(\frac{FF_J}{\sum_J FF_J}\right)^{-0.46}\cdot\left(\frac{N+H}{C_J}\right)^{-0.70}, \tag{5-16}$$

where porosity, ϕ, is in volume fraction (i.e. $0 < \phi < 1$).

The calibration and testing results for the NMR directional permeability model (**Fig. 5.7**) were obtained using the second approach, Equation (5-13). Fig. 5.7b illustrates a close agreement between the NMR-based estimates of directional permeability and LBM permeability for the testing sample, S2, while the permeability estimates show anisotropic properties. The correlation coefficient R^2 is calculated as 0.94 for all the sandstone rock samples. The results indicate that directional permeability of rock samples can be estimated by combining NMR and electrical resistivity measurements, and the directional electrical formation factor is a good candidate for reflecting the anisotropic characteristic of rock permeability.

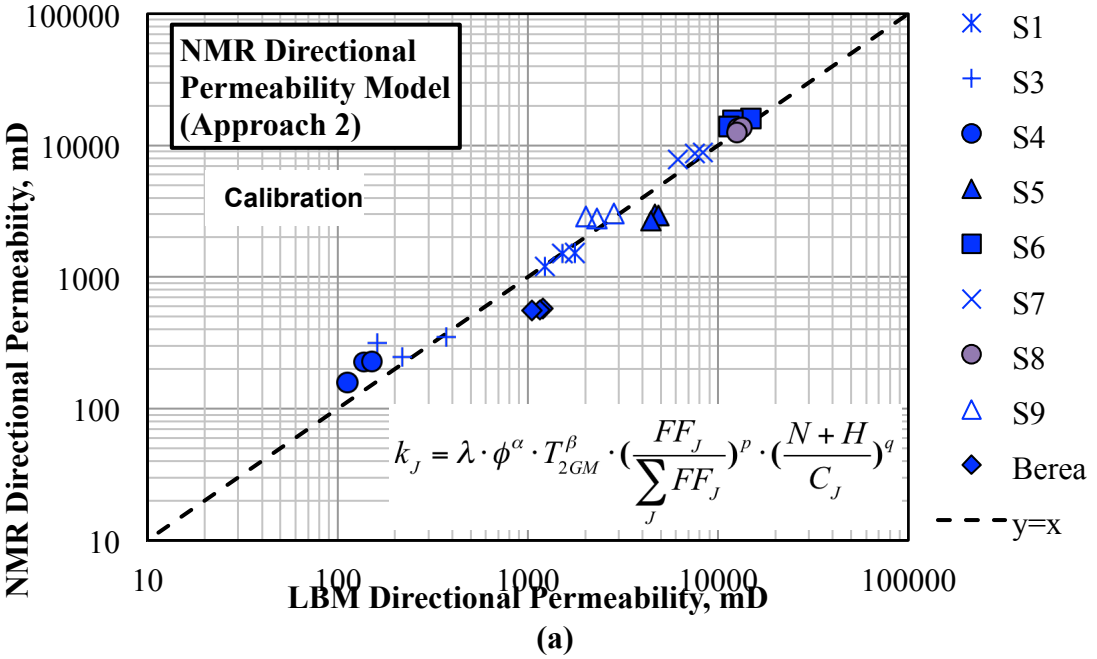

(a)

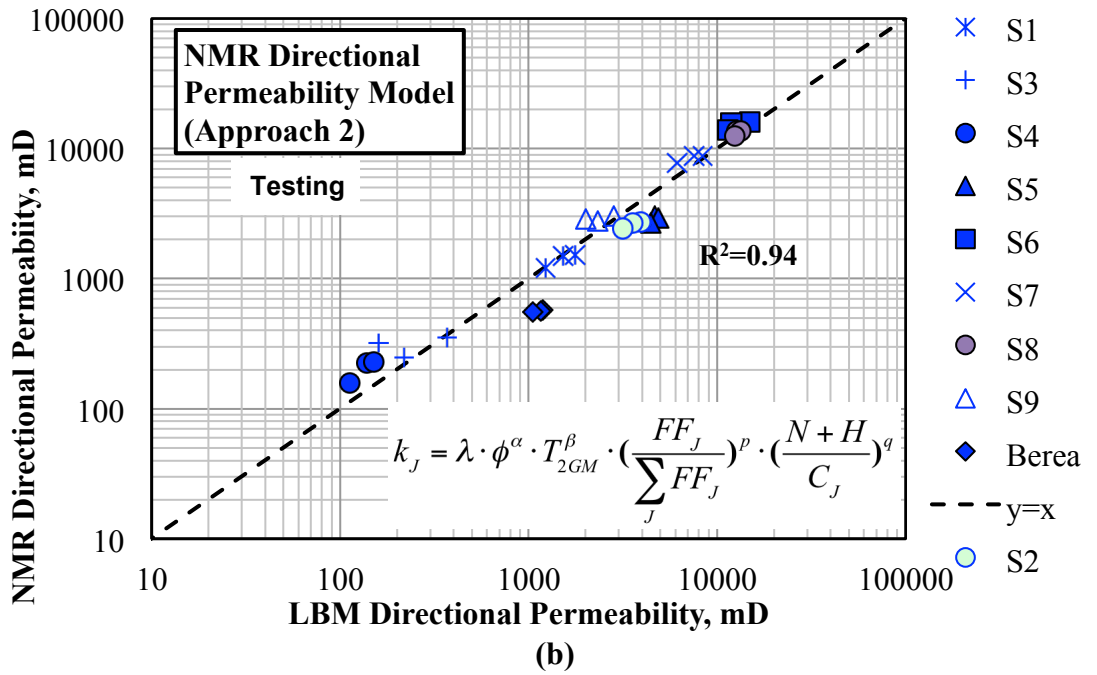

(b)

Fig. 5.7—(a) Calibration and (b) testing results for the new NMR-based directional permeability model using the second approach (Equation (5-13)) for assessment of directional pore connectivity. All the data points represent sandstone samples. In both figures the permeability estimates from NMR-based directional permeability model are compared against the LBM directional permeability. For each rock sample, three data points are shown to represent the permeability in X, Y, and Z directions.

Table 5.7—The coefficient *C* in the original SDR permeability model adjusted for all rock samples: (a) the carbonate rock samples, and (b) the sandstone/sandpack samples.

	C
C1	0.004
C2	0.004
C1_frac	0.004
C2_frac	0.004
AC_C1	0.004
HS_C1	0.004
HS_C4	0.0002
HS_C4_1	0.0002
Sa_C3	0.0001

(a)

	C
S1	0.025
S2	0.025
S3	0.025
S4	0.025
S5	0.025
S6	0.025
S7	0.025
S8	0.025
S9	0.025
Berea	0.025
SS1	0.025
F42B	0.1

(b)

5.5. Permeability Assessment using Conventional NMR-Based Permeability Models

This section shows assessment of permeability for the same sandstone, carbonate, and sandpack samples using the conventional NMR-based permeability models, including the original SDR model, the modified SDR model, and the Coates model. These examples demonstrate the extensive case-by-case calibration effort required by conventional techniques. **Fig. 5.8a** shows the permeability estimates for all rock samples using original SDR model compared against the LBM-derived permeability. The parameters *a* and *b* in the original SDR model (Equation (5-2)) adopt the default values of 4 and 2, respectively. The SDR model requires calibration of the coefficient *C* based on LBM permeability, or lab measured permeability, for different rock types. We adjusted the coefficient *C* for different rock types, as listed in **Table 5.7**, to get the best possible match to LBM permeability using SDR model. After calibration of coefficient *C* in SDR model, some of the SDR permeability estimates still deviate from the LBM directional permeability by approximately an order of magnitude, and none of them show anisotropic property in X, Y, and Z directions.

Fig. 5.8b shows the permeability estimates using the modified SDR model (Chang et al. 1997) compared against the LBM directional permeability, for the carbonate rock samples. We applied the modified SDR model only to carbonate rock samples because the model was originally designed for vuggy carbonate formations and is not suitable for sandstone rock samples (Chang et al. 1997). The parameters *a* and *b*

in the modified SDR model (Equation (5-3)) adopt the default values of 4 and 2, respectively. We adjusted coefficient C to 25 for four carbonate samples (C1, C2, C1_fractured, C2_fractured), and 0.004 for all the other carbonate samples, respectively. Only by calibrating the coefficient for different rock types can this model provide a reasonable estimation of rock permeability, without capturing anisotropic characteristics.

Fig. 5.9 shows the permeability estimates using Coates model compared against the LBM directional permeability for all the rock samples. The parameters C, m, and n in the original Coates model (Equation (5-4)) adopt the default values of 10, 4, and 2, respectively. We adjusted the cutoff value, $T_{2cutoff}$, in the Coates model for each sample to obtain the best estimate of permeability. The adjusted $T_{2cutoff}$ values vary significantly from 199.7 msec to 1086.9 msec. **Table 5.8** lists the adjusted $T_{2cutoff}$ values for each rock sample.

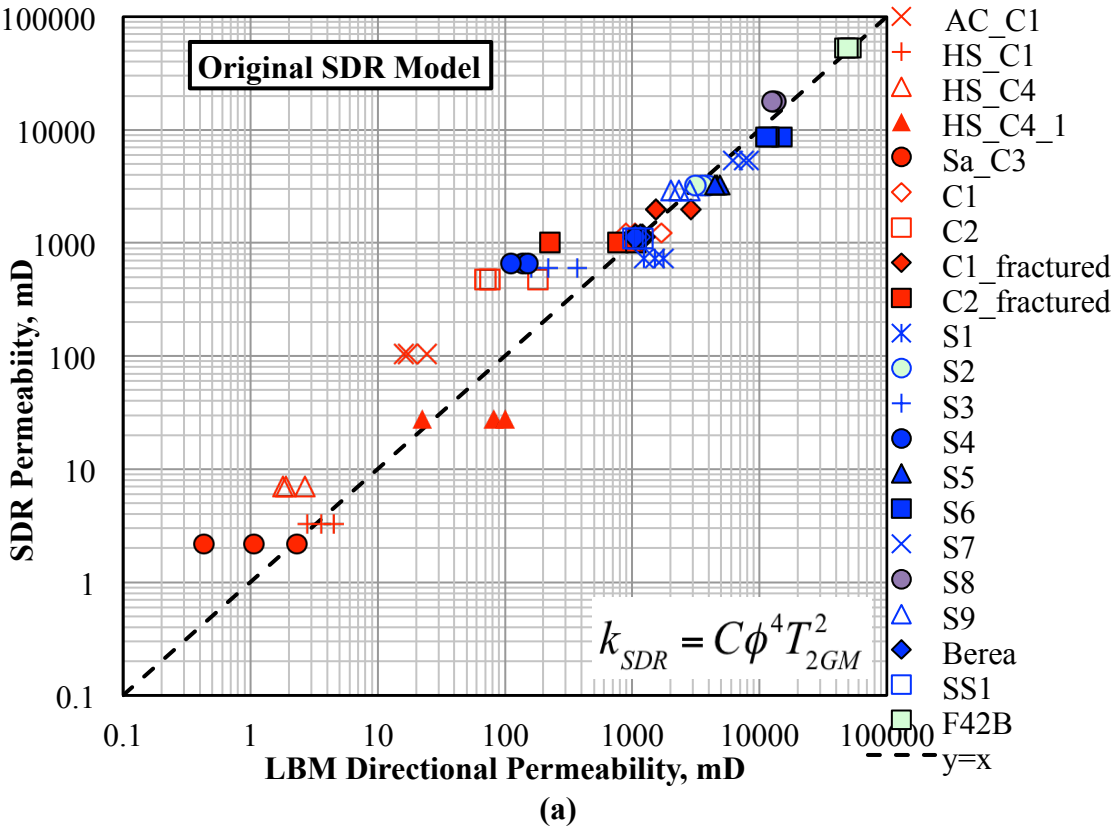

(a)

Fig. 5.8—Permeability estimates from SDR models compared against the LBM permeability: (a) the original SDR model for all the rock samples, and (b) the modified SDR model (Chang et al. 1997) for the 9 carbonate samples. Coefficient C in both original and modified SDR models is adjusted for different rock types to match the results. The red, blue, and green data points represent carbonate, sandstone, and sandpack (F42B) samples, respectively. In both figures the permeability estimates from NMR-based directional permeability model are compared against the LBM directional permeability. For each rock sample, three data points are shown to represent the permeability in X, Y, and Z directions.

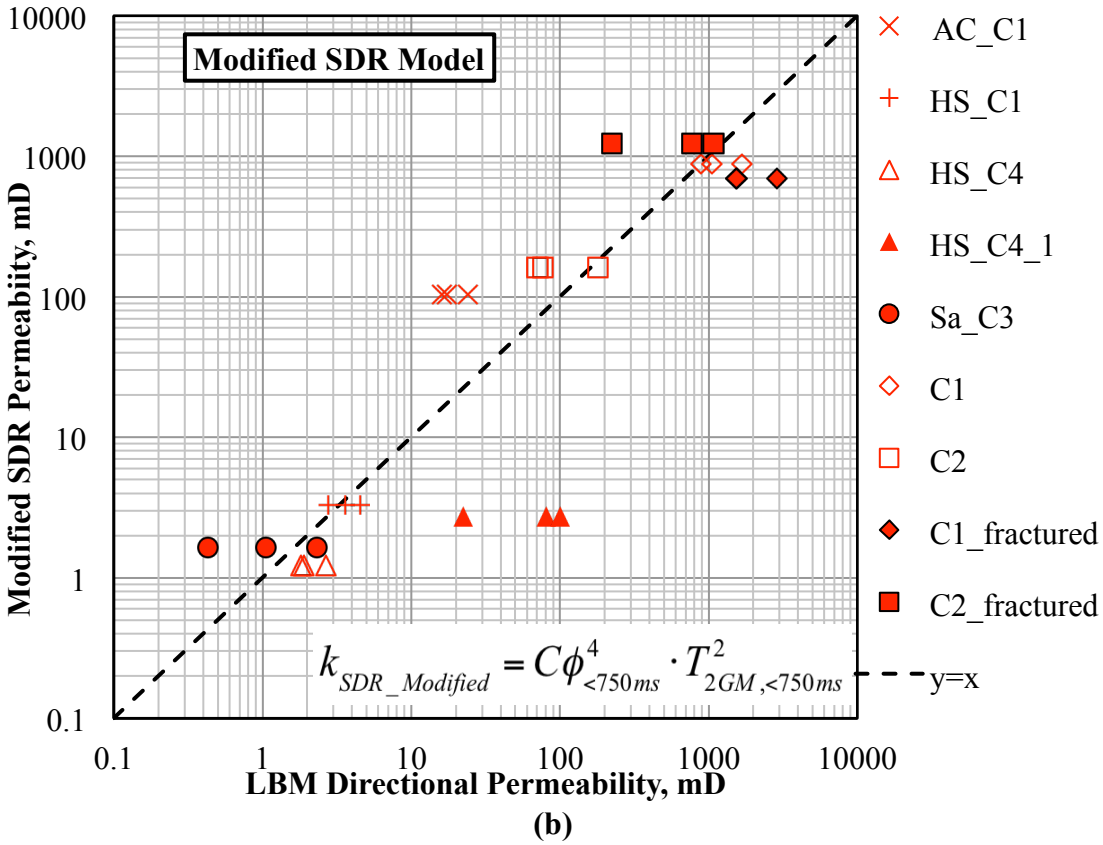

(b)

Fig. 5.8 Continued.

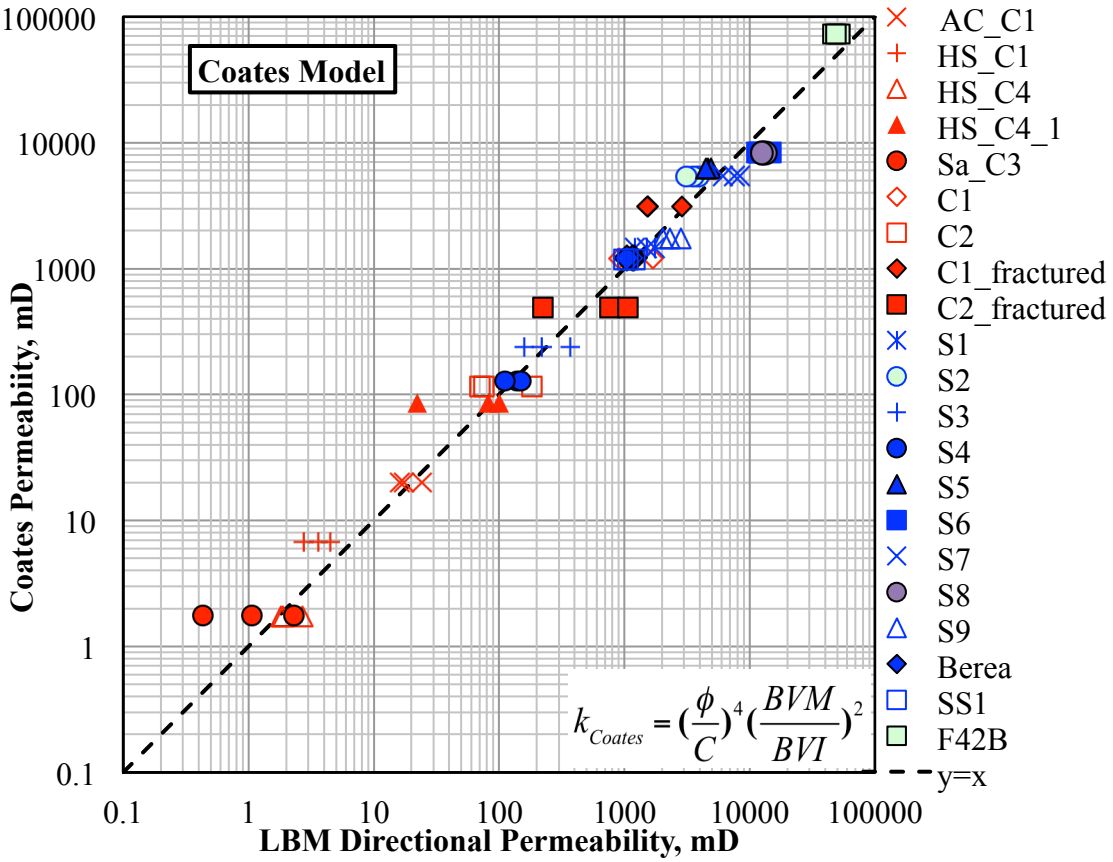

Fig. 5.9—Permeability estimates from Coates model compared against the LBM permeability for all the rock samples. The red, blue, and green data points represent carbonate, sandstone, and sandpack (F42B) samples, respectively. For each rock sample, three data points are shown to represent the permeability in X, Y, and Z directions. $T_{2cutoff}$ in the Coates model is adjusted for each rock sample to match the results as listed in Table 5.8.

Table 5.8—$T_{2cutoff}$ values in the Coates permeability model adjusted for all rock samples: (a) the carbonate rock samples, and (b) the sandstone/sandpack samples.

	$T_{2cutoff}$, msec
C1	774.3
C2	954.1
C1_frac	774.3
C2_frac	954.1
AC_C1	295.4
HS_C1	199.8
HS_C4	1086.9
HS_C4_1	645.4
Sa_C3	932.6

(a)

	$T_{2cutoff}$, msec
S1	470.3
S2	341.1
S3	470.3
S4	422.5
S5	275.4
S6	422.5
S7	379.7
S8	523.4
S9	422.5
Berea	373.3
SS1	281.8
F42B	199.7

(b)

5.6. Discussions

We demonstrated that the introduced NMR-based permeability model can be successfully applied to sandstone and carbonate rock samples with complex pore structures, in which the key step is to calculate the directional pore connectivity factor from micro-CT images or from electrical formation factor. The results of permeability assessment using the new NMR-based model and the conventional ones show that none of the conventional NMR-based permeability models, including SDR, modified SDR, and Coates model, is able to reflect the anisotropic characteristics of rock permeability. Furthermore, they all require significant adjustments of model parameters for different rock types to provide reliable permeability estimates. For instance, SDR model requires adjustment of coefficient C for different rock types, and Coates model needs calibration of $T_{2cutoff}$ for different formations. In comparison to conventional methods, the new NMR-based directional permeability model can predict the anisotropic rock permeability values reliably for a wide variety of rock types, and does not require case-by-case adjustments of model parameters.

We considered the multiple linear regression analysis as the calibration step, which is required only once for model development, using rock samples with various pore geometry and a wide range of permeability. When applying the NMR-based directional permeability model to new rock samples from new formations, no further calibration is needed on the model parameters. Therefore, our proposed NMR-based directional permeability model significantly improves permeability assessment for rock

samples with complex pore structures, by showing anisotropic rock permeability and minimizing the need for model parameter adjustment. The new model, however, requires reliable micro-CT scans on rock samples, which prevents real-time application of this model, unless approximations for pore-connectivity factor are available. Furthermore, the new NMR directional permeability model is not restricted to carbonate and sandstone formations. It can also be applied to unconventional formations such as organic-rich mudrocks, if we have reliable permeability data and pore-scale images of organic-rich mudrock samples, and include them in the model-calibration process in the future.

The results from the pore-scale simulations are promising for reliable well-log-based applications of the new NMR-based permeability model. We hereby proposed a method to combine the new NMR-based model with other well logs to estimate depth-by-depth directional permeability in complex formations. The first step is to apply rock classification based on conventional well logs. The directional connectivity can then be calculated for each rock type using either of the two approaches proposed in this paper. We assumed that the directional pore connectivity factor calculated for each rock type remains consistent for other samples in the same rock type. Finally we can apply the new model for depth-by-depth assessment of directional permeability using borehole NMR measurements free of any calibration effort.

The results from the second approach for assessment of directional pore connectivity factor, which includes the combined use of electrical formation factor and NMR measurements, is a first attempt to incorporate the electrical formation factor into NMR-based permeability model. The future work includes testing more rock samples and obtaining reliable model parameters, while combining interpretation of borehole NMR and directional electrical conductivity measurements.

5.7. Conclusions

The proposed NMR directional permeability model incorporates a directional pore-connectivity factor for reliable assessment of anisotropic rock permeability. We successfully calibrated and tested the proposed NMR directional permeability model using carbonate, sandstone, and sandpack samples from different formations. Results showed that the directional permeability values estimated by the new model were in close agreement with LBM-derived permeability values: 80% of the model-estimated permeability values were accurate within a factor of two, and the other 20% were accurate within a factor of five. The estimated permeability range covered six orders of magnitude from 0.1 mD to 100,000 mD, indicating that our NMR directional permeability model can be reliably applied to a wide variety of rock samples from different formations.

The new model reflects the anisotropic characteristics of rock permeability and enables reliable assessment of directional permeability, which the conventional NMR

models are not able to do. Furthermore, conventional NMR-based permeability models require calibration of model parameters for different rock types, while the new model minimizes the parameter calibration effort, and shows promising potential as a general model for all rock types. Our NMR directional permeability significantly improves permeability assessment in formations with complex pore structure compared to conventional NMR permeability models. It can also be applied to unconventional formations such as organic-rich mudrocks, if we have reliable permeability data of organic-rich mudrock samples and include them in the model-calibration process in the future.

We further proposed a workflow for application of this new NMR-based permeability model to estimate depth-by-depth permeability in real formations when combined with other well logs. By assuming that rock samples in the same rock class have the same directional pore-connectivity factor, one can apply the new NMR model to estimate the depth-by-depth directional permeability in real formations after conventional rock classification.

6. INFLUENCES OF FRACTURE-PORE DIFFUSIONAL COUPLING ON NMR PERMEABILITY ASSESSMENT

As discussed in Section 3, NMR fracture-pore diffusional coupling effect might significantly influence the NMR T_2 distribution in multiple-pore-type systems, which leads to misinterpretation of pore size distribution of rock samples. It is natural to presume that distortion of T_2 distribution can influence the permeability estimates from NMR relaxometry. Nevertheless, these influences have not been investigated. This section quantifies the impacts of micro-fractures and fracture-pore coupling on NMR permeability assessment and evaluates the reliability of conventional NMR permeability models and the new NMR directional permeability model, which was introduced in Section 5.

6.1. Introduction

Due to its sensitivity to pore size distribution in rock samples, NMR relaxometry has been used to estimate rock permeability. The most extensively used NMR-based permeability models include the SDR model (Kenyon et al. 1986) and the Coates model (Coates et al. 1997). In addition, we introduced in Section 5 and previous publications (Chi and Heidari 2015b) an NMR directional permeability model to estimate the anisotropic permeability of rock samples with complex pore structure, by incorporating a directional pore-connectivity factor. The SDR model and the NMR directional permeability model both rely on the calculation of geometric mean of T_2 distribution,

i.e. T_{2GM} values, while the Coates model depends on selecting a T_2 cutoff value on the T_2 distribution curve to differentiate the movable and irreducible fluids. However, all the NMR permeability models aforementioned are based on the assumption that the NMR T_2 distribution represents the real pore-size distribution of rock samples. In a recent publication (Chi and Heidari 2015a) and in Section 3 we showed that NMR T_2 distribution can be significantly influenced by the presence of micro-fractures and this phenomena is named fracture-pore diffusional coupling effect. Under the influences of fracture-pore diffusional coupling, the slow relaxing T_2 peak in a fractured rock sample shifts downwards in the NMR T_2 distribution and increases in amplitude, while the fast relaxing T_2 peak remains almost at its original T_2 position and decreases in amplitude. The slow and fast relaxing T_2 peaks can be micro-fractures and inter-granular pores in a rock sample, and vice versa, depending on their relative size.

This distortion of NMR T_2 distribution caused by fracture-pore diffusional coupling naturally arouses questions about NMR permeability assessment. Therefore, in this section we quantified the impact of micro-fractures and fracture-pore diffusional coupling on NMR permeability estimates, and evaluated the reliability of conventional NMR permeability models (i.e., SDR and Coates model) and the NMR directional permeability model in various fractured carbonate rock samples. The following two sections lay out the simulation results in two types of synthetic examples.

6.2. Synthetic Case No.1: Carbonate Samples Containing Wide Planar Micro-Fractures

In this section, we show four synthetic cases where carbonate rock samples contain planar micro-fractures with apertures larger than the inter-granular pore size, i.e. wide fractures. The four carbonate samples are denoted as HS_C1, Sa_C3, C1, and C2, and after inserting synthetic micro-fractures, HS_C1_frac, Sa_C3_frac, C1_frac, and C2_frac, respectively (**Fig. 6.1**). **Table 6.1** lists the matrix volumes, micro-CT image resolutions, total porosity, T_{2GM} values estimated from the simulated NMR T_2 distributions, and the LBM permeability from fluid flow simulations for all the carbonate rock samples, before and after inserting micro-fractures.

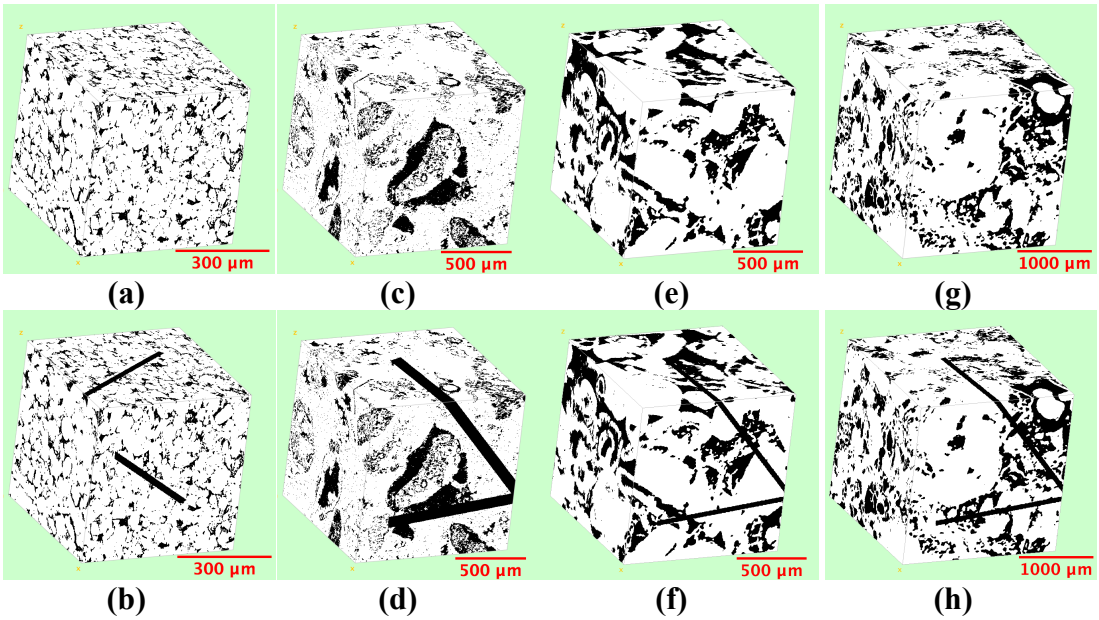

Fig. 6.1—The 3D pore-scale images of the carbonate samples before and after inserting micro-fractures: (a) HS_C1, (b) HS_C1_frac, (c) Sa_C3, (d) Sa_C3_frac, (e) C1, (f) C1_frac, (g) C2, and (h) C2_frac. The white and black regions represent the grains and pore space, respectively.

Table 6.1—Carbonate samples with planar fractures wider than pore size (i.e., wide fractures): matrix volume, micro-CT resolutions, total porosity, estimated T_{2GM} values, and LBM permeability in three directions of the rock matrices.

Matrix	Volume, pixel^3	Resolution, μm/pixel	Porosity, %	T_{2GM}, msec	LBM Permeability, mD	
HS_C1	600x600x600	0.900	11.89	203.2	X: Y: Z:	4.5 3.6 2.8
HS_C1_frac	600x600x600	0.900	15.07	278.6	X: Y: Z:	9.6 23.6 166.9
Sa_C3	600x600x600	2.000	15.77	591.7	X: Y: Z:	2.3 1.1 0.4
Sa_C3_frac	600x600x600	2.000	20.97	859.8	X: Y: Z:	1.7 4. 9 1.7
C1	400x400x400	2.850	23.26	1024.8	X: Y: Z:	896.0 1688.1 1047.9
C1_frac	400x400x400	2.850	25.49	1083.4	X: Y: Z:	2881.1 1537.0 1534.0
C2	400x400x400	5.345	16.83	1223.0	X: Y: Z:	76.5 180.2 70.4
C2_frac	400x400x400	5.345	19.46	1326.4	X: Y: Z:	767.4 224.7 1071.6

Fig. 6.2 shows the simulated NMR T_2 distribution curves for all the carbonate rock samples before and after inserting micro-fractures, and the isolated micro-fractures. In **Fig. 6.2a** the NMR simulation results for HS_C1_frac clearly show the characteristics of fracture-pore diffusional coupling, (i.e. the slow relaxing T_2 peak of micro-fractures (black dash curve) shifts downward), as denoted by the red arrow; while

the fast relaxing T_2 peak of inter-granular pores in the carbonate sample (black solid curve) remains at the same T_2 position. In the case of Sa_C3_frac in **Fig. 6.2b**, the fracture-pore diffusional coupling is also observed; however, because the fracture T_2 peak (black dash curve) is close to the original carbonate pore T_2 peak (black solid curve), after downshifting the two T_2 peaks merge to one (red curve). In the cases of C1_frac and C2_frac in **Figs. 6.2c** and **6.2d**, where the original carbonate pore T_2 peak overlaps the fracture T_2 peak, the influences of fracture-pore diffusional coupling is minimal so that the NMR T_2 distribution does not show a measurable distortion.

The new NMR directional permeability model is calibrated only once based on the rock samples in Section 5 and in a previous publication (Chi and Heidari 2015b), which includes the original carbonate samples HS_C1, Sa_C3, C1, and C2. The model parameters from previous calibration are listed in Table 5.5 in Section 5. We used the same parameters here to predict the directional permeability for the fractured rock samples. On the other hand, the SDR and Coates model were calibrated for each original carbonate sample, with model parameters listed in **Tables 6.2** and **6.3**. Then, we used the parameters from original carbonate samples to predict permeability for their corresponding fractured rock samples.

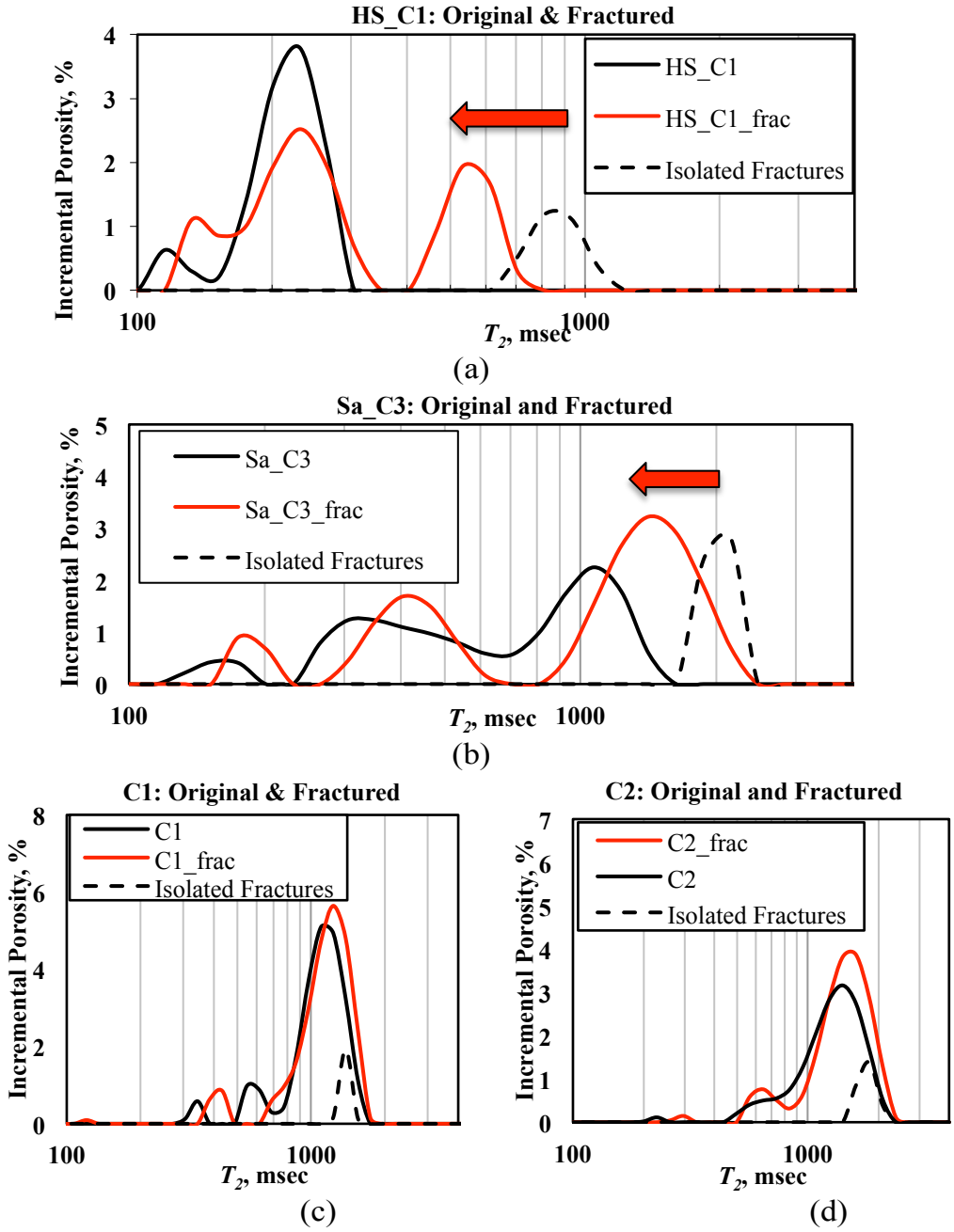

Fig. 6.2—Carbonate samples containing planar fractures wider than pore size (i.e., wide fractures): The simulated NMR T_2 distribution curves for the four carbonate samples before and after inserting micro-fractures, (a) HS_C1 and HS_C1_frac, (b) Sa_C3 and Sa_C3_frac, (c) C1 and C1_frac, and (d) C2 and C2_frac. The black solid curves, red solid curves, and black dash curves show the NMR T2 distribution for the original rock samples, fractured rock samples, and isolated fractures, respectively.

Table 6.2—Carbonate samples with planar fractures wider than pore size (i.e., wide fractures): The assumed *C* parameter in SDR model adjusted for each rock sample and the permeability estimates from SDR model.

Matrix	Parameter *C*	SDR Permeability, mD
HS_C1	0.004	3.3
HS_C1_frac	0.004	16.0
Sa_C3	0.0001	2.2
Sa_C3_frac	0.0001	14.3
C1	0.004	1229.6
C1_frac	0.004	1983.0
C2	0.001	120.0
C2_frac	0.001	252.2

Table 6.3—Carbonate samples with planar fractures wider than pore size (i.e., wide fractures): The assumed $T_{2\text{cutoff}}$ value in Coates model adjusted for each rock sample and the permeability estimates from Coates model.

Matrix	$T_{2cutoff}$, msec	Coates Permeability, mD
HS_C1	199.8	6.7
HS_C1_frac	199.8	49.2
Sa_C3	932.6	1.8
Sa_C3_frac	932.6	55.6
C1	774.3	1193.7
C1_frac	774.3	3096.2
C2	954.1	147.1
C2_frac	954.1	554.0

Fig. 6.3 shows the NMR permeability estimates from different models compared against LBM permeability for all the carbonate samples before and after inserting wide micro-fractures. Three data points are shown for each rock sample representing the permeability in the X, Y, and Z directions. In **Fig. 6.3a** the NMR directional permeability estimates show anisotropic characteristic in the X, Y, and Z directions,

while the SDR and Coates models in **Figs. 6.3b** and **6.3c** only predict an absolute permeability value for each rock sample, without capturing anisotropy.

Table 6.4 lists the relative decrease of fracture T_2 from their original values, and the relative errors in permeability estimation by NMR directional permeability model, SDR model, and Coates model, compared against LBM permeability. We categorized the carbonate rock samples in two scenarios according to the fracture T_2 decrease: (a) the rock samples with minimal fracture-pore diffusional coupling (i.e., C1 and C2, where fracture T_2 decreased by 11.0% to 12.2% from their original value), and (b) those with significant fracture-pore diffusional coupling (i.e., HS_C1 and Sa_C3, where fracture T_2 decreased by 34.2% from their original value). In the first scenario, all the three models reliably predict the permeability of fractured samples within one order of magnitude compared to LBM permeability (Fig. 6.3 and Table 6.4). In the second scenario, however, the reliability of three models varies significantly. Table 6.4 shows that the relative errors of permeability estimates for HS_C1_frac are 32-90% using the SDR and directional permeability model, but increase significantly to 70-414% using the Coates model; the relative errors for Sa_C3_frac are 13-305% using directional permeability model, 193-749% using SDR model, and increase significantly to 1038-3203% using Coates model. These results clearly show that Coates model can overestimate the permeability for rock samples with significant fracture-pore diffusional coupling by up to two orders of magnitude.

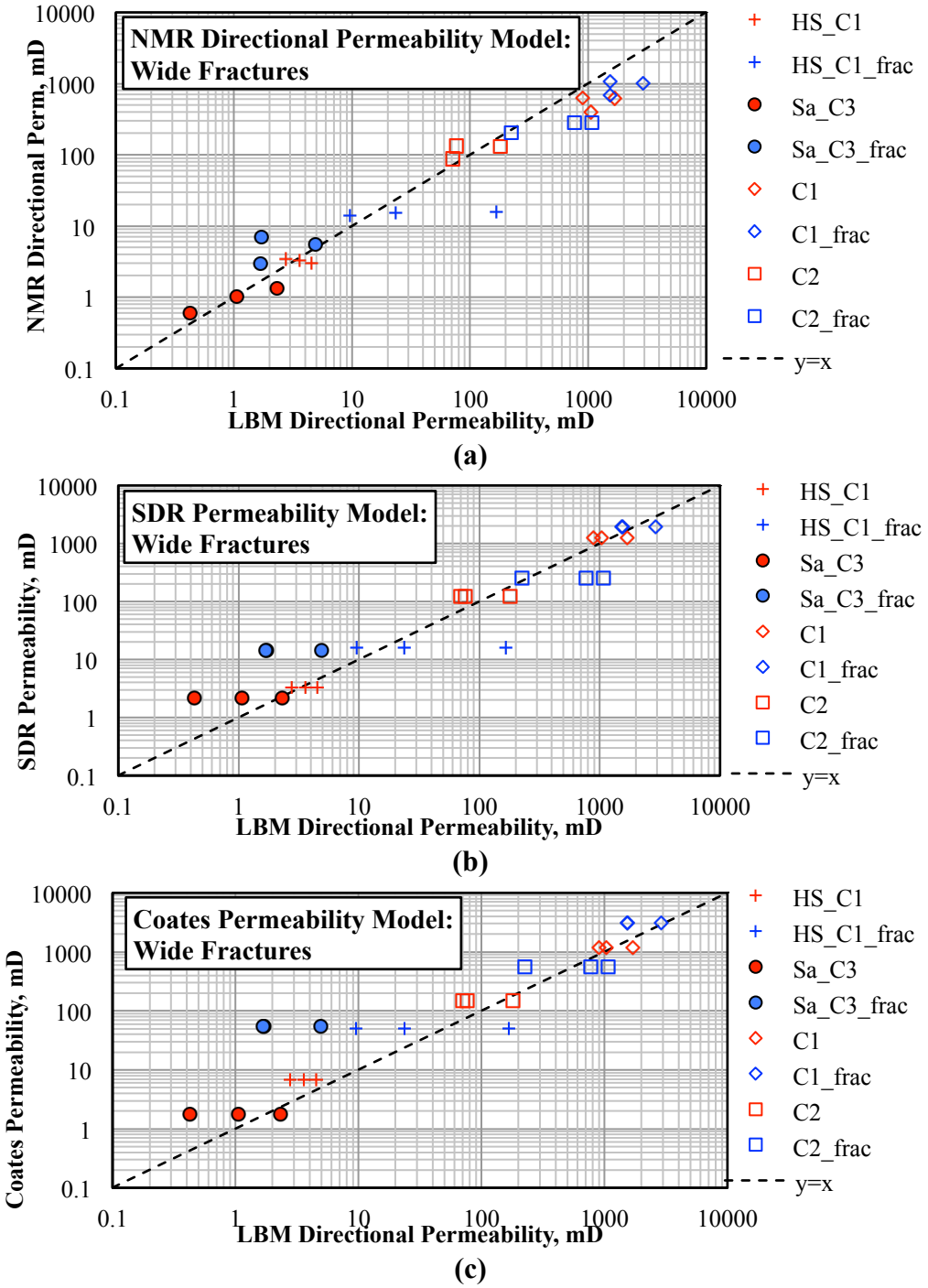

Fig. 6.3—Comparison of NMR permeability estimates against LBM permeability for the carbonate samples before and after inserting wide micro-fractures. (a) NMR directional permeability model, (b) SDR model, and (c) Coates model. For each rock sample, three data points are shown to represent the permeability in X, Y, and Z directions. The red and blue data points show the original carbonate samples and their corresponding fractured samples, respectively.

Table 6.4—Carbonate samples with planar fractures wider than pore size (i.e., wide fractures): The relative decrease of fracture T_2 from their original T_2 value, and the relative errors in permeability estimation by NMR directional permeability model, SDR model, and Coates model, compared against LBM permeability.

Matrix	Fracture T_2 Decrease, %		Error in Directional Permeability Model Estimation, %	Error in SDR Permeability Estimation, %	Error in Coates Permeability Estimation, %
HS_C1_frac	34.2	X:	45.6	67.5	414.2
		Y:	-34.6	-32.2	108.2
		Z:	-90.5	-90.4	-70.5
Sa_C3_frac	34.2	X:	305.5	737.4	3157.9
		Y:	12.6	192.5	1037.9
		Z:	74.1	749.0	3203.0
C1_frac	11.0	X:	-64.9	-31.2	7.5
		Y:	-55.4	29.0	101.4
		Z:	-30.5	29.3	101.8
C2_frac	12.2	X:	-62.7	-67.1	-27.8
		Y:	-9.2	12.2	146.5
		Z:	-73.4	-76.5	-48.3

Based on the aforementioned observations we concluded that when the fracture-pore diffusional coupling effect is significant in fractured rock samples, the SDR and NMR directional permeability models are more reliable than the Coates model. When the fracture-pore diffusional coupling is negligible, all the three models can reliably predict permeability for fractured rock samples.

6.3. Synthetic Case No.2: Carbonate Samples Containing Narrow Planar Micro-Fractures

In this section, we analyze two synthetic carbonate rock samples that contain planar micro-fractures with apertures (w) smaller than the inter-granular pore size (i.e., narrow fractures). The two original carbonate samples are denoted as C0 and C2, and

their corresponding fractured rock samples as C0_frac1, C0_frac2, and C2_frac2, respectively. The C0_frac1 sample contains 15 planar fractures with apertures of 3 μm, while C0_frac2 contains 5 planar fractures with apertures of 9 μm. The total porosity of these two fractured samples are kept almost the same, to investigate the effect of fracture aperture on NMR T_2 distribution. On the other hand, the C2_frac2 sample contains 11 planar fractures with apertures of 10.7 μm. The synthetic planar fractures in the rock samples include both primary and secondary fractures. The primary fractures are almost parallel to each other, and secondary fractures terminate at the primary fractures. **Fig. 6.4** shows the 3D micro-CT pore-scale images for all the original and fractured carbonate rock samples. **Table 6.5** lists the matrix volumes, micro-CT image resolutions, total porosity, T_{2GM} values estimated from the simulated NMR T_2 distributions, and LBM permeability from fluid flow simulations for all the carbonate rock samples.

Fig. 6.5 shows the simulated NMR T_2 distributions for all the carbonate rock samples and isolated micro-fractures. In Figures 5a and 5b, the NMR simulation results for C0_frac1 and C0_frac2 show typical characteristics of fracture-pore diffusional coupling (i.e. the slow relaxing T_2 peaks of inter-granular pores are shifted downward, while the fast relaxing T_2 peak of micro-fractures almost remains in the same location). In the case of rock sample C0_frac1, containing narrow fractures (w = 3μm), the pore T_2 is decreased by 20.8%; while for C0_frac2, the one containing wide fractures (w = 9μm), the pore T_2 is decreased by 11.0% (**Table 6.6**). The comparison of the results

obtained for C0_frac1 and C0_frac2 rock samples confirms that narrow micro-fractures can downshift the pore T_2 peak more significantly than wide micro-fractures, as shown in Chi and Heidari (2015). On the other hand, in **Fig. 6.5c**, we observed minimal fracture-pore diffusional coupling effect in C2_frac, with pore T_2 peak remaining in the same location (Table 6.6).

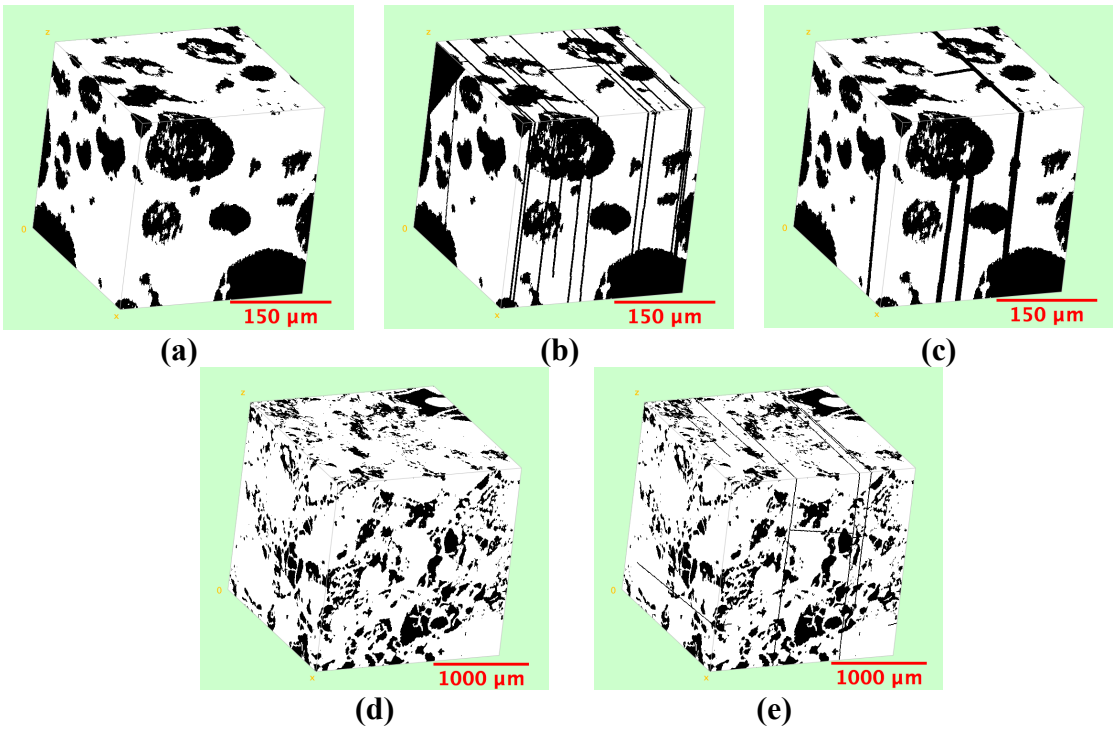

Fig. 6.4—The 3D pore-scale images of the three carbonate rock samples before and after inserting micro-fractures: (a) C0, (b) C0_frac_1 (w = 3µm, 15 fractures), (c) C0_frac_2 (w = 9µm, 5 fractures), (d) C2, and (e) C2_frac2 (w = 10.7 µm, 11 fractures). The white and black regions represent the grain and pore space, respectively.

Table 6.5—Carbonate rock samples with planar fractures narrower than pore size (i.e., narrow fractures): matrix volume, micro-CT resolutions, total porosity, estimated T_{2GM} values, and LBM permeability in three directions of the rock matrices.

Matrix	Volume, pixel^3	Resolution, μm/pixel	Porosity, %	T_{2GM}, msec	LBM Permeability, mD	
C0	300x300x300	1.000	21.98	441.4	X: Y: Z:	~0.0 ~0.0 ~0.0
C0_frac1	300x300x300	1.000	30.53	324.6	X: Y: Z:	172.6 293.8 10.8
C0_frac2	300x300x300	1.000	31.41	449.3	X: Y: Z:	923.6 991.7 307.5
C2	400x400x400	5.345	16.83	1223.0	X: Y: Z:	76.5 180.2 70.4
C2_frac2	400x400x400	5.345	19.53	1167.7	X: Y: Z:	581.4 145.1 529.9

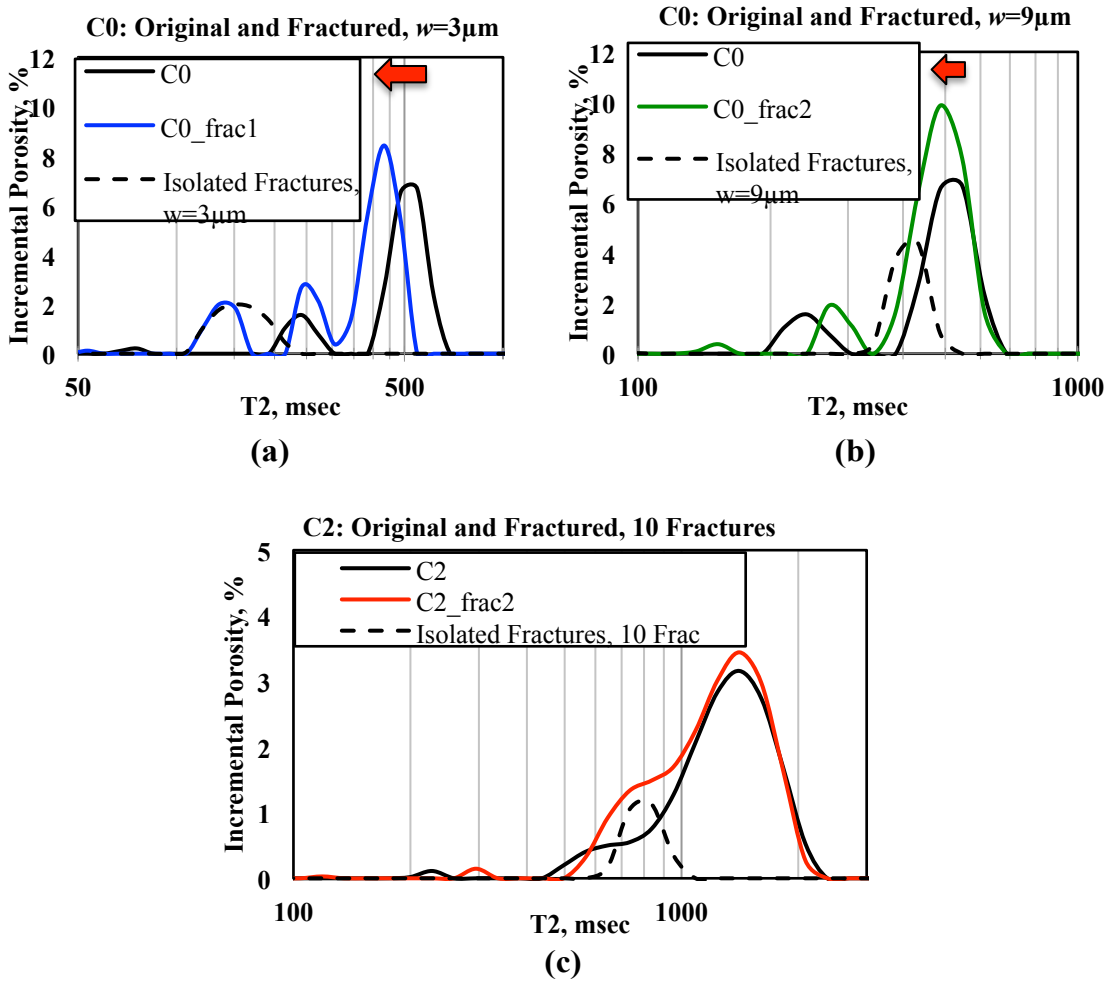

Fig. 6.5—Carbonate rock samples with planar fractures narrower than pore size (i.e., narrow fractures): The simulated NMR T_2 distribution curves for the three carbonate samples before and after inserting micro-fractures, (a) C0 and C0_frac1 (w=3µm, 15 fractures), (b) C0 and C0_frac2 (w=9µm, 5 fractures), and (c) C2 and C2_frac2 (w=10.7µm, 11 fractures). The black solid curves represent the NMR T_2 distribution for the original rock samples, the blue, green, and red solid curves show the NMR T_2 distribution for the fractured rock samples, and black dash curves represent the NMR T_2 distribution for isolated fractures, respectively.

Table 6.6—Carbonate rock samples with planar fractures narrower than pore size (i.e., narrow fractures): The relative decrease of pore T_2 from their original T_2 value, and the relative errors in permeability estimation by NMR directional permeability model, SDR model, and Coates model, compared against LBM permeability.

Matrix	Pore T_2 Decrease, %	Error in Directional Permeability Model Estimation, %		Error in SDR Permeability Estimation, %	Error in Coates Permeability Estimation, %
C0_frac1	20.8	X:	-22.2	6.0	-33.7
		Y:	-49.3	-37.7	-61.1
		Z:	453.8	1586.8	954.4
C0_frac2	11.0	X:	-79.9	-57.5	222.9
		Y:	-77.1	-60.4	200.7
		Z:	-55.5	27.8	869.9
C2_frac2	0	X:	-45.6	-65.9	-79.9
		Y:	54.8	36.6	-19.7
		Z:	-38.8	-62.6	-78.0

We used the same NMR directional permeability model parameters from previous work (Chi and Heidari 2015b), as listed in Table 5.5 in Section 5, to predict the directional permeability for the fractured rock samples, C0_frac1, C0_frac2, and C2_frac2. **Tables 6.7** and **6.8** list the parameters in the SDR and Coates model calibrated for each rock type, from which we predict permeability for fractured rock samples. The carbonate sample C0 has almost zero permeability, so there is no calibrated model parameter for C0.

Table 6.7—Carbonate rock samples with planar fractures narrower than pore size (i.e., narrow fractures): The assumed *C* parameters in SDR model adjusted for each rock sample and the permeability estimates from SDR model.

Matrix	Parameter *C*	SDR Permeability, mD
C0_frac1	0.002	183.0
C0_frac2	0.002	392.9
C2	0.001	120.0
C2_frac2	0.001	198.3

Table 6.8—Carbonate rock samples with planar fractures narrower than pore size (i.e., narrow fractures): The assumed $T_{2\text{cutoff}}$ values in Coates model adjusted for each rock sample and the permeability estimates from Coates model.

Matrix	$T_{2cutoff}$, msec	Coates Permeability, mD
C0_frac1	385.4	114.4
C0_frac2	385.4	2982.0
C2	954.1	147.1
C2_frac2	954.1	116.6

Fig. 6.6 shows the NMR permeability estimates from the three models compared against LBM permeability for all the carbonate samples before and after inserting narrow planar micro-fractures. The NMR directional permeability model (**Fig. 6.6a**) predicts anisotropic rock permeability in three directions, while the SDR and Coates models (**Figs. 6.6b** and **6.6c**) are not capable to do so. Table 6.6 lists the relative decrease of pore T_2 from their original values, and the relative errors in permeability estimates by the three models compared against the permeability estimated from LBM method. In the rock samples experiencing significant fracture-pore coupling effect (i.e. C0_frac1 and C0_frac2), both the NMR directional permeability model and the SDR model predict the permeability satisfactorily, while the Coates model significantly overestimates the permeability of C0_frac2 by 200%-870% (Table 6.6). On the other hand, for the rock samples showing minimal fracture-pore coupling effect (i.e. C2_frac2) all three permeability models predict the rock permeability with similar errors, but the SDR and NMR directional permeability models are slightly better than the Coates model (Table 6.6). These observations further confirm the conclusion from the previous section, i.e. the SDR and NMR directional permeability models are more reliable than the Coates model when fracture-pore diffusional coupling effect is significant.

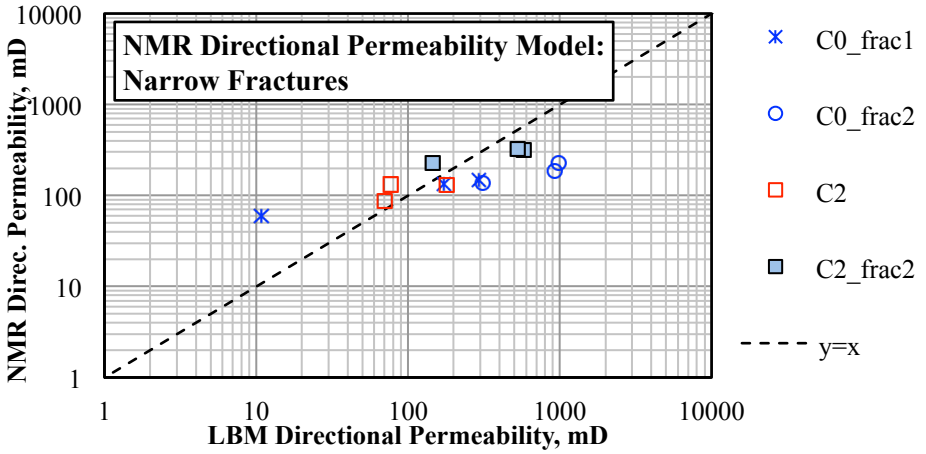

(a)

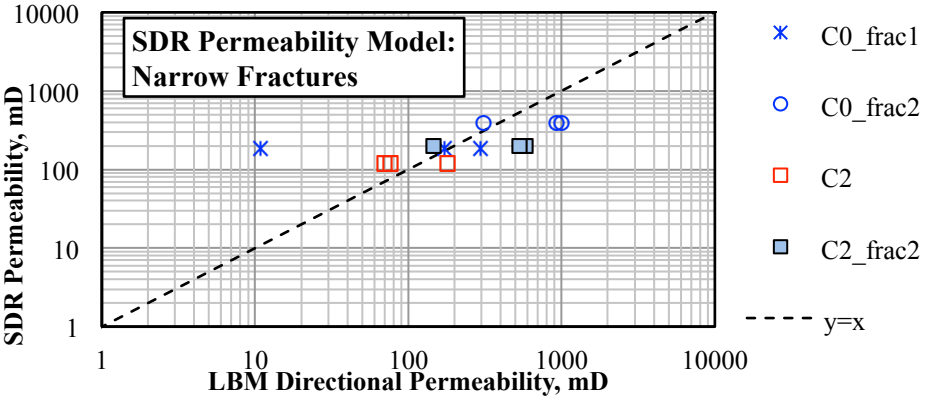

(b)

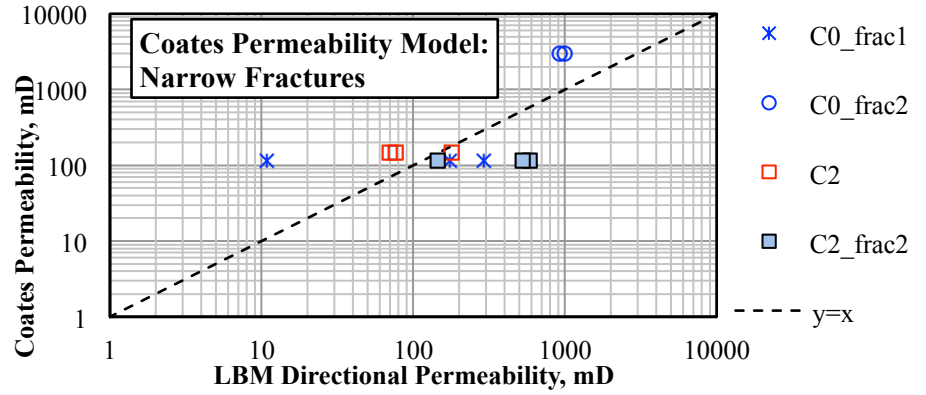

(c)

Fig. 6.6—Comparison of NMR permeability estimates against LBM permeability for the carbonate samples before and after inserting narrow micro-fractures: (a) NMR directional permeability model, (b) SDR model, and (c) Coates model. For each rock sample, three data points are shown to represent the permeability in X, Y, and Z directions. The red and blue data points show the original carbonate samples and their corresponding fractured samples, respectively.

6.4. Conclusions

Fracture-pore diffusional coupling affects NMR T_2 distribution of fractured rock samples to different extents, depending on the relative size of micro-fractures and pores, and the volumetric concentration of micro-fractures. We demonstrated that the fracture-pore diffusional coupling effect can also impact NMR permeability assessment in fractured formations. We showed that, in the case of carbonate rock samples experiencing significant fracture-pore diffusional coupling effect, the SDR and NMR directional permeability models estimate rock permeability within one order of magnitude of error, but the Coates model can overestimate or underestimate permeability by up to two orders of magnitude. Therefore, we concluded that the SDR and NMR directional permeability models are more reliable than the Coates model when fracture-pore diffusional coupling is significant. In the case of rock samples experiencing minimal fracture-pore diffusional coupling effect, all three models can predict permeability for fractured rock samples with similar accuracy.

The outcomes of this research enable improved permeability assessment in formations with complex pore structure, such as tight carbonate and organic-rich mudrock formations containing natural and induced micro-fractures. The improved NMR permeability assessment in fractured formations enhances reservoir characterization, and can significantly improve the production from tight carbonate and organic-rich mudrock formations.

7. NMR TWO-PHASE SIMULATIONS IN ORGANIC-RICH MUDROCKS

Interpretation of NMR relaxometry in organic-rich mudrocks still remains a challenge for petrophysicists. A reliable numerical simulation of NMR response in these rocks helps in better understanding of the NMR relaxometry data and the corresponding petrophysical properties, e.g., the wettability and fluid distribution in the pore space. The hydrocarbon-wetting or mixed-wetting characteristics of organic-rich mudrocks have significant impacts on hydrocarbon recovery from the rocks, but quantification of wettability using conventional well-log interpretation methods remains a conundrum. The objectives of this section are to (a) introduce an NMR two-phase simulation method to model the NMR responses in organic-rich mudrocks and (b) investigate the effects of wettability alteration and fluid distribution on NMR relaxometry using numerical simulations.

7.1. Introduction

NMR relaxometry has proved its successful application in conventional reservoirs. In recent years, due to the high demand in developing oil and gas production in unconventional reservoirs, there have been uprising interests in applying the NMR technique in unconventional reservoirs such as tight-gas-sand (Xiao et al. 2013) and organic-rich mudrock formations (Singer et al. 2013; Smith et al. 2013).

In organic-rich mudrocks, it has been observed that there are two types of pores, i.e. the organic pores inside the kerogen, and the inorganic pores in the rock matrix (Loucks et al. 2012). Due to the nano-scale size of the pores, various NMR experiments have shown T_2 distribution in organic-rich mudrocks spanning the short T_2 range of less than 1 msec (Odusina et al. 2011; Kausik et al. 2011; Cao Minh et al. 2012; Sulucarnain et al. 2012; Rylander et al. 2013; Jiang et al. 2013; Washburn and Birdwell 2013a). NMR detects the magnetic signals from all the hydrogen nuclei in the fluids including both water and hydrocarbon phases, and the water and hydrocarbon signals largely overlap on the measured NMR T_2 distribution. Generally, it has been challenging to separate the water signal from the hydrocarbon signal in NMR T_2 distribution. Sigal and Odusina (2011) proposed a laboratory method to determine the pore size distributions for the pores containing methane in Barnett cores, and later showed that the methane-saturated pores in these core plugs ranged from 1 to 100 nm, and 20-40% of the pore volume was in pores smaller than 10 nm (Sigal 2015). On the other hand, the water phase in organic-rich mudrocks was observed mostly as clay-bound water (Passey et al. 2010; Sigal and Odusina 2011). Because of the small dimensons of both organic and inorganic pores, the diffusion-induced relaxation in both hydrocarbon and water phases has been supposed to be significantly suppressed in organic-rich mudrocks and therefore can be ignored (Sigal and Odusina 2011; Washburn 2014).

It is also generally accepted that the organic pores in kerogen are hydrocarbon-wet, and the inorganic pores are water-wet (Passey et al. 2010; Sigal and Odusina

2011). The hydrocarbon-wetting or mixed-wetting characteristics of organic pores reduce the hydrocarbon relaxation times significantly, which makes conventional interpretation techniques unreliable in organic-rich mudrocks (Chen et al. 2013; Odusina et al. 2011). Furthermore, the existence of hydrogen-bearing constituents, such as bitumen and kerogen in some immature organic-rich mudrock samples, might also generate NMR signals in the measurements (Washburn and Birdwell 2013b). All these factors complicate the interpretation of NMR measurements in organic-rich mudrocks.

The NMR responses in organic-rich mudrocks, which reflect signals from both water and hydrocarbon phases, have not been investigated by pore-scale simulations due to the complex pore structure of organic-rich mudrocks. We improved the previously developed and tested single-phase NMR simulator (Chi and Heidari 2014a, 2014b, 2015; Chi et al. 2014; Talabi, 2009) to model the two-phase NMR relaxometry in organic-rich mudrocks. We treated the hydrocarbon as one phase without differentiating gas and oil, because previous publications indicate that the hydrocarbon in the nano-sized organic pores in gas shale might be stored as liquid rather than absorbed/free gas, due to a physical phenomenon called capillary condensation (Chen et al. 2012; Zhang et al. 2012). By simultaneously simulating the NMR signals from hydrocarbon and water phases, we aim to study the effect of wettability alteration and fluid distribution on NMR relaxometry in organic-rich mudrocks

7.2. Two-Phase NMR Simulation Method

This section describes the modified random-walk algorithm used in the two-phase NMR simulation method.

Our single-phase NMR simulator, which was adapted from Talabi's (2009) work, has been proved successful in improving the interpretation of NMR relaxometry in single-phase fluid bearing rock samples (Chi and Heidari 2014a, 2014b, 2015). In the original random-walk algorithm for single-phase NMR simulations (Talabi et al. 2008; Talabi 2009), random walkers are assigned to all void pixels, and the step time Δt of each walking step is given by

$$\Delta t = \frac{s^2}{6D}, \tag{7-1}$$

where s is the distance of each walking step, and D is the diffusional coefficient of the fluid. The walking step distance s is calculated by 0.2 times of the resolution of the input micro-CT images, to ensure that the walker takes significant amount of steps before it collides on a surface (Talabi 2009). When a walker encounters a solid surface, there is a probability that it is killed by the collision on the solid surface. The death probability, δ, of the walker, is given by

$$\delta = \frac{2\rho s}{3D}, \tag{7-2}$$

where ρ is the surface relaxivity of the solid grains. If the walker survives after collision on the solid surface, it bounces back to the pore space. The transverse magnetization

decay caused by surface relaxation is therefore calculated by the fraction of alive walkers, *P(t)*, given by

$$\left.\frac{M(t)}{M_0}\right|_{surface} = P(t) = \frac{N(t)}{N_0}, \tag{7-3}$$

where *M(t)* is the transverse magnetization at time *t*, M_0 is the initial transverse magnetization at time zero, *N(t)* is the number of alive walkers at time *t*, and N_0 is the initial number of total walkers.

In our two-phase NMR simulation method, we consider two types of fluids, water and hydrocarbon, which have different diffusional coefficients. In this dissertation, we adopted the diffusional coefficient of 2.07×10^{-9} m^2/sec for water (Talabi 2008), and 1.50×10^{-9} m^2/sec for hydrocarbon (Cussler 1997), as denoted in Fig. 2.2. Consequently, the walkers representing each type of fluid have different walking step distances. On the other hand, the fluids in organic-rich mudrocks encounter two types of solid surfaces, i.e. the inorganic surface of mineral grains, and the organic surface of kerogen. The NMR surface relaxivities of the two types of surfaces are distinct, i.e. 10 to 46 μm/sec for the inorganic surfaces (Talabi 2009), and 3.8 to 5 μm/sec for organic surfaces (Jiang et al. 2013). We assumed a NMR surface relaxivity value of 15 μm/sec for inorganic surfaces, and 5 μm/sec for organic surfaces, respectively (Fig. 2.2). Therefore the death probabilities of walkers colliding on the two types of solid surface are also distinct. Although Fig. 2.2 illustrates a complete separation of organic and inorganic pores, there is a high chance that both fluid phases contact both types of solid

surfaces. Therefore, there are four scenarios for the relaxation process in organic-rich mudrocks: water relaxing on inorganic surfaces, water relaxing on organic surfaces, hydrocarbon relaxing on inorganic surfaces, and hydrocarbon relaxing on organic surfaces. Determining the types of fluids and the types of solid surfaces for each random walker is thereby crucial to the random walking and collision processes in the two-phase NMR simulation.

In the input data matrix representing an organic-rich mudrock sample, we used 0s for water phase, 1s for inorganic grains, 2s for hydrocarbon phase, and 3s for kerogen. After assigning walkers in the void pixels (i.e., 0s and 2s), their walking step is determined by their diffusional coefficients via Equation (7-1). Then, when the walker proceeds to a solid pixel, either 1 or 3, the death probability is determined by their different surface relaxivity via Equation (7-2). At each time point, the fraction of alive walkers is calculated to show the normalized magnetization decay. By this means, the NMR signals from both water and hydrocarbon phases, which relax on two types of surfaces, are simulated simultaneously.

In addition to the surface relaxation, which is modeled by the random-walking process described above, we also considered different bulk relaxation times for the two types of fluids. We set the bulk relaxation times as 3.1 sec for water, and 0.62 sec for hydrocarbon in the simulations (Talabi 2009). Then the effective bulk relaxation time $T_{2B,eff}$ is given by the weighted average of the two bulk relaxation times,

$$\frac{1}{T_{2B,eff}} = \frac{\chi_w}{T_{2B,w}} + \frac{\chi_{hc}}{T_{2B,hc}}, \tag{7-4}$$

where $T_{2B,w}$ is the bulk relaxation time of water, $T_{2B,hc}$ is the bulk relaxation time of hydrocarbon, χ_w is the volume ratio of water in all fluids, and χ_{hc} is the volume ratio of hydrocarbon in all fluids. Then the magnetization decay caused by bulk relaxation is given by an exponential decay with characteristic time of $T_{2B,eff}$,

$$\left.\frac{M(t)}{M_0}\right|_{bulk} = \exp(-\frac{1}{T_{2B,eff}}). \tag{7-5}$$

At last, the total transverse magnetization decay in the two-phase NMR simlator is modeled by multiplying the exponential decay of bulk relaxation and the multi-exponential decay of surface relaxation. We assumed zero diffusion-induced relaxation in our simulations (Sigal and Odusina 2011; Washburn 2014). Therefore the total transverse magnetization decay is given by

$$\frac{M(t)}{M_0} = \frac{N(t)}{N_0} \cdot \exp(-\frac{1}{T_{2B,eff}}). \tag{7-6}$$

To speed up the simulation process, we parallelized the random-walk computation in the NMR two-phase simulator. The original NMR simulator updates the walker position and status sequentially at each time point, i.e. one walker by one walker. However, the random walkers are independent from and have no interactions with each other, we can group them into a certain number of groups and assign each

group to a computing thread. The positions of walkers and the fraction of alive walkers are thus checked and calculated in each computing thread simultaneously, instead of sequentially. The parallelized algorithm of simulator can accelerate the NMR simulation process significantly, depending on the number of computing threads used.

7.3. Pore-scale Rock Matrices of Organic-rich Mudrock Samples

First, we synthetically created an organic-rich mudrock matrix containing water in inorganic pores and hydrocarbon in organic pores to mimic a real organic-rich mudrock sample. In the data matrix we used 0 to represent water, 1 for inorganic minerals, 2 for organic pores, and 3 for kerogen, respectively. The synthetic organic-rich mudrock matrix has a volume of 300x300x300 $pixel^3$, and an assumed image resolution of 10 nm/pixel (**Fig. 7.1**). This synthetic organic-rich mudrock matrix serves as an input file for our two-phase NMR numerical simulations.

In addition to the synthetic organic-rich mudrock matrix, two actual organic-rich mudrock samples, named Sample A and Sample B, were scanned by an FIB-SEM equipment. The FIB-SEM image resolution is 7.487 nm/pixel for Sample A and 4.863 nm/pixel for Sample B, respectively. And the vertical resolution, i.e. the distances between two adjacent images, is 10 nm/pixel for both samples. After interpolating the FIB-SEM images using Fiji, the imaging resolution is uniform in different directions for each sample, i.e. 7.487 nm/pixel for Sample A and 4.863 nm/pixel for Sample B, respectively. Then we used Fiji to perform trainable segmentation on the grey-scale

FIB-SEM images to convert them into four-colored images, as described in Section 2.1, Section 2. The comparison of original grey-scale FIB-SEM images and the color images after segmentation is shown in **Figs. 7.2** (Sample A) and **7.3** (Sample B). Then we cropped the image stacks into cubic shape, as shown in **Figs. 7.4** (Sample A) and **7.5** (Sample B). The cubic rock matrices have a volume of 584x584x584 pixel^3 for Sample A, and 694x694x694 pixel^3 for Sample B, respectively. At last, we converted the cubic stack of images to a data matrix (i.e., 0 for water, 1 for inorganic minerals, 2 for organic pores, and 3 for kerogen, respectively), to serve as the input file for two-phase NMR numerical simulations.

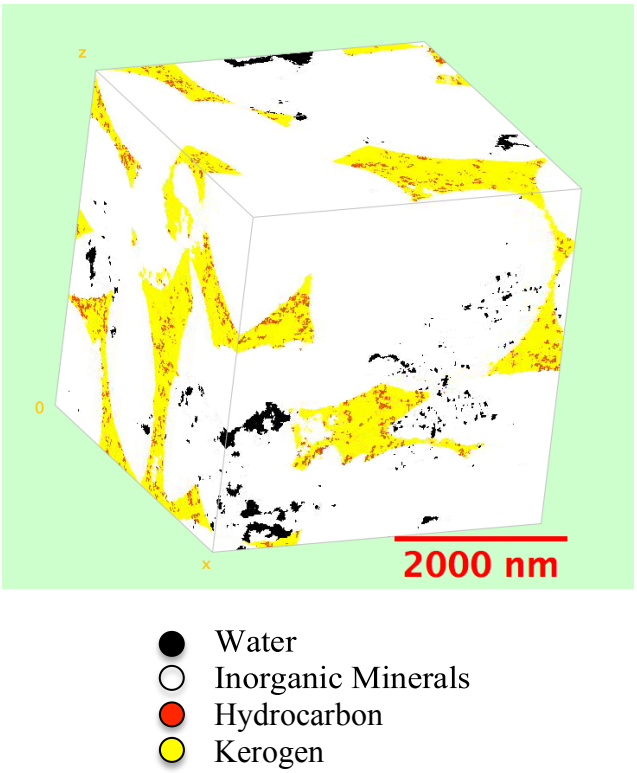

Fig. 7.1—The 3D pore-scale image for the synthetic organic-rich mudrock matrix. The black, white, red, and yellow regions stand for the water, inorganic minerals, hydrocarbon, and kerogen, respectively.

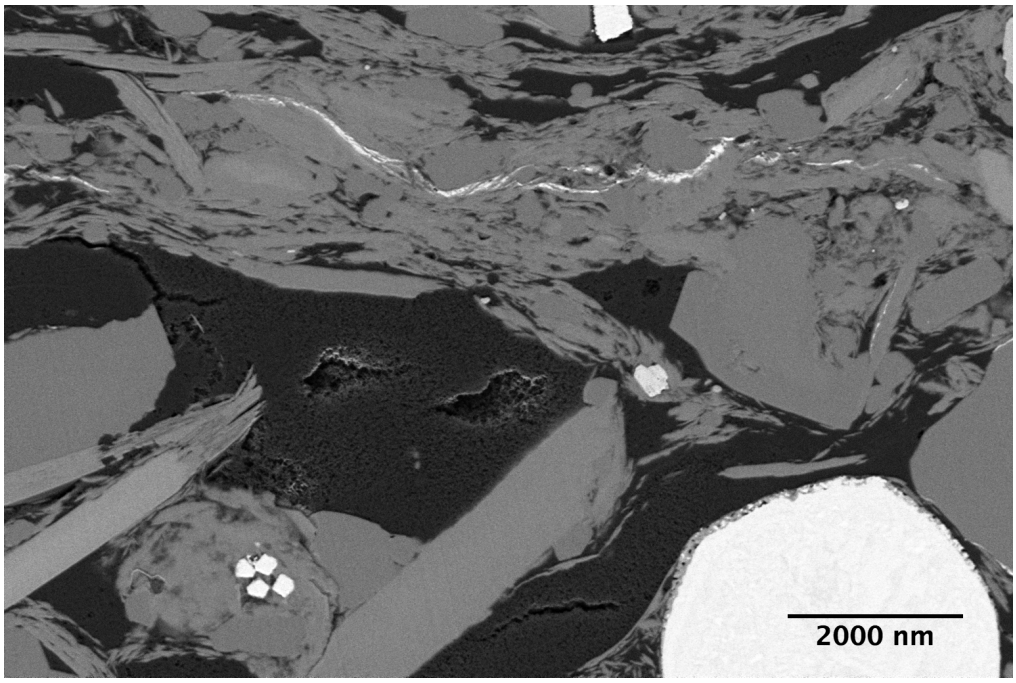

(a)

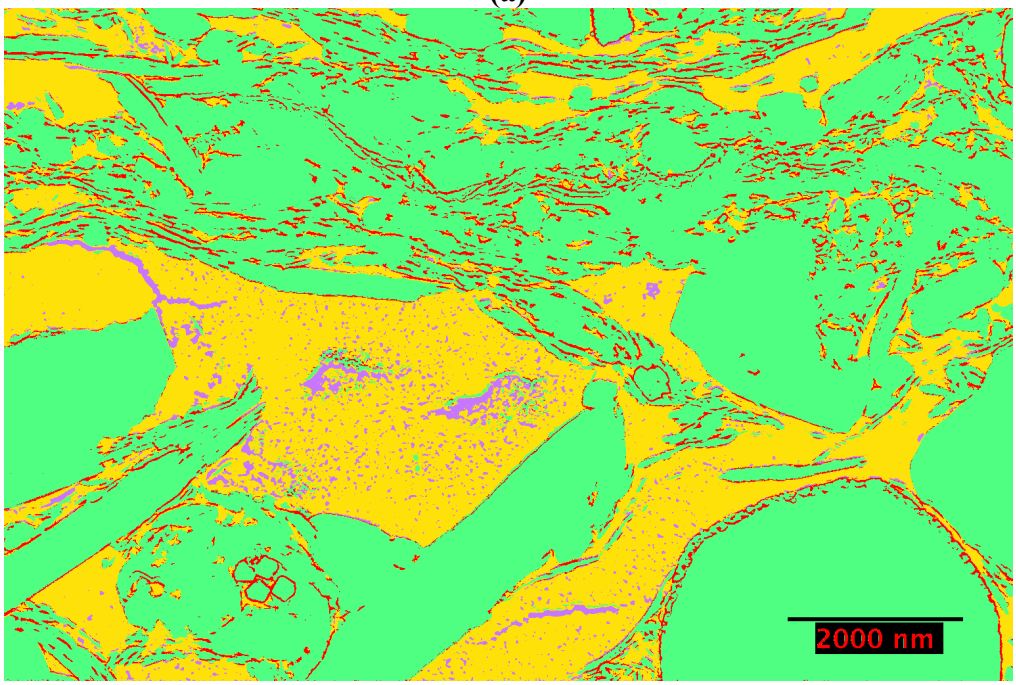

(b)

Fig. 7.2—Segmentation of FIB-SEM images of organic-rich mudrock Sample A. (a) The original grey-scale FIB-SEM image of Sample A, and (b) the four-color image obtained by Fiji trainable segmentation. The red, green, purple, and yellow stand for the water, inorganic minerals, organic pores, and kerogen regions, respectively.

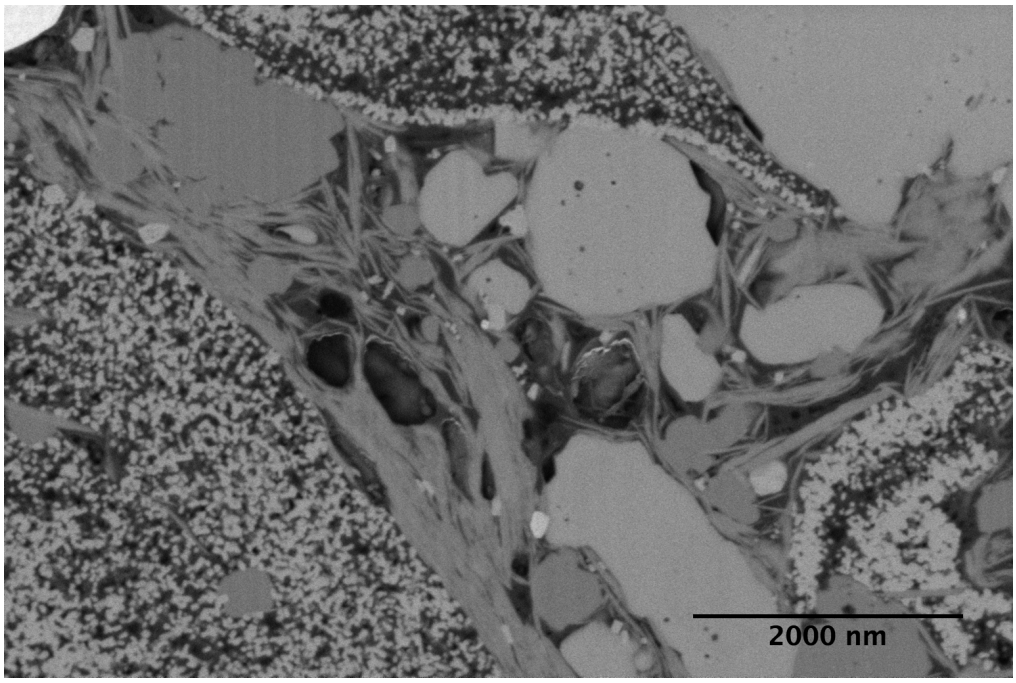

(a)

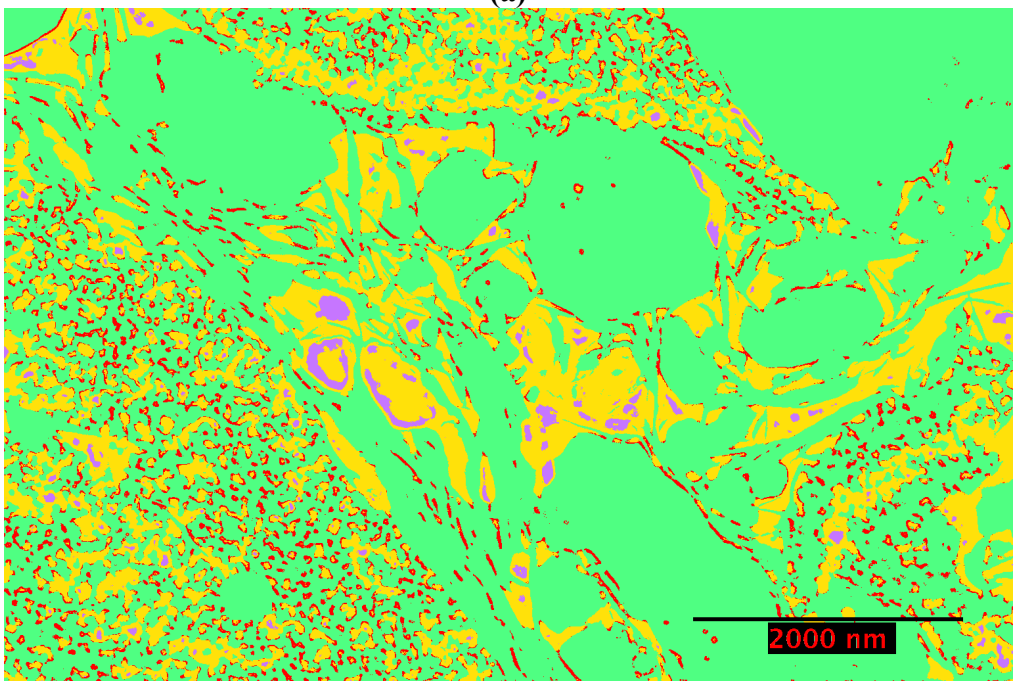

(b)

Fig. 7.3—Segmentation of FIB-SEM images of organic-rich mudrock Sample B. (a) the original grey-scale FIB-SEM image of Sample B, and (b) the four-color image obtained by Fiji trainable segmentation. The red, green, purple, and yellow regions stand for the water, inorganic minerals, organic pores, and kerogen, respectively.

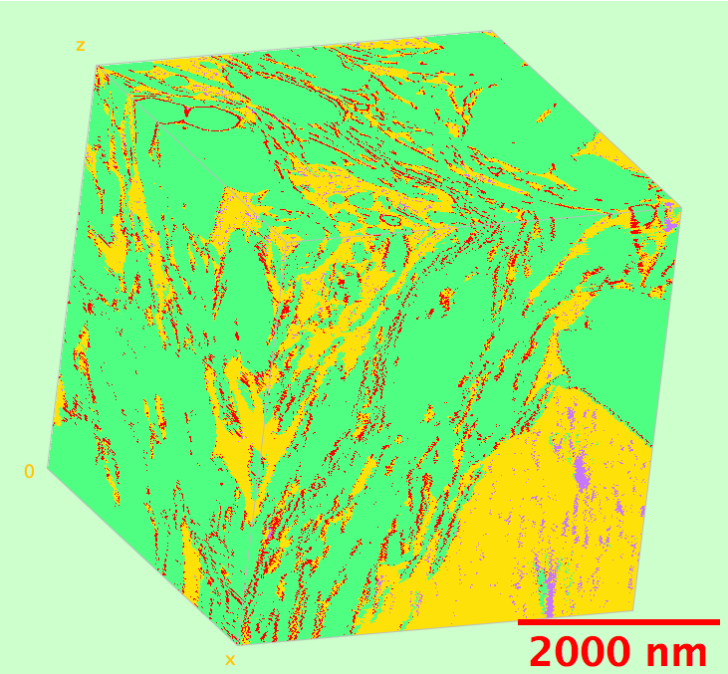

Fig. 7.4—The 3D rock matrix representing the organic-rich mudrock Sample A. The red, green, purple, and yellow regions stand for the water, inorganic minerals, hydrocarbon pores, and kerogen, respectively.

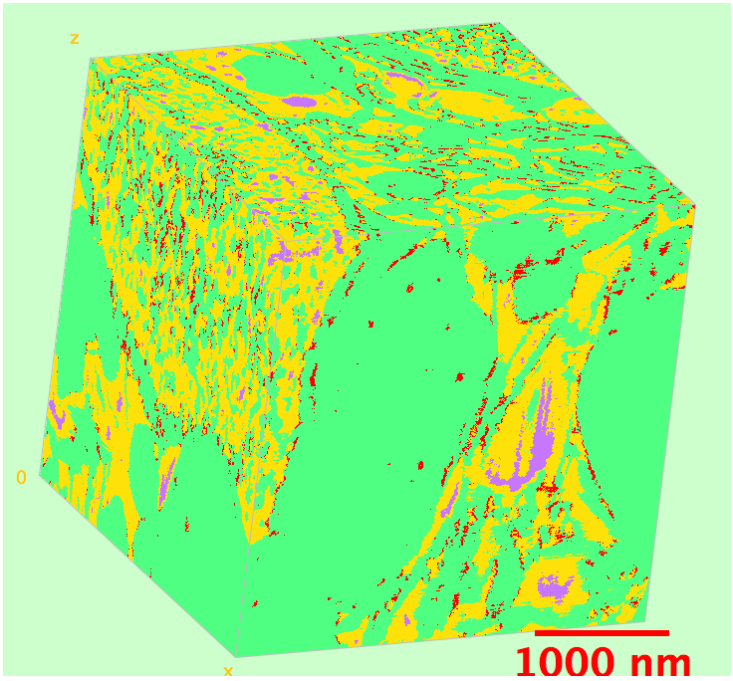

Fig. 7.5—The 3D rock matrix representing the organic-rich mudrock Sample B. The red, green, purple, and yellow regions stand for the water, inorganic minerals, organic pores, and kerogen, respectively.

Table 7.1—Synthetic organic-rich mudrock sample: the total porosity, organic porosity, inorganic porosity, and matrix volume of the sample.

Matrix	Total Porosity, %	Organic Porosity, %	Inorganic Porosity, %	Matrix Volume, pixel^3
Synthetic Organic Mudrock	3.73	2.61	1.12	300x300x300

7.4. NMR Two-Phase Simulation Results

7.4.1 Synthetic Organic-rich Mudrock Matrix

First, we simulated the total NMR response from both the water and hydrocarbon phases in the synthetic organic-rich mudrock matrix, then we simulated the NMR response from each phase individually, to compare against the total NMR response. **Table 7.1** lists the total porosity, organic porosity, inorganic porosity, and matrix volume of the synthetic organic-rich mudrock sample. **Fig. 7.6a** shows the simulated NMR T_2 distribution of the synthetic organic-rich mudrock sample, containing only water phase (blue), only hydrocarbon phase (red), and both phases (black curve). The T_2 distribution shows that the water phase relaxes slightly faster than the hydrocarbon phase, which is mainly due to the fact that the surface relaxivity for water in inorganic pores (15 μm/sec) is higher than that for hydrocarbon phase in organic pores (5 μm/sec). When both phases are simulated simultaneously, the total T_2 distribution of the synthetic organic-rich mudrock matrix (Fig. 7.6a black curve) exactly overlaps both the T_2 peaks of water and hydrocarbon phases. This demonstrates that our two-phase simulation method is reflecting NMR responses from both phases. Furthermore, we compared the transverse magnetization decay curves for two-phase simulation and sum of individual phases, as shown in **Fig. 7.6b**. The total transverse magnetization decay from two-phase NMR simulation (black solid line) exactly matches the sum of individual decay curves from water and hydrocarbon phases (red dash line).

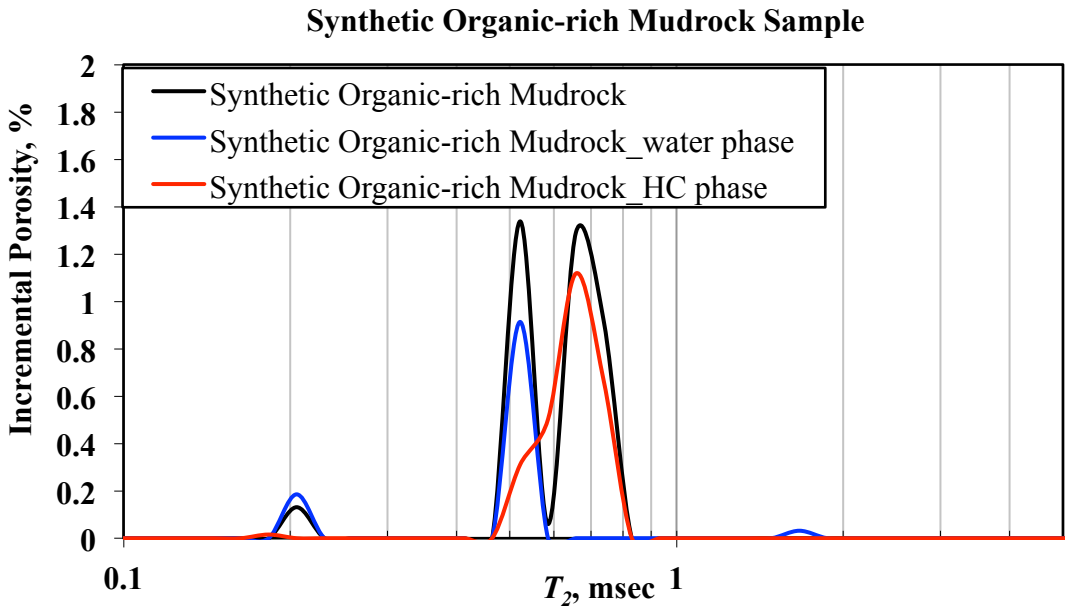

(a)

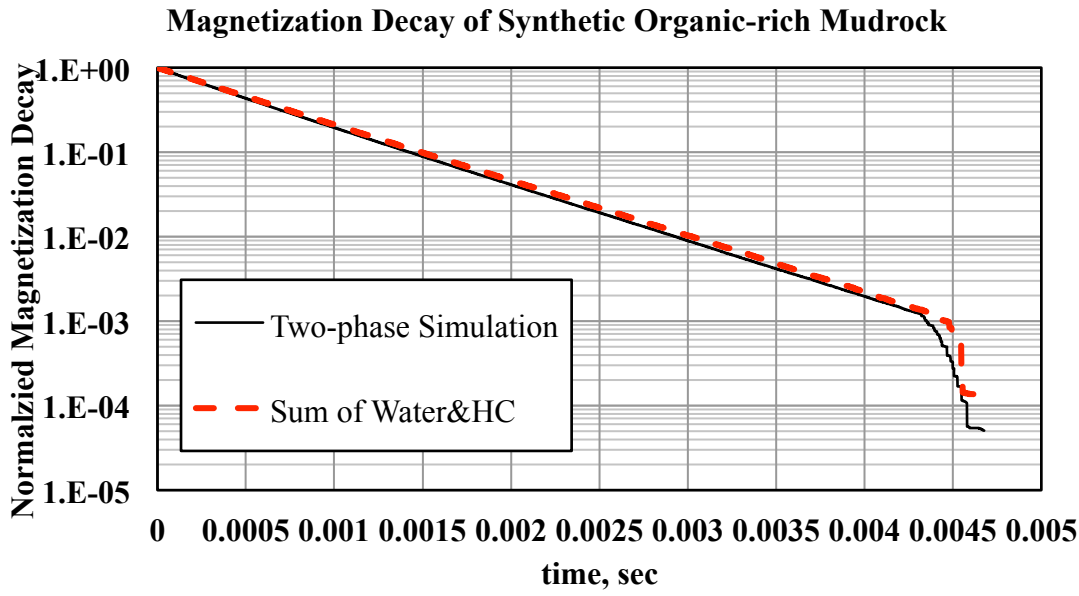

(b)

Fig. 7.6—Synthetic organic-rich mudrock matrix: (a) The estimated T_2 distribution of water phase in inorganic pores (blue), hydrocarbon phase in organic pores (red), and both phases in the whole rock (black curve). The area under each T_2 distribution curve represents the corresponding porosity. (b) The simulated transverse magnetization decay of the synthetic organic-rich mudrock sample, by two-phase NMR simulation (black solid curve) and by sum of individual signals from inorganic and organic pores (red dash curve).

To investigate the influence of wettability alteration on NMR relaxometry in organic-rich mudrocks, we changed the wettability of inorganic pores in the synthetic organic-rich mudrock matrix from water-wet to hydrocarbon-wet, as shown in **Fig. 7.7**. In **Fig. 7.7a** only those inorganic pores connecting to kerogen experience wettability change from water-wet to hydrocarbon-wet, and in **Fig. 7.7b** all the inorganic pores do. The inorganic pores that become hydrocarbon-wet contain a thin layer of hydrocarbon on the surface of pore walls, and water phase remains in the middle of pores.

Fig. 7.8 shows the simulated NMR T_2 distribution of the organic-rich mudrock matrix before (black) and after wettability change from water-wet to hydrocarbon-wet (green curve). **Figs. 7.8a** and **7.8b** show the cases of partial wettability change and whole-rock wettability change, respectively. The comparison of T_2 distributions indicates that the original fast-relaxing water signal shifts upwards and almost merges with the slow-relaxing hydrocarbon signal. This observation can be explained by the fact that the water phase in the inorganic pores is not contacting the pore wall, thus its relaxation becomes much slower. Meanwhile, a fast-relaxing T_2 peak appears at 0.4 msec, which can be related to the thin layer of hydrocarbon on the inorganic pore surface. These influences on T_2 distribution become more obvious when the whole mudrock changes to hydrocarbon-wet, as shown in **Figs. 7.7b** and **7.8b**. These observations indicate that the wettability alteration can evidently influence the NMR relaxometry in organic-rich mudrocks.

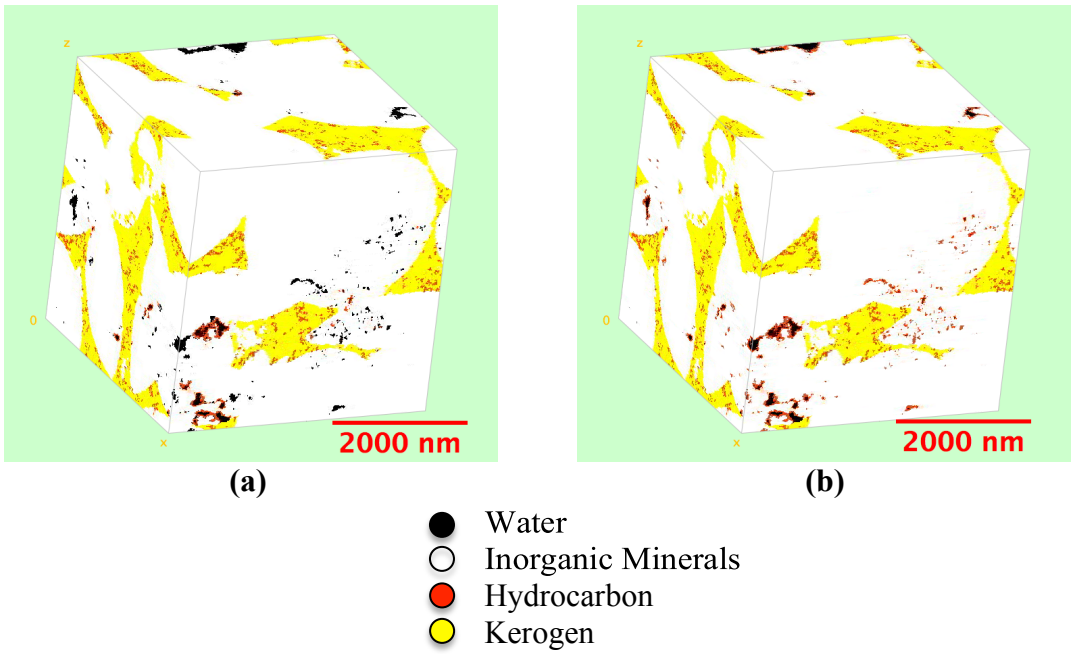

Fig. 7.7—Synthetic organic-rich mudrock matrix: The 3D pore-scale image for the mudrock matrix with inorganic pores changed to hydrocarbon-wet. (a) Only the inorganics pores connecting to kerogen change wettability; and (b) all the inorganic pores change wettability. The inorganic pores that changed wettability contain a thin layer of hydrocarbon on the wall surface, and water phase in the middle. The black, white, red, and yellow regions represent water, inorganic minerals, hydrocarbon, and kerogen, respectively.

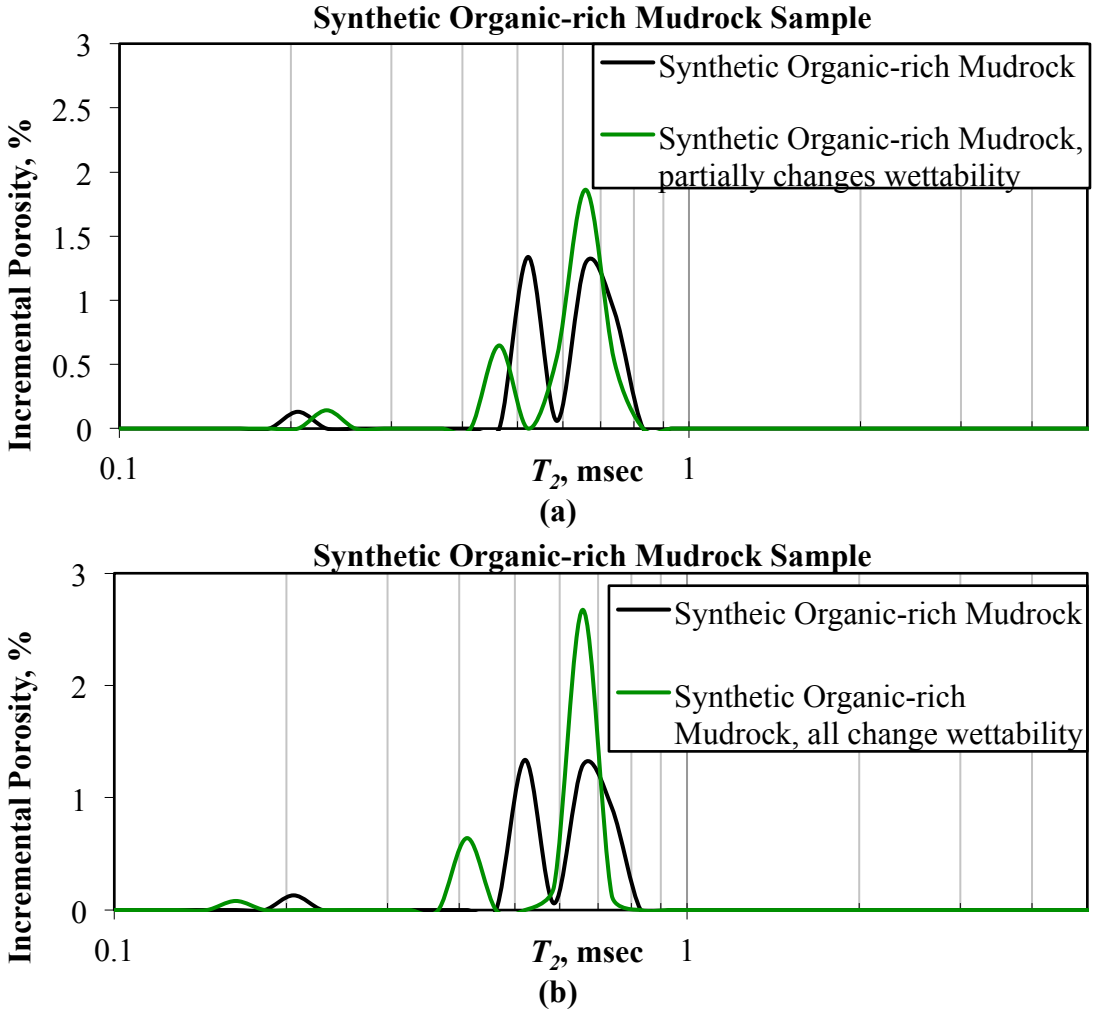

Fig. 7.8—Synthetic organic-rich mudrock matrix: The simulated T_2 distributions of the mudrock matrix with (a) only the inorganics pores connecting to kerogen change to hydrocarbon-wet; and (b) all the inorganic pores change to hydrocarbon-wet. Black and green curves represent the T_2 distributions of the original rock matrix, and the rock matrix after wettability change, respectively.

7.4.2 Organic-rich Mudrock Sample A

The total NMR response from both water and hydrocarbon phases in Sample A is simulated simultaneously using our two-phase NMR simulator. Due to the large matrix size of Sample A, we divided this sample into eight subsamples, named as A-1, A-2, … and A-8, and simulated NMR responses in each of them. **Table 7.2** lists the total porosity, organic porosity, inorganic porosity, and matrix volume of Sample A and its eight subsamples. From the porosity values it is observed that Sample A is highly inhomogeneous in the spatial distribution of organic and inorganic pores. For example, the subsample A-1 has higher inorganic porosity than organic porosity, and vice versa for subsample A-2. **Fig. 7.9** shows the simulated T_2 distributions for all eight subsamples of Sample A, and the area under each T_2 distribution curve reflects the inorganic and organic porosities of the corresponding subsample. This result demonstrates that the pore size distributions and porosities of the eight subsamples are highly inhomogeneous. To simulate the total NMR response in the whole organic-rich mudrock Sample A, we combined the transverse magnetization decays from all 8 subsamples to calculate the total transverse magnetization decay, then we estimated the total NMR T_2 distribution in Sample A by T_2 inversion. **Fig. 7.10** show the total magnetization decay from all 8 subsamples, and the total NMR T_2 distribution in organic-rich mudrock Sample A, respectively. **Fig. 7.11** shows the simulated NMR T_2 distribution curves of Sample A containing only water phase (blue), only hydrocarbon phase (red), and both phases (black curve). It shows that the NMR T_2 distribution of Sample A captures the feature of both water and hydrocarbon signals.

Table 7.2—Organic-rich mudrock Sample A: the total porosity, organic porosity, inorganic porosity, and matrix volume of the sample and its eight subsamples.

Matrix	Total Porosity, %	Organic Porosity, %	Inorganic Porosity, %	Matrix Volume, pixel^3
Sample A	8.60	3.35	5.26	584x584x584
Subsample A-1	6.51	1.64	4.87	292x292x292
Subsample A-2	10.39	6.09	4.30	292x292x292
Subsample A-3	9.33	1.04	8.29	292x292x292
Subsample A-4	7.53	0.72	6.81	292x292x292
Subsample A-5	8.33	0.70	7.63	292x292x292
Subsample A-6	8.00	2.48	5.52	292x292x292
Subsample A-7	10.92	9.94	0.97	292x292x292
Subsample A-8	7.81	4.16	3.65	292x292x292

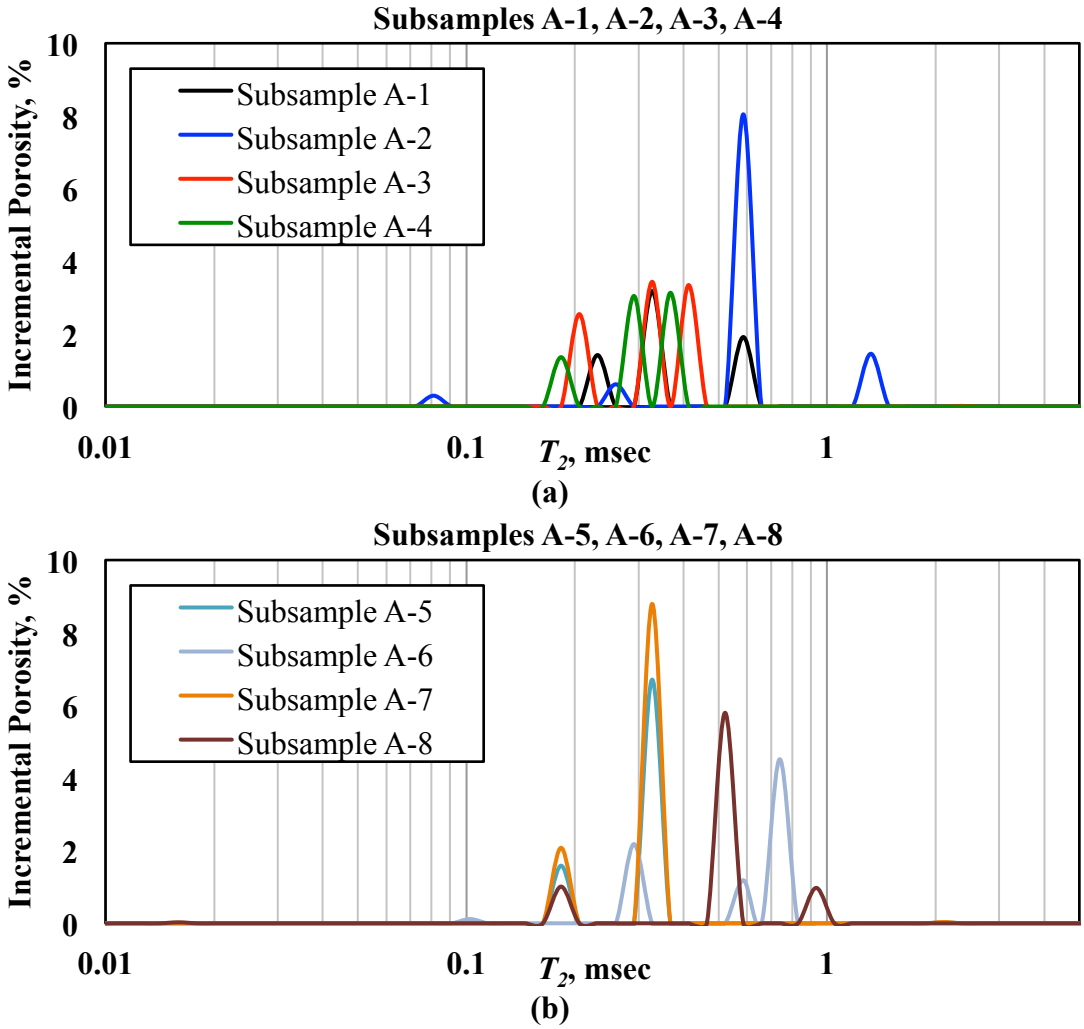

Fig. 7.9—Organic-rich mudrock Sample A: the simulated T_2 distributions of (a) subsamples A-1, A-2, A-3, A-4, and (b) subsamples A-5, A-6, A-7, and A-8.

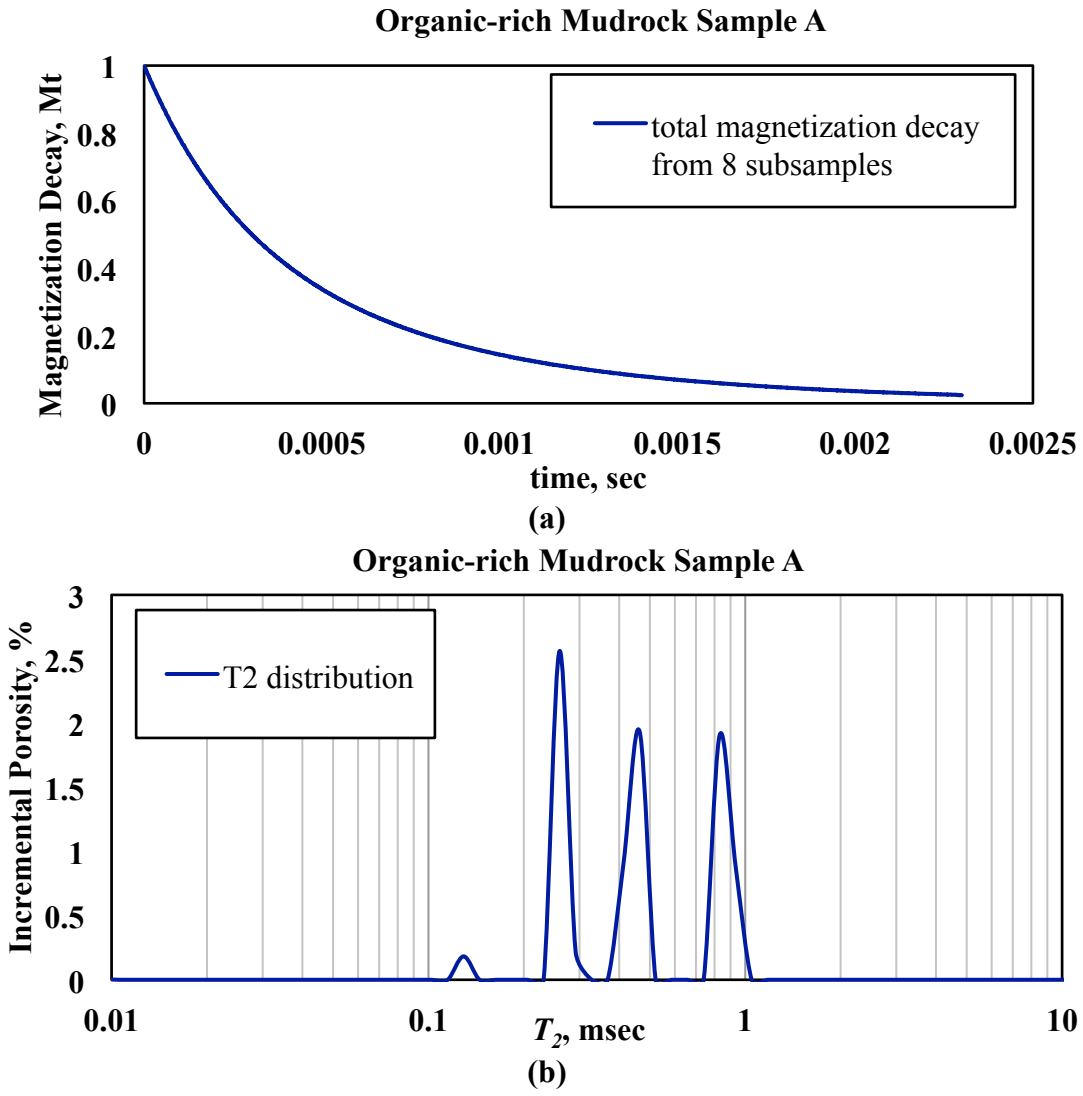

Fig. 7.10—Organic-rich mudrock Sample A: (a) the total transverse magnetization decay from all 8 subsamples, and (b) the estimated total NMR T_2 distribution of Sample A from the total transverse magnetization decay.

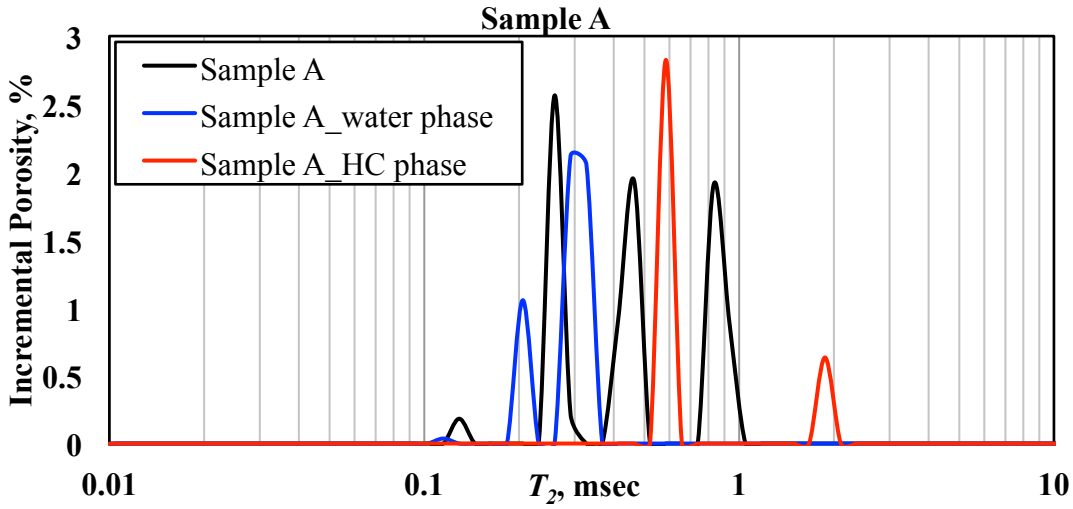

Fig. 7.11—Organic-rich mudrock Sample A: The simulated T_2 distribution of water phase (blue), hydrocarbon phase (red), and both phases in the whole rock sample (black). The area under each T_2 distribution curve represents the corresponding porosity.

To investigate the impact of fluid distribution and wettability of organic-rich mudrocks on NMR relaxometry, we altered the wettability of inorganic pores of Sample A to hydrocarbon-wet and run NMR simulations again. **Fig. 7.12** shows the comparison between the NMR T_2 distributions of original Sample A (black curve), and the modified Sample A fully saturated with hydrocarbon (green curve). The comparison result indicates that when the inorganic rock matrix changes from water-wet to hydrocarbon-wet, the NMR T_2 distribution of the organic-rich mudrock Sample A shows a downshift of T_2 peaks. This downshift of T_2 peaks can be due to the diffusional coupling between the hydrocarbon in all the organic and inorganic pores, which are fully saturated with hydrocarbon now.

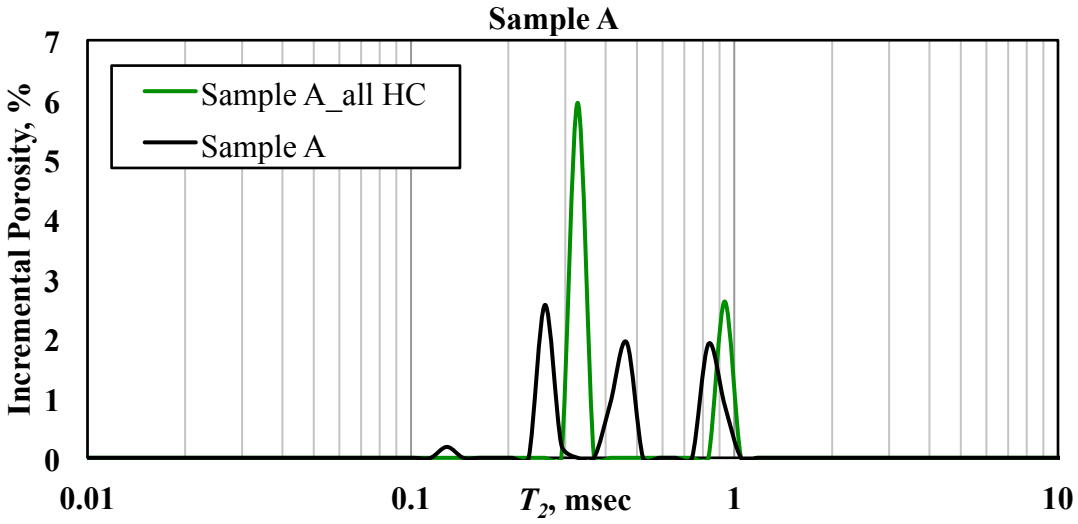

Fig. 7.12—Organic-rich mudrock Sample A: The simulated T_2 distributions of Sample A before (black) and after inorganic pores change to hydrocarbon-wet (green curve), i.e. all inorganic pores are fully saturated with hydrocarbon.

Furthermore, we explored the impact of fluid distribution on NMR relaxometry when the inorganic rock matrix remains water-wet but the hydrocarbon leaks into the inorganic pores through micro-fracture networks. We inserted four synthetic micro-fractures into Sample A to mimic the micro-fractures in organic-rich mudrock samples (Curtis et al. 2011; Chalmers et al. 2012; Loucks et al. 2012; Koneti et al. 2012), and saturated them with hydrocarbon. **Fig. 7.13a** shows the 3D pore-scale image of fractured Sample A, and **Fig. 7.13b** shows the comparison between the NMR T_2 distributions of original (black) and fractured Sample A (red dash curve). The results show that a T_2 peak related to hydrocarbon phase in the micro-fractures appear in the NMR T_2 distribution at 1.87 msec. It is observed that when the hydrocarbon leaks from organic pores into inorganic matrix through micro-fracture networks, it might distort the NMR T_2 distribution by downshifting the T_2 peaks.

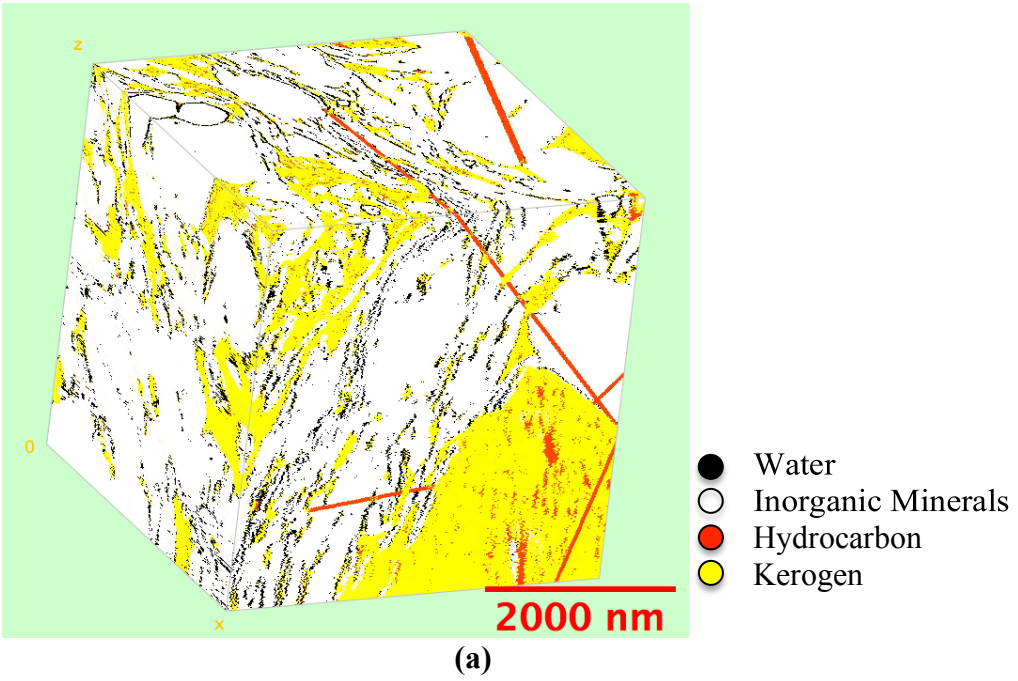

Fig. 7.13—Organic-rich mudrock Sample A: (a) The 3D pore-scale image for Sample A containing four planar micro-fractures. The black, white, red, and yellow regions represent water, inorganic minerals, hydrocarbon, and kerogen, respectively; and (b) the simulated T_2 distributions of original (black) and fractured Sample A (red dash curve).

7.4.3 Organic-rich Mudrock Sample B

The total NMR response from both water and hydrocarbon phases in organic-rich mudrock Sample B was also simulated using the two-phase NMR simulator. **Table 7.3** lists the total porosity, organic porosity, inorganic porosity, and matrix volume of Sample B and its eight subsamples, named as B-1, B-2, …, and B-8. The porosity values show that Sample B is highly inhomogeneous in spatial distribution of organic and inorganic pores.

Fig. 7.14 shows the simulated T_2 distributions for all eight subsamples of Sample B, demonstrating that the pore size distributions and porosities of subsamples are highly inhomogeneous. Then we combined the transverse magnetization decays from all eight subsamples to calculate the total transverse magnetization decay in Sample B, and estimated the total NMR T_2 distribution in Sample B by T_2 inversion. **Figs. 7.15a** and **7.15b** show the total transverse magnetization decay and the NMR T_2 distribution of organic-rich mudrock Sample B, respectively.

To investigate the impact of wettability alteration on Sample B, we changed the inorganic pores from water-wet to hydrocarbon-wet, and saturated them with hydrocarbon. **Fig. 7.16** shows the simulated NMR T_2 distribution curves of Sample B before (black) and after (green curve) the inorganic pores change from water-wet to hydrocarbon-wet. An obvious distortion of T_2 distribution is observed, and most T_2

peaks are downshifted. As mentioned in the case of Sample A, this effect might be due to the diffusional coupling between hydrocarbon in organic pores and inorganic pores.

Table 7.3—Organic-rich mudrock Sample B: the total porosity, organic porosity, inorganic porosity, and matrix volume of the sample and its eight subsamples.

Matrix	Total Porosity, %	Organic Porosity, %	Inorganic Porosity, %	Matrix Volume, pixel^3
Sample B	6.00	1.43	4.57	694x694x694
Subsample B-1	5.52	1.05	4.47	347x347x347
Subsample B-2	10.67	2.25	8.42	347x347x347
Subsample B-3	2.43	0.47	1.96	347x347x347
Subsample B-4	4.59	1.67	2.92	347x347x347
Subsample B-5	4.99	1.59	3.40	347x347x347
Subsample B-6	9.07	2.11	6.96	347x347x347
Subsample B-7	5.46	0.96	4.50	347x347x347
Subsample B-8	5.28	1.37	3.91	347x347x347

7.5. Discussions

We observed that the simulated NMR relaxometry of organic-rich mudrocks shows narrower T_2 distributions compared to experimental data (Odusina et al. 2011; Kausik et al. 2011; Sulucarnain et al. 2012). This is due to the fact that our FIB-SEM images of organic-rich mudrocks have a limited view area of several microns, and that the imaging resolution is 4 - 8 nm/pixel, thus only a small range of pore sizes is captured by the FIB-SEM images. Given a sufficiently large FIB-SEM image that shows all possible pore sizes in a real rock, our simulation results should be comparable to experimental data.

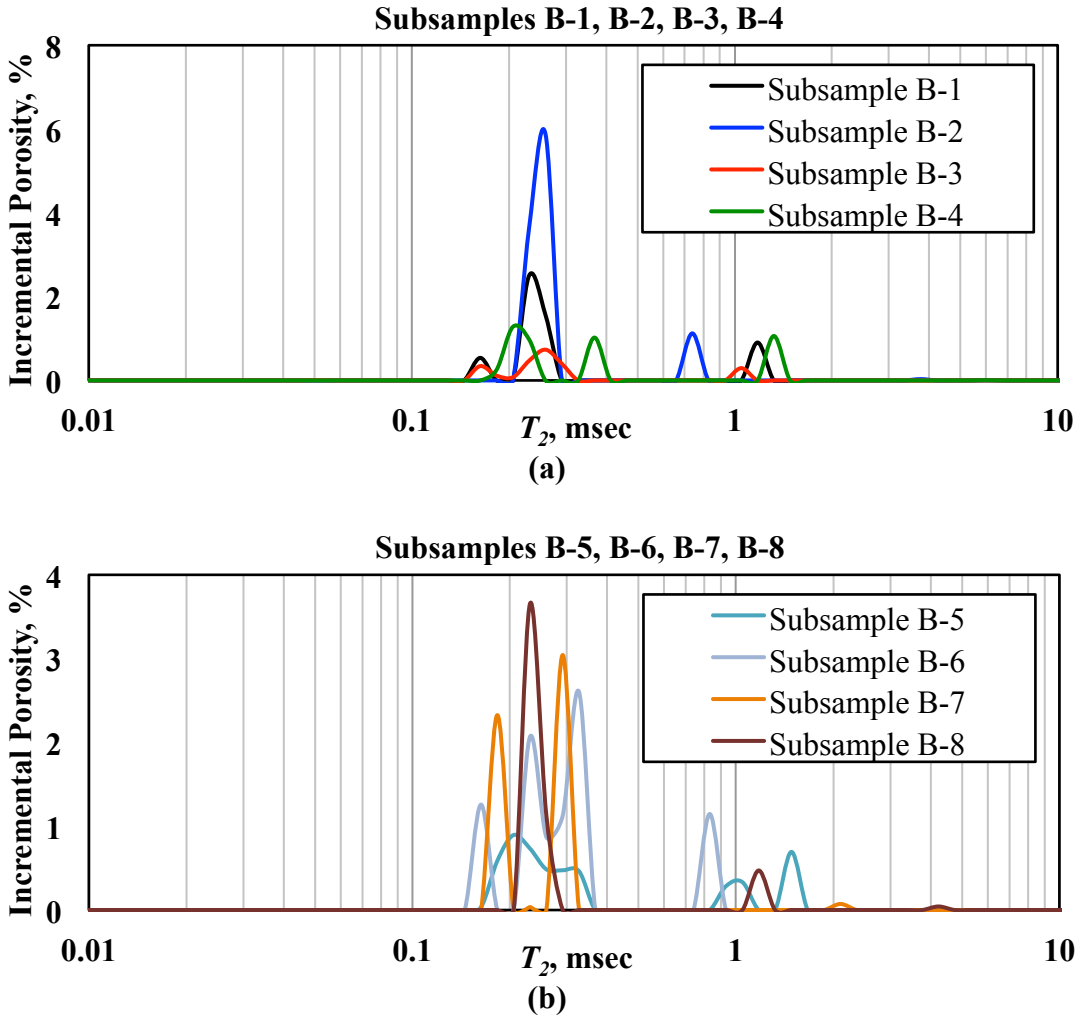

Fig. 7.14—Organic-rich mudrock Sample B: the simulated T_2 distributions of (a) subsamples B-1, B-2, B-3, B-4, and (b) subsamples B-5, B-6, B-7, and B-8.

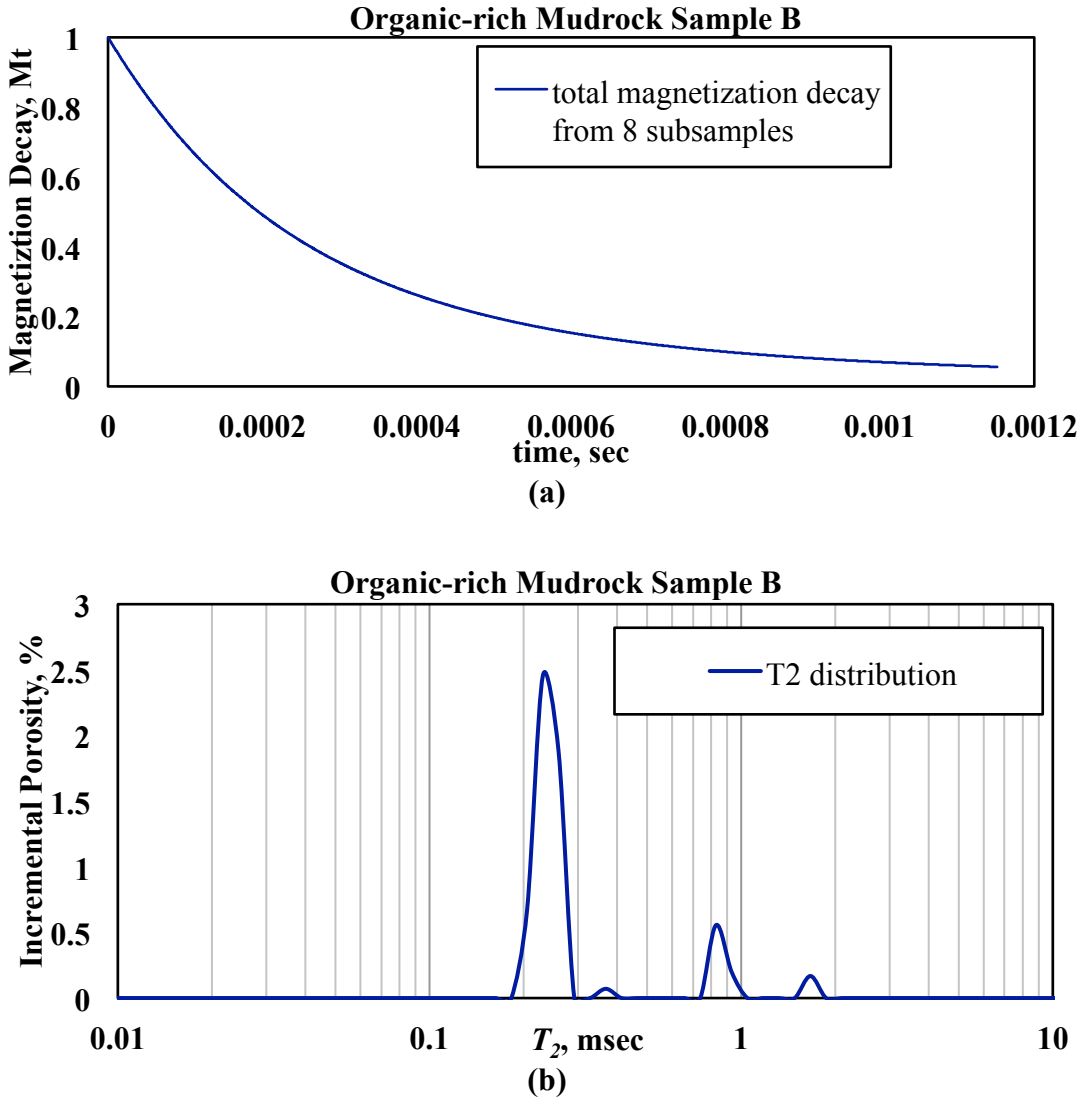

Fig. 7.15—Organic-rich mudrock Sample B: (a) the total transverse magnetization decay from all 8 subsamples, and (b) the estimated total NMR T_2 distribution of Sample B from the total transverse magnetization decay.

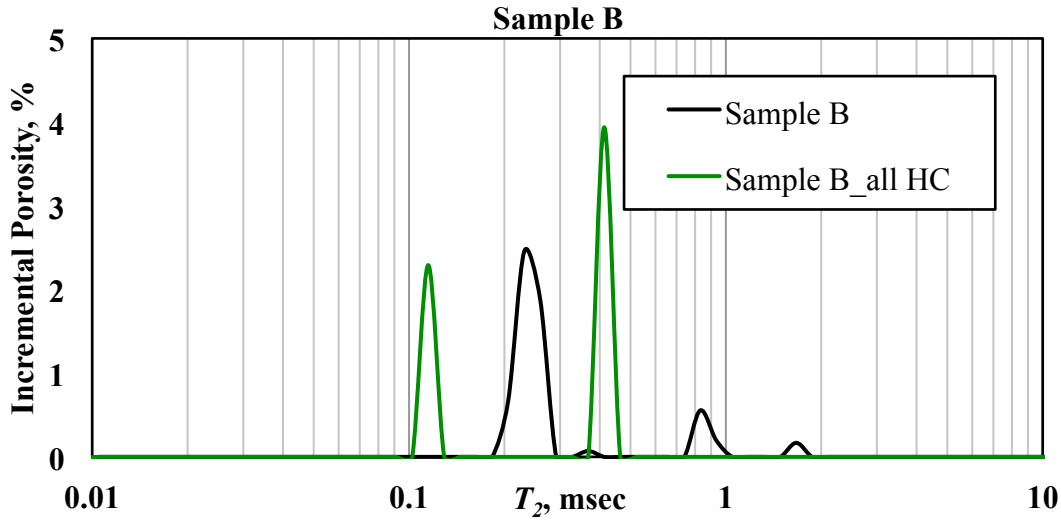

Fig. 7.16—Organic-rich mudrock Sample B: The simulated T_2 distributions of Sample B before (black) and after inorganic pores change to hydrocarbon-wet (green curve), i.e., all inorganic pores are fully saturated with hydrocarbon.

Another limitation of our simulation method resides in the modeling of surface relaxation in organic pores. In the two-phase NMR simulator, the surface relaxation in organic pores was modeled by collisions and killings of random walkers on the organic surface, which imitate the interactions between proton spins in fluids and paramagnetic impurities on the solid surface. However, previous publications indicated that the surface relaxation in organic matter can be caused by other physical mechanisms, such as homonuclear dipolar coupling (Washburn and Birdwell 2013b; Washburn 2014; Sigal and Odusina 2011; Daigle et al. 2014). Surface relaxation caused by homonuclear dipolar coupling shows a significant dependence on temperature and orientation of organic pores, thus cannot be merely represented by the collision/killing process. The future development of the NMR two-phase simulator should take into account of

various physical mechanisms including homonuclear dipolar coupling in organic pores to improve the reliability of simulations.

7.6. Conclusions

We successfully improved the previously developed single-phase NMR numerical simulator (Talabi et al. 2009) to model the NMR responses in organic-rich mudrocks, and applied the simulation method to synthetic and actual organic-rich mudrock samples. The NMR responses from hydrocarbon and water phases in organic-rich mudrock samples were simultaneously simulated in the two-phase NMR simulator. To investigate the impact of wettability and fluid distribution on NMR relaxometry of organic-rich mudrocks, we changed the water-wet inorganic pores to hydrocarbon-wet. The simulation results demonstrated that the alteration of wettability can evidently influence the NMR T_2 distribution of organic-rich mudrocks. After the inorganic pores change from water-wet to hydrocarbon-wet, the water T_2 peak shifts upward by up to 0.5 msec, and a fast-relaxing T_2 peak appears at around 0.1 to 0.4 msec, which is related to the thin layer of hydrocarbon saturating the inorganic pore surface. In all the synthetic and actual organic-rich mudrock samples, we observed the distortion of NMR T_2 distribution caused by wettability alteration. Furthermore, we simulated the case when hydrocarbon leaks into inorganic rock matrix through micro-fracture networks in an actual organic-rich mudrock sample. The results showed that a T_2 peak related to the hydrocarbon in micro-fractures appears at 0.4 - 0.5 msec on NMR T_2 distribution of the

fractured rock sample, demonstrating that the wettability and fluid distribution can evidently influence NMR relaxometry of organic-rich mudrocks.

In the presence of reliable 3D pore-scale images of rock samples, the introduced NMR two-phase simulation method enables further developments on interpretation of NMR relaxometry in organic-rich mudrocks, which has been challenging in laboratory experiments. The outcomes of this research can improve understanding of the parameters affecting NMR relaxometry, and may potentially enhance the interpretation of NMR borehole measurements for real-time assessment of pore-size distribution, fluid distribution, wettability, and micro-fractures in organic-rich mudrock formations.

8. SUMMARY, CONCLUSIONS, AND RECOMMENDATIONS

This final section summarizes the major results and conclusions of the work presented in this dissertation. Based on the completed work, we also make recommendations on potential future research about improving the interpretation of NMR measurements in formations with complex pore structures.

8.1. Summary

The main technical contributions from the dissertation are summarized as below:

1. The impact of micro-fractures on NMR relaxometry in various rock samples was quantified by numerical simulations and theoretical analysis;
2. A 1D analytical model for NMR fracture-pore diffusional coupling was established, and its viability to estimate the volumetric concentrations and apertures of micro-fractures in multiple-pore-type systems was investigated;
3. A directional pore-connectivity factor was introduced to characterize the anisotropic pore connectivity in rock samples. We proposed two approaches to calculate the directional pore-connectivity factor in a rock sample: (a) based on pure image analysis, and (b) based on image analysis combined with electrical formation factor;
4. An innovative NMR-based directional permeability model was developed to estimate anisotropic permeability of rock samples with complex pore structure;

5. The impact of fracture-pore diffusional coupling on NMR permeability assessment was quantified by numerical simulations, and the reliability of conventional NMR-based permeability models and the NMR directional permeability model was compared and evaluated in fractured formations;
6. A two-phase pore-scale NMR simulator was developed to model the NMR responses in organic-rich mudrocks. The NMR signals from both water and hydrocarbon phases in organic-rich mudrocks are simultaneously simulated; and
7. The impacts of fluid distribution and wettability alteration on NMR relaxometry in organic-rich mudrocks were investigated by changing the wettability of inorganic pores and comparing the NMR responses.

8.2. Conclusions

The numerical simulation and theoretical analysis results reported in this dissertation led to the conclusions listed below:

1. The micro-fractures may significantly influence NMR relaxometry of rock samples. This influence is due to fracture-pore diffusional coupling, which can be theoretically described by a 1D analytical model. The NMR simulation results and the 1D analytical model cross-validate each other and confirm the existence of fracture-pore diffusional coupling effect in fractured rock samples;
2. Under the influence of fracture-pore diffusional coupling, the NMR relaxometry of fractured rock samples is sensitive to the relative size of micro-fractures and inter-granular pores, the volumetric concentration and the shape of micro-

fractures. The results are that the long T_2 mode shifts downward with increasing amplitude, and the short T_2 mode remains almost at the same T_2 position with damping amplitude.

3. If the impact of fracture-pore diffusional coupling is not taken into account in interpretation of NMR relaxometry, the intergranular pore size can be underestimated by up to 29%, and the volume fraction of intergranular pores can be underestimated by more than 10%;
4. It is possible to use the 1D analytical model of NMR fracture-pore diffusional coupling with aid of other well logging measurements, to evaluate the volumetric concentrations of micro-fractures, the inter-granular porosity, and the micro-fracture aperture in fractured formations. The error of fracture volumetric concentration estimation is within 40%, and the error of fracture aperture estimation is within 20%;
5. The introduced NMR directional permeability model, which incorporates the directional pore-connectivity factor, significantly improves the permeability assessment for rock samples with complex pore structure. It reflects the anisotropic characteristics of rock permeability, minimizes the parameter calibration effort, and shows promising potential as a general model for all rock types. The estimated rock permeability values covered six orders of magnitude, demonstrating that the model is reliable for a large variety of rock samples from different formations. And 80% of the rock permeability were estimated within a

factor of two, the other 20% were accurate within a factor of five, showing excellent accuracy of the NMR directional permeability model;

6. The fracture-pore diffusional coupling may influence the NMR permeability assessment on fractured rock samples. In rock samples showing significant fracture-pore diffusional coupling, the NMR directional permeability model and the SDR model can estimate permeability within one order of magnitude, but Coates model can overestimate or underestimate the permeability by up to two orders of magnitude; in rock samples showing minimal fracture-pore diffusional coupling, all three models estimate the rock permeability with similar accuracy. In sum, the SDR and NMR directional permeability models show better reliability than the Coates model in fractured formations when fracture-pore diffusional coupling is significant;
7. The introduced two-phase NMR pore-scale simulator can simultaneously model the NMR signals from both hydrocarbon and water phases in organic-rich mudrocks. The simulated NMR T_2 distribution covers both the water and hydrocarbon signals in organic-rich mudrock samples; and
8. The alteration of wettability and fluid distribution has measurable impacts on NMR relaxometry in organic-rich mudrocks. When the inorganic pores in organic-rich mudrocks change from water-wet to hydrocarbon-wet, the fast-relaxing T_2 peaks related to water phase shifted upwards by up to 0.5 msec, and a fast-relaxing T_2 peak appears, which is related to the thin layer of hydrocarbon saturating the inorganic pores. When the hydrocarbon leaks into the inorganic

mudrock matrix through micro-fracture networks, a T_2 peak related to the hydrocarbon in micro-fractures appears on T_2 distribution of the fractured organic-rich mudrock sample, at around 0.1 - 0.4 msec.

8.3. Recommendation for Future Work

The recommendations for future research work that can extend the scope and contributions presented in this dissertation are listed below:

1. The introduced NMR directional permeability model is calibrated by the 20 rock samples presented in Section 5, and successfully tested by several other rock samples. To enhance the reliability of NMR directional permeability model, it is recommended that more carbonate and sandstone rock samples are included in the calibration and testing process. Organic-rich mudrock samples can also be included in the calibration and testing of NMR directional permeability model, given reliable permeability data and pore-scale images of organic-rich mudrock samples.
2. The influences of fracture-pore diffusional coupling effect on NMR permeability assessment would be better illustrated if experimental results on real rock samples are included. The future work includes evaluating the NMR permeability models in real rock samples before and after fracturing, and investigating the extent of fracture-pore diffusional coupling effect on real rock samples.

3. The two-phase NMR simulation presented in the Section 7 did not consider other possible relaxation mechanisms in organic pores in organic-rich mudrocks, such as the homonuclear dipolar coupling between proton spins and organic matters. The future work could explore the possibility of simulating all possible relaxation mechanisms in organic-rich mudrocks to better interpret the NMR relaxometry.
4. The two-phase NMR simulation would also be improved if experimental NMR data can be used to validate the simulation results. This work involves upscaling the nano-scale simulation results to match the NMR experimental data in the core scale.
5. The NMR numerical simulation results presented in this dissertation were based on several assumptions including zero diffusion-induced relaxation. In the future work, one can include the extra magnetization decay of diffusion-induced relaxation into simulation results, and compare with NMR experimental data.

REFERENCES

Akkurt, R., Bachman, H. N., Cao Minh, C., Flaum, C., LaVigne, J., Leveridge, R., Carmona, R., Crary, S., Decoster, E., Heaton, N., Hurlimann, M. D., Looyestijn, W. J., and Mardon, D., 2009, Nuclear Magnetic Resonance comes out of its shell: Oilfield Review, vol. 20, no. 4. Copyright © 2009 Schlumberger.

AlGhamdi, T. M. and Arns, C. H., 2012, Correlations between NMR T2-D responses and relative permeability from micro Xray-CT images: SPE Annual Technical Conference and Exhibition, 8-10 October. SPE 158168.

Anand, V. and G. J. Hirasaki, 2005, Diffusional coupling between micro and macroporosity for NMR relaxation in sandstones and grainstones: SPWLA 46th Annual Logging Symposium. SPWLA-2005-KKK.

Aster, R., Borchers, B., and Thurber, C., 2012, *Parameter estimation and inverse problems*, 2nd Edition, Academic Press.

Bernabe, Y., Li, M., and Maineult, A., 2010, Permeability and pore connectivity: a new model based on network simulation: Journal of Geophysical Research, vol. 115, B10203.

Bloch, F., 1946, Nuclear induction: Physics Review, vol. 70, 460-474.

Blunt, M. J., Bijeljic, B., Dong, H., Gharbi, O., Iglauer, S., Mostaghimi, P., Paluszny, A., and Pentland, C., 2013, Pore-scale imaging and modeling: Advances in Water Resources, vol. 51, 197-216.

Brownstein, K. R. and C. E. Tarr, 1979, Importance of classical diffusion in NMR studies of water in biological cells: Physical Review A, vol. 19, no. 6, 2446-2453.

Cao Minh, C., Crary, S., Zielinski, L., Liu, C. B., Jones, S., and Jacobsen, S., 2012, 2D-NMR Applications in Unconventional Reservoirs: Canadian Unconventional Resources Conference held in Calgary, Alberta, Canada, 30 October-1 November.

Carr, H. and Purcell, E., 1954, Effects of diffusion on free precession in Nuclear Magnetic Resonance experiments, Physics Review, vol. 94, 630.

Chalmers, G. R., Bustin, R. M., and Power, I. M., 2012, Characterization of gas shale pore systems by porosimetry, pycnometry, surface area, and field emission scanning electron microscopy/transmission electron microscopy image analyses: Examples from

the Barnett, Woodford, Haynesville, Marcellus, and Doig units: AAPG Bulletin, vol. 96, no. 6, 1099-1119.

Chang, C. T. P., Qiao, J., Chen, S., and Watson, A. T., 1997, Fracture characterization with NMR spectroscopic techniques: Journal of Magnetic Resonance, vol. 126, no. 2, 213-220.

Chang, D., Vinegar, H., Morriss, C., and Straley, C., 1997, Effective porosity, producible fluid and permeability in carbonates from NMR logging: The Log Analyst, vol. 38, no. 2, 60-72.

Chauveteau, G., Nabzar, L., El Attar, Y., and Jacquin, C., 1996, Pore structure and hydrodynamics in sandstones: International Symposium of the Society of Core Analysis, SCA9607.

Chen, J., Zhang, J., Jin, G., Quinn, T., Frost, E., and Chen, J., 2012, Capillary condensation and NMR relaxation time in unconventional shale hydrocarbon resources: SPWLA 53rd Annual Logging Symposium, 16-20 June.

Chen, S., Georgi, D., Fang, S., Salyer, J., and Shorey, D., 1999, Optimization of NMR logging acquisition and processing: SPE Annual Technical Conference and Exhibition. SPE 56766.

Chen, S., Jacobi, D., Kwak, H., Altunbay, M., and Kloos, J., 2008, Pore-connectivity based permeability model for complex carbonate formations: SPWLA 49th Annual Logging Symposium. SPWLA-2008-E.

Chen, S., Miller, D., Li, L., Westacott, D., Murphy, E., and Balliet R., 2013, Qualitative and quantitative information NMR logging delivers for characterization of unconventional shale plays: Case studies: SPWLA 54th Annual Logging Symposium, June 22-26.

Coates, G. R., et al, 1997, A new characterization of bulk-volume irreducible using magnetic resonanace: SPWLA 38th Annual Logging Symposium, SPWLA-1997-QQ. Also published in 1997 in Dialog, London Petrophysical Society, vol. 5, no. 6, 9-16.

Coates, G. R., Xiao, L., and Prammer, M. G., 1999, NMR logging principles and applications: Halliburton Energy Services, Houston.

Curtis, M. E., Ambrose, R. J., Sondergeld, C. H., and Rai, C. S., 2011, Transmission and Scanning Electron Microscopy investigation of pore connectivity of gas shales on the nanoscale: Presented at the North American Unconventional Gas Conference and Exhibition, 14-16 June, The Woodlands, Texas, USA. SPE 144391.

Cussler, E. L., 1997, *Diffusion: Mass Transfer in Fluid Systems*, 2nd Edition, Cambridge University Press, New York.

Daigle, H., Johnson, A., Gips, J. P., and Sharma, M., 2014, Porosity evaluation of shales using NMR secular relaxation: Unconventional Resources Technology Conference, Denver, Colorado, 25-27 August. URTeC 1905272.

Degruyter, W., Bachmann, O., Burgisser, A., and Malaspinas, O., 2010, Synchrotron X-ray microtomography and lattice Boltzmann simulations of gas flow through volcanic pumices: Geosphere, October, vol. 6, 470-481.

Dong, H., 2007, Micro-CT imaging and pore network extraction: PhD Dissertation, Imperial College London.

Fleury, M., Deflandre, F., and Godefroy, S., 2001, Validity of permeability prediction from NMR measurements: Chimie/Chemistry, vol. 4, 869-872.

Freedman, R., Anand, V., Catina, D., Grant, B., Tabrizi, P., Torres, R., Ganesan, K., Borman, C., Krueckl, C., and Ryan, D., 2013, Major advancement in reservoir fluid analysis achieved using a new high-performance Nuclear Magnetic Resonance laboratory system: SPWLA 54th Annual Logging Symposium, 22-26 June.

Galatsanos, N.P. and Katsaggelos, A.K., 1992, Methods for choosing the regularization parameter and estimating the noise variance in image restoration and their relation, IEEE Transactions on Image Processing, vol. 1, no. 3, 322-366.

Grunewald, E. and R. Knight, 2009, A laboratory study of NMR relaxation times and pore coupling in heterogeneous media: Geophysics, vol. 74, no. 6, E215-E221.

Gueguen, Y. and Dienes, J., 1989, Transport properties of rocks from statistics and percolation: Mathematical Geology, vol. 21, no. 1, 1-13.

Gundersen, H. J. G., Boyce, R. W., Nyengaard, J. R., and Odgaard, A., 1993, The connEuler: Unbiased estimation of connectivity using physical dissectors under projection: Bone, vol. 14, no. 3, 217-222.

Gupta, A., Datta-Gupta, A., and King, M. J., 2010, Geology-based reservoir model building for carbonate reservoirs: A project founded by Qatar National Research Found (QNRF), Cycle 4.

Jain, V., Cao Minh, C., Heaton, N., Ferraris, P., and Ortenzi, L., 2013, Characterization of underlying pore and fluid structure using factor analysis on NMR data: SPWLA 54th Annual Logging Symposium, June 22-26.

Jerath, K., Torres-Verdin, C., and Merletti, G., 2012, Improved assessment of in-situ fluid saturation with multi-dimensional NMR measurements and conventional well logs: SPWLA 53th Annual Logging Symposium, 16-20 June.

Jiang, T., Rylander, E., Singer, P. M., Lewis, R. E., and Sinclair, S. M., 2013, Integrated petrophysical interpretation of Eagle Ford shale with 1-D and 2-D Nuclear Magnetic Resonance (NMR): SPWLA 54th Annual Logging Symposium, June 22-26.

Jin, G., Torres-Verdin, C., and Toumelin, E., 2009, Comparison of NMR simulations of porous media derived from analytical and voxelized representations: Journal of Magnetic Resonance, vol. 200, 313-320.

Kausik, R., Cao Minh, C., Zielinski, L., Vissapragada, B., Akkurt, R., Song, Y., Liu, C., Jones, S., and Blair, E., 2011, Characterization of Gas Dynamics in Kerogen Nanopores by NMR: SPE ATCE held in Denver, Colorado, USA, 30 October-2 November.

Kenyon, W. E., Day, P. I., Straley, C., and Willemsen, J. F., 1988, A three part study of NMR longitudinal relaxation properties of water saturated sandstones: SPE Formation Evaluation, vol. 3, no. 3, 622 -636.

Kleinberg, R. L., and Horsfield, M. A., 1990, Transverse relaxation processes in porous sedimentary rock: Journal of Magnetic Resonance, vol. 88, 9-19.

Kleinberg, R. L., W. E. Kenyon, and P. P. Mitra, 1994, Mechanism of NMR relaxation of fluids in rock: Journal of Magnetic Resonance, Series A, vol. 108, no. 2, 206-214.

Koneti, S., Gokhale, S., and Wadsworth, T., 2012, Tubular fracturing: pinpointing the cause: *Innovating While Drilling*, March/April. (http://www.drillingcontractor.org/tubular-fracturing-pinpointing-the-cause-14544)

Levitt, M. H., 2001, *Spin Dynamics: Basics of Nuclear Magnetic Resonance*, Jone Wiley & Sons, Chichester, UK.

Liaw, H.-K., R. Kulkarni, S. Chen, and A.T. Watson, 1996, Characterization of Fluid Distributions in Porous Media by NMR Techniques: AIChE Journal 42 (2): 538-546.

Loucks, R., Reed, R., Ruppel, S., and Hammes U., 2012, Spectrum of pore types and networks in mudrocks and a descriptive classification for matrix-related mudrock pores, AAPG Bulletin, vol. 96, no. 6, 1071-1098.

Meiboom, S. and Gill, D., 1958, Modified spinecho method for measuring nuclear relaxation times: The Review of Scientific Instruments, vol. 29, no. 8, 688-691.

Meridji, Y, and Hursan, G., 2013, Fluid identification in complex clastic reservoirs using 2D NMR maps: a case study from Saudi Arabia: SPE Saudi Arabia section Annual Techical Symposium and Exhibition, 19-22 May.

Mohnke, O. and Klitzsch, N., 2010, Microscale simulations of NMR Relaxation in porous media considering internal field gradients: Vadose Zone Journal, vol. 9, no. 4, 846-857.

Mostaghimi, P., Blunt, M. J., and Bijeljic, B., 2012, Computations of absolute permeability on micro-CT images: Mathematical Geosciences, vol. 45, no. 1, 103-125.

Nakashima, Y. and T. Kikuchi, 2007, Estimation of the apertures of water-saturated fractures by Nuclear Magnetic Resonance well logging: Geophysical Prospecting, vol. 55, no. 2, 235-254.

Odgaard, A., and Gundersen, H. J. G., 1993, Quantification of connectivity in cancellous bone, with special emphasis on 3-D reconstructions: Bone, vol. 14, 173-182.

Odusina, E., Sondergeld, C., and Rai, C., 2011, An NMR study on shale wettability: Canadian Unconventional Resources Conference held in Calgary, Alberta, Canada, 15-17 November. SPE-147371.

Øren, P. E. and Bakke, S., 2002, Process based reconstruction of sandstones and prediction of transport properties: Transport in Porous Media, vol. 46, 311-343.

Palabos, 2013, The Palabos software project: http://www.palabos.org/documentation/tutorial/permeability.html.

Passey, Q. R., Bohacs, K., Esch, W. L., Klimentidis, R., 2010, From Oil-Prone Source Rock to Gas-Producing Shale Reservoir - Geologic and Petrophysical Characterization of Unconventional Shale Gas Reservoirs: International Oil and Gas Conference and Exhibition in China, 8-10 June, Beijing, China

Ramakrishnan, T.S., Schwartz, L.M., Fordham, E.J., and Wilkinson, D.J., 1998, Forward models for nuclear magnetic resonance in carbonate rocks: SPWLA 39th Annual Logging Symposium. SPWLA-1998-SS.

Ramakrishnan, T.S., Schwartz, L.M., Fordham, E.J., and Wilkinson, D.J., 1999, Forward models for nuclear magnetic resonance in carbonate rocks: The Log Analyst, vol. 40, no. 4, 260-270

Roberts, S.P., P.J. McDonald, and T. Pritchard, 1995, A Bulk and Spatially Resolved NMR Relaxation Study of Sandstone Rock Plugs: Journal of Magnetic Resonance, Series A 116 (2): 189-195.

Rylander, E., Singer, P. M., Jiang, T., Lewis, R., McLin, R., and Sinclair S., 2013, NMR T2 Distributions in the Eagle Ford Shale: Reflections on Pore Size: Unconventional Resources Conference-USA held in The Woodlands, Texas, USA, 10-12 April.

Schindelin, J., Arganda-Carreras, I., Frise, E. et al., 2012, Fiji: An Open-Source Platform for Biological-Image Analysis. Nat Meth, vol. 9, no. 7, 676-682.

Serry, A. M., Al-Mutwali, O., Al-Mansoori, A., M., Al-Marzouki, M. I., Budebes, S. A., Gueddoud, A. G., Balliet, R., Aki, A. C., and Akopyan, G., 2013, Sourceless porosity and permeability estimation with NMR logs while drilling in a carbonate reservoir: a case study: SPE Middle East Oil and Gas Show and Conference, 10-13 March.

Sigal, R., 2015, Pore-size distributions for organic-shale-reservoir rocks from Nuclear-Magnetic-Resonance spectra combined with adsorption measurements: SPE Journal, April 2015. SPE-174546-PA.

Sigal, R. and Odusina, E., 2011, Laboratory NMR measurements on methane saturated barnett shale samples: Petrophysics, vol. 52, no. 1, 32-49.

Singer, P. M., Rylander, E, Jiang, T., McLin, R., Lewis, R. E., and Sinclair, S. M., 2013, 1D and 2D NMR core-log intergration in organic shale: International Symposium of the Society of Core Analysis, 16-19 September.

Smith, C. H., Ramakrishna, S., and Hamilton, L., 2013, Solutions for difficult reservoirs direct NMR fluid type and permeability: SPE Production and Operations Symposium, 23-26 March.

Souza, A., Carneiro, G., Zielinski, L., Polinski, R., Schwartz, L., Hurlimann, M. D., Boyd, A., Rios, E. H., and et al., 2013, Permeability prediction improvement using 2D NMR diffusion-T2 maps: SPWLA 54th Annual Logging Symposium, 22-26, June.

Sulucarnain, I., Sondergeld, C. H., and Rai, C., S., 2012, An NMR study of shale wettability and effective surface relaxivity: Canadian Unconventional Resources Conference held in Calgary, Alberta, Canada, 30 October-1 November.

Talabi, O.A., 2008, Pore-scale simulation of NMR response in porous media: PhD Dissertation, Imperial College London.

Talabi, O., AlSayari, S., Iglauer, S., and Blunt, M.J., 2009, Pore-scale simulation of NMR response: Journal of Petroleum Science and Engineering, vol. 67, no. 3-4, 168-178.

Toumelin, E., C. Torres-Verdín, S. Chen, and Fischer, D. M., 2002, Analysis of NMR diffusion coupling effects in two-phase carbonate rocks: comparison of measurements with Monte Carlo simulations: SPWLA-2002-JJJ.

Toumelin, E., Torres-Verdín, C., and Chen, S., 2003, Modeling of multiple echo-time NMR measurements for complex pore geometries and multiphase saturations: SPE Reservoir Evaluation & Engineering, vol. 6, no. 4, 234-243. SPE 85635.

Toumelin, E., 2006, Pore-scale petrophysical models for the simulation and combined interpretation of Nuclear Magnetic Resonance and wide-band electromagnetic measurements of saturated rocks: PhD Dissertation, University of Texas at Austin.

Valori, A., Ali, F., AlZoukani, A., and Taherian, R., 2014, NMR measurements for pore size mapping at fine scale: International Petroleum Technology Conference, Doha, Qatar, 20-22 January.

Venkataramanan, L., Gruber, F. K., LaVigne, J., Habashy, T. M., Iglesias, J. G., Anand, V., Rampurawala, M. A., Jain, V., Heaton, N., Akkurt, R., Rylander, E., and Lewis, R., 2015, New method to estimate porosity more accurately from NMR data with short relaxation times: Petrophysics, vol. 56, no. 2, April. Originally presented at the SPWLA 55th Annual Logging Symposium, Abu Dhabi, United Arabic Emirates, May 18-22. SPWLA-V.

Vogel, H. J., 1997, Morphological determination of pore connectivity as a function of pore size using serial sections: European Journal of Soil Science, vol. 48, no. 3, 365-377.

Washburn, K. E., and Birdwell, J. E., 2013a, A new laboratory to shale analysis using NMR relaxometry: Unconventional Resources Technology Conference (URTeC) held in Denver, Colorado, USA, 12-14 August.

Washburn, K. E., and Birdwell, J. E., 2013b, Updated methodology for nuclear magnetic resonance characterization of shales: Journal of Magnetic Resonance, vol. 233, 17-28.

Washburn, K. E., 2014, Relaxation mechanics and shales: Concepts in Magnetic Resonance Part A, vol. 43A, no. 3, 57-78.

Wright, S. M., 1999, "NMR-MRI", Chapter 16 in *Introduction to Biomedical Engineering*, Enderle, J., Blanchard, S., Bronzino, J., Eds., Academic Press, New York.

Xiao, L. and K. Li, 2011, Characteristics of the Nuclear Magnetic Resonance logging response in fracture oil and gas reservoirs: New Journal of Physics, vol. 13, no. 4, 045003.

Xiao, L., Zou, C., Mao, Z., Liu, X., Hu, X., and Jin, Y., 2013, Tight-gas-sand permeability estimation from Nuclear-Magnetic-Resonance (NMR) logs based on the Hydraulic-Flow-Unit (HFU) approach: Journal of Canadian Petroleum Technology, vol. 52, no. 04, 306-314. SPE 167255.

Zhang, J., Chen, J., and Edwards, C., 2012, Lab NMR study on adsorption/condensation of hydrocarbon in smectite clay: SPW/EAGE European Unconventional Resources Conference and Exhibition, 20-22 March.

Zielinski, L., Ramamoorthy, R., Cao Minh, C., Sayed, R. H., and Abdelaal, A. F., 2010, Restricted diffusion effects in saturation estimates from 2D diffusion-relaxation NMR Maps: SPE Annual Technical Conference and Exhibition, 19-22 September. SPE 134841.

APPENDIX: RELATED PUBLICATIONS

Peer-Reviewed Journal Publications

Chi, L. and Heidari, Z., 2015a, Diffusional coupling between micro-fractures and pore structure and its impact on NMR measurements in multiple-porosity systems: *Geophysics*, Vol 80(1): D31-D42. http://dx.doi.org/10.1190/geo2013-0467.1

Chi, L. and Heidari, Z., 2015b, Directional permeability assessment in formations with complex pore geometry using a new NMR-based permeability model: *SPE Journal* (under review)

Chi, L., Cheng, K., and Heidari, Z., 2015, Improved assessment of pore-size distribution and pore connectivity in multiple-porosity systems using contrast agents and NMR relaxation measurements: *SPE Reservoir Evaluation & Engineering* (under review)

Refereed Conference Proceedings

Chi, L. and Heidari, Z., 2015c, Investigation of Wettability and Fluid Distribution in Organic-rich Mudrocks using NMR Two-Phase Simulation: To be presented at the *SPE Annual Technical Conference and Exhibition*, Houston, Texas, October 27-29.

Chi, L. and Heidari, Z., 2015d, Impact of Fracture-Pore Diffusional Coupling on NMR Permeability Assessment in Complex Formations: To be presented at the *56th Annual Logging Symposium Proceedings*, Society of Petrophysicists and Well Log Analysts, Jul.

Chi, L., and Heidari, Z., 2014a, Quantifying the impact of natural fractures and pore structure on NMR measurements in multiple-porosity systems: *7th International Petroleum Technology Conference Proceedings*. IPTC 17688.

Chi, L. and Heidari, Z., 2014b, Directional permeability assessment in formations with complex pore geometry using a new NMR-based permeability model: *55th Annual Logging Symposium Proceedings*, Society of Petrophysicists and Well Log Analysts. SPWLA-2014-E.

Chi, L., Elliot, M., Heidari, Z., and Everett, M., 2014, Assessment of Micro-Fracture Density using Combined Interpretation of NMR Relaxometry and Electromagnetic Logs: *Unconventional Resources Technology Conference*, Denver, Colorado, USA, August 25-27.

Cheng, K., **Chi, L.**, and Heidari, Z., 2014, Improved Assessment of Pore-Size Distribution and Pore Connectivity in Multiple-Porosity Systems using Superparamagnetic Iron Oxide Nanoparticles and NMR Measurement: *SPE Annual Technical Conference and Exhibition*, Amsterdam, The Netherlands, October 27-29.

Chen, H., **Chi, L.**, Kethireddy, N., and Heidari, Z., 2013, Impact of Spatial Distribution of Kerogen Network on Electrical Resistivity of Organic-Rich Source Rocks: *Unconventional Resources Technology Conference*, Denver, Colorado, USA, August.